
JSCSEN 88(3)223–354(2023)

ISSN 1820-7421(Online)

Journal of the Serbian Chemical Society

VOLUME 88

No 3

BELGRADE 2023

Available on line at



www.shd.org.rs/JSCS/

The full search of JSCS

is available through

DOAJ DIRECTORY OF

OPEN ACCESS

JOURNALS

www.doaj.org

The **Journal of the Serbian Chemical Society** (formerly Glasnik Hemijskog društva Beograd), one volume (12 issues) per year, publishes articles from the fields of chemistry. The **Journal** is financially supported by the **Ministry of Education, Science and Technological Development of the Republic of Serbia**.

Articles published in the **Journal** are indexed in **Clarivate Analytics products: Science Citation Index-Expanded™** – accessed via **Web of Science®** and **Journal Citation Reports®**.

Impact Factor announced 2022: **1.100; 5-year Impact Factor: 1.175.**

Articles appearing in the **Journal** are also abstracted by: **Scopus, Chemical Abstracts Plus (CAplusSM), Directory of Open Access Journals, Referativni Zhurnal (VINITI), RSC Analytical Abstracts, EuroPub, Pro Quest and Asian Digital Library.**

Publisher:

Serbian Chemical Society, Karnegijeva 4/III, P. O. Box 36, 1120 Belgrade 35, Serbia
tel./fax: +381-11-3370-467, E-mails: **Society** – shd@shd.org.rs; **Journal** – jscs@shd.org.rs
Home Pages: **Society** – <http://www.shd.org.rs/>; **Journal** – <http://www.shd.org.rs/JSCS/>
Contents, Abstracts and full papers (from Vol 64, No. 1, 1999) are available in the electronic form at the Web Site of the **Journal** (<http://www.shd.org.rs/JSCS/>).

Internet Service:

Nikola A. Pušin (1930–1947), **Aleksandar M. Leko** (1948–1954),

Panta S. Tutundžić (1955–1961), **Miloš K. Mladenović** (1962–1964),

Dorđe M. Dimitrijević (1965–1969), **Aleksandar R. Despić** (1969–1975),

Slobodan V. Ribnikar (1975–1985), **Dragutin M. Dražić** (1986–2006).

BRANISLAV Ž. NIKOLIĆ, Serbian Chemical Society (E-mail: jscs-ed@shd.org.rs)

DUŠAN SLADIĆ, Faculty of Chemistry, University of Belgrade

Editor-in-Chief:

DEJAN OPSENICA, Institute of Chemistry, Technology and Metallurgy, University of Belgrade

Former Editors:

JÁNOS CSANÁDI, Faculty of Science, University of Novi Sad

OLGICA NEDIĆ, INEP – Institute for the Application of Nuclear Energy, University of Belgrade

MILOŠ ĐURAN, Serbian Chemical Society

IVAN JURANIĆ, Serbian Chemical Society

LJILJANA DAMJANOVIĆ-VASILIĆ, Faculty of Physical Chemistry, University of Belgrade

SNEŽANA GOJKOVIĆ, Faculty of Technology and Metallurgy, University of Belgrade

SLAVICA RAŽIĆ, Faculty of Pharmacy, University of Belgrade

BRANKO DUNJIĆ, Faculty of Technology and Metallurgy, University of Belgrade

MIRJANA KIJEVČANIN, Faculty of Technology and Metallurgy, University of Belgrade

TATJANA KALUDEROVIĆ RADOIČIĆ, Faculty of Technology and Metallurgy, University of Belgrade

Sub editors:

Organic Chemistry **DEJAN OPSENICA**, Institute of Chemistry, Technology and Metallurgy, University of Belgrade

Biochemistry and

Biochemistry **JÁNOS CSANÁDI**, Faculty of Science, University of Novi Sad

Inorganic Chemistry

OLGICA NEDIĆ, INEP – Institute for the Application of Nuclear Energy, University of Belgrade

Theoretical Chemistry

MILOŠ ĐURAN, Serbian Chemical Society

Physical Chemistry

IVAN JURANIĆ, Serbian Chemical Society

Electrochemistry

LJILJANA DAMJANOVIĆ-VASILIĆ, Faculty of Physical Chemistry, University of Belgrade

Analytical Chemistry

SNEŽANA GOJKOVIĆ, Faculty of Technology and Metallurgy, University of Belgrade

Polymers

SLAVICA RAŽIĆ, Faculty of Pharmacy, University of Belgrade

Thermodynamics

BRANKO DUNJIĆ, Faculty of Technology and Metallurgy, University of Belgrade

Chemical Engineering

MIRJANA KIJEVČANIN, Faculty of Technology and Metallurgy, University of Belgrade

Materials

ANA KOSTOV, Mining and Metallurgy Institute Bor, University of Belgrade

Metallic Materials and

Metallurgy

VESNA ANTIĆ, Faculty of Agriculture, University of Belgrade

Environmental and

Geochemistry

DRAGICA TRIVIĆ, Faculty of Chemistry, University of Belgrade

History of and

Education in Chemistry

LYNNE KATSIKAS, Serbian Chemical Society

English Language

VLATKA VAJS, Serbian Chemical Society

Editors:

JASMINA NIKOLIĆ, Faculty of Technology and Metallurgy, University of Belgrade

Technical Editors:

VLADIMIR PANIĆ, Institute of Chemistry, Technology and Metallurgy, University of Belgrade

Journal Manager &

MARIO ZLATOVIĆ, Faculty of Chemistry, University of Belgrade

Web Master:

VERA ĆUŠIĆ, Serbian Chemical Society

Office:

Editorial Board

From abroad: **R. Adžić**, Brookhaven National Laboratory (USA); **A. Casini**, University of Groningen (The Netherlands); **G. Cobb**, Baylor University (USA); **D. Douglas**, University of British Columbia (Canada); **G. Inzelt**, Etvos Lorand University (Hungary); **J. Kenny**, University of Perugia (Italy); **Ya. I. Korenman**, Voronezh Academy of Technology (Russian Federation); **M. D. Lechner**, University of Osnabrueck (Germany); **S. Macura**, Mayo Clinic (USA); **M. Spitteler**, INFU, Technical University Dortmund (Germany); **M. Stratakis**, University of Crete (Greece); **M. Swart**, University of Girona (Cataluna, Spain); **G. Vunjak-Novaković**, Columbia University (USA); **P. Worsfold**, University of Plymouth (UK); **J. Zagal**, Universidad de Santiago de Chile (Chile).

From Serbia: **B. Abramović**, **V. Antić**, **V. Beškoski**, **J. Csanadi**, **Lj. Damjanović-Vasilić**, **A. Dekanski**, **V. Dondur**, **B. Dunjić**, **M. Duran**, **S. Gojković**, **I. Gutman**, **B. Jovančević**, **I. Juranić**, **T. Kaluderović Radiović**, **L. Katsikas**, **M. Kijevčanin**, **G. Kostov**, **V. Leovac**, **S. Milonjić**, **V.B. Mišković-Stanković**, **O. Nedić**, **B. Nikolić**, **J. Nikolić**, **D. Ospenica**, **V. Panić**, **M. Petkovska**, **R. Petrović**, **I. Popović**, **B. Radak**, **S. Ražić**, **D. Sladić**, **S. Sovilj**, **S. Šerbanović**, **B. Šolaja**, **Ž. Tešić**, **D. Trivić**, **V. Vajs**, **M. Zlatović**.

Subscription: The annual subscription rate is **150.00 €** including postage (surface mail) and handling. For Society members from abroad rate is **50.00 €**. For the proforma invoice with the instruction for bank payment contact the Society Office (E-mail: shd@shd.org.rs) or see JSCS Web Site: <http://www.shd.org.rs/JSCS/>, option Subscription.

Godišnja pretplata: Za članove SHD: **2.500,00 RSD**, za penzionere i studente: **1000,00 RSD**, a za ostale: **3.500,00 RSD**: za organizacije i ustanove: **16.000,00 RSD**. Uplate se vrše na tekući račun Društva: **205-13815-62**, poziv na broj **320**, sa naznakom "pretplata za JSCS".

Nota: Radovi čiji su svi autori članovi SHD prioritetno se publikuju.
Odlukom Odbora za hemiju Republičkog fonda za nauku Srbije, br. 66788/1 od 22.11.1990. godine, koja je kasnije potvrđena odlukom Saveta Fonda, časopis je uvršten u kategoriju međunarodnih časopisa (**M-23**). Takođe, aktom Ministarstva za nauku i tehnologiju Republike Srbije, 413-00-247/2000-01 od 15.06.2000. godine, ovaj časopis je proglašen za publikaciju od posebnog interesa za nauku. **Impact Factor** časopisa objavljen 2022. godini iznosi **1,100**, a petogodišnji **Impact Factor 1,175**.



Journal of the Serbian Chemical Society

JSCS-info@shd.org.rs • www.shd.org.rs/JSCS

J. Serb. Chem. Soc. Vol. 88, No. 3 (2023)

CONTENTS*

Organic Chemistry

- S. D. Stojanović and M. V. Zlatović: π - π Interactions in structural stability: Role in superoxide dismutases 223

Biochemistry and Biotechnology

- M. Peić Tukuljac, D. Danojević, S. Medić-Pap, J. Gvozdanović-Varga and D. Prvulović: Antioxidant response of sweet pepper fruits infected with *Alternaria alternata* 237

Theoretical Chemistry

- M. A. Matica, D. L. Roman, V. Ostafe and A. Isvoran: Deeper inside, the use of chito-oligosaccharides, in wound healing process. A computational approach 251

Physical Chemistry

- R. V. Kapustin, I. I. Grinvald, A. V. Vorotyntsev, A. N. Petukhov, V. M. Vorotyntsev, S. S. Suvorov and A. V. Baryscheva: Formation of intermediate gas-liquid system in aromatics' thin layers 267

Electrochemistry

- V. Smilyk, Y. Voloshanovska, V. Galaguz, O. Ivanenko and O. Medvezhynska: Highly efficient functional materials for modern electrochemical devices 283

Analytical Chemistry

- D. Ozdes, C. Duran, H. Bektas and E. Mentes: A facile and sensitive coprecipitation method coupled with flame atomic absorption spectrometry for quantification of Cu(II) ions in complex matrices 301

Materials

- L. Radovanović, Ž. Radovanović, B. Simović, M. V. Vasić, B. Balanč, A. Dapčević, M. Dramičanin and J. Rogan: Structure and properties of ZnO/ZnMn₂O₄ composite obtained by thermal decomposition of terephthalate precursor 313

Environmental

- G. Mosoarca, C. Vancea, S. Popa, M. E. Radulescu-Grad and S. Boran: Powdered adsorbent obtained from bathurst burr biomass for methylene blue removal from aqueous solutions 327

History of and Education in Chemistry

- F. Stašević, N. Miletić, J. Đurđević Nikolić and I. Gutman: Do Serbian high school students possess knowledge of basic chemical facts related to real life as a prerequisite for chemical literacy? 343

Published by the Serbian Chemical Society
Karnegijeva 4/III, P.O. Box 36, 11120 Belgrade, Serbia
Printed by the Faculty of Technology and Metallurgy
Karnegijeva 4, P.O. Box 35-03, 11120 Belgrade, Serbia

* For colored figures in this issue please see electronic version at the Journal Home Page:
<http://www.shd.org.rs/JSCS/>



π–π Interactions in structural stability: Role in superoxide dismutases

SRĐAN Đ. STOJANOVIĆ¹ and MARIO V. ZLATOVIĆ^{2*}#

¹*University of Belgrade – Institute of Chemistry, Technology and Metallurgy, Department of Chemistry, Belgrade, Serbia* and ²*Faculty of Chemistry, University of Belgrade, Belgrade, Serbia*

(Received 4 April, revised 25 May, accepted 11 June 2022)

Abstract: In the present work, the influences of π–π interactions in superoxide dismutase (SOD) active centers were analyzed. The majority of the aromatic residues are involved in π–π interactions. Predominant type of interacting pairs is His–His and His–Trp pairs. In addition to π–π interactions, π residues also form π-networks in SOD proteins. The π–π interactions are most favorable at the pair distance range of 5–7 Å. We observed that most of the π–π interactions shows stabilization energies in the range from −4.2 to −12.6 kJ mol^{−1}, while the metal assisted π–π interactions showed an energy in the range from −83.7 to −334.7 kJ mol^{−1}. Most of the π–π interacting residues were evolutionary conserved and thus probably important in maintaining the structural stability of proteins through these interactions. A high percentage of these residues could be considered as stabilization centers, contributing to the net stability of SOD proteins.

Keywords: superoxide dismutase; dispersive forces; catalytic site.

INTRODUCTION

Interaction between the arene systems (π – π) has been recognized as a key stabilizing force in supramolecular chemistry, drug design, biochemistry, crystal engineering and molecular science.^{1–6} Interactions between aromatic amino acid side chains are abundant in proteins, it has been reported and gained widespread acceptance that majority (about 60 %) of all the aromatic residues in proteins are involved in aromatic interactions and among them more than 80 % are involved in imparting stability to proteins.^{7,8} The nature of π – π interaction was primarily thought to be dispersive with notable electrostatic contribution depending on the system in question.⁹ At the supramolecular level, the aromatic rings can interact

* Corresponding author. E-mail: mario@chem.bg.ac.rs

Serbian Chemical Society member.

<https://doi.org/10.2298/JSC220404052S>

in different ways: stacked arrangement (face-to-face, perfect alignment, offset, slipped, parallel displaced) and edge-to-face, T-shaped conformation.¹⁰ Although $\pi-\pi$ interactions are accepted as a weak, they still play an important role in the folding and the thermal stability of proteins.^{11,12} The calculated $\pi-\pi$ interaction energies of the parallel, edge-face (T-shaped) and offset stacked are -6.2 , -10.3 and -10.4 kJ mol⁻¹, respectively,¹³ and the major source of attraction is not short range (such as charge-transfer), but long-range interactions (quadrupole-quadrupole electrostatic and dispersion).¹⁴ It has been suggested that the perpendicular and the parallel-displaced configurations are more common than the sandwich geometry as these, especially as the former one exposes three aromatic faces to the outside, offering greater possibility for additional interactions with other groups.¹⁵ Aromatic residues show a high tendency towards forming clusters beyond the dimer, having a significant influence on protein folding, structure, and stability.^{2,16}

The presented study expands on our previous work on the anion- π and cation- π interactions of SOD crystal structures by analyzing the same protein group with respect to $\pi-\pi$ interactions, in order to better understand their stabilizing role.^{17,18} We have focused our study at the SOD active centers and hence the $\pi-\pi$ interactions within a protein are not considered. Results from this study might be used for understanding of structure-function relationships and can provide a new dimension of molecular recognition and self-assembly.

EXPERIMENTAL

Dataset

For this study, we used the Protein Data Bank (PDB), accessed on May 10th, 2021, at that moment listing 183,118 resolved structures.¹⁹ The selection criteria for superoxide dismutase to be included in the dataset were as follows: 1) crystal structures of proteins containing E.C. Number 1.15.1.1 (superoxide dismutase) with metal were accepted; 2) theoretical model structures and NMR structures were not included (these structures were not accepted as it was difficult to define the accuracy of the ensemble of structures in terms of displacement that was directly comparable to the X-ray diffraction studies); 3) only crystal structures with the resolution of 2.0 Å or better and a crystallographic *R*-factor of 25.0 % or lower were accepted; 4) we included only representatives having at least 30 % sequence identity. After assembling the dataset, several structures containing ligands and mutant amino acids were rejected, leaving 43 proteins that were actually used as the dataset in our analysis. Hydrogen atoms were added and optimized, where needed, using the program Reduce,²⁰ with default settings. Reduce software adds hydrogen atoms to protein and/or DNA structures in standardized geometry, optimizing them to the orientations of OH, SH, NH₃⁺, Met methyls, Asn and Gln sidechain amides and His rings. Software determines best hydrogen positions by selecting the best overall score from all of the possible combinations, taking into the account single scores assigned for each individual residue and for groups containing movable protons partitioned in closed sets of local interacting networks. The PDB IDs of selected protein chain structures were as follows: 1ar5:A, 1cbj:A, 1d5n:A, 1hl5:A, 1ids:A, 1isa:A, 1kkc:A, 1luv:A, 1my6:A, 1qnn:A, 1srd:A, 1to4:A, 1unf:X, 1xre:A, 1xuq:A, 1y67:A, 1yai:A, 1yso:A, 2aqn:A,

2cw2:A, 2goj:A, 2rcv:A, 2w7w:A, 3ak2:A, 3ce1:A, 3dc6:A, 3evk:A, 3f7l:A, 3h1s:A, 3js4:A, 3lio:A, 3lsu:A, 3mds:A, 3pu7:A, 3tqj:A, 4br6:A, 4c7u:A, 4f2n:A, 4ffk:A, 4yet:A, 5a9g:A, 5vf9:A and 6bej:A.

π - π interaction analysis

A computer program Discovery Studio Visualizer 2020²¹ was used for the calculation of various types π - π interactions and their geometrical features with default settings (Fig. 1). π - π interactions are determined following the methodology of McGaughey.¹⁰ This method finds stacked and staggered π - π interactions by performing the following tests: 1) the distance between the centroid of each pair of π rings is determined to find those which fall within the π - π centroid (R_{cen}) cutoff distance ($R_{cen} < 7 \text{ \AA}$). For these, an atom from each ring should be within the closest atom distance (R_{clo}) cutoff distance ($R_{clo} < 7 \text{ \AA}$). The angle θ between the normal of one or both rings and the centroid-centroid vector must fall between 0° and $\pm \theta$ angle cutoff ($\theta < 90^\circ$), and the angle λ between the normal to each ring must fall between 0° and $\pm \lambda$ angle cutoff ($\lambda < 90^\circ$). The aromatic systems include the aromatic side chains of the residues tryptophan (Trp), tyrosine (Tyr), phenylalanine (Phe) and histidine (His). However, as His can act either as cation or as an aromatic moiety depending on its protonation state, in our study, both the possibilities are considered.

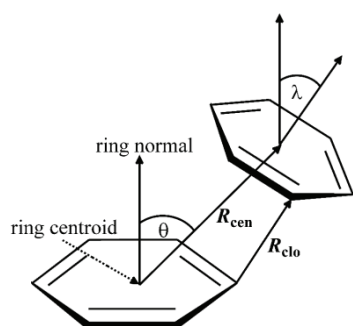


Fig. 1. Parameters for π - π interactions: (R_{cen}) the distance between the centroid of each pair of π rings; (R_{clo}) the distance between the closest atom of each π ring; (θ) the angle between the normal of one or both rings and the centroid-centroid vector; and (λ) the angle between the normal to each ring.

Computation of π - π interaction energy

In order to apply *ab initio* methods in determining the energies of π - π pairs on desired level of theory, with sufficient level of accuracy and still in satisfactory time frame, calculations were performed on structurally reduced model systems: phenylalanine was simplified to toluene (**1**), histidine to 5-methyl-1*H*-imidazole (**2**), tryptophan to 3-methyl-1*H*-indole (**3**) and tyrosine was reduced to 4-methylphenol (**4**, Fig. 2).¹⁷

Using of reduced model of large systems in calculations of specific intramolecular interaction is well known and already proved methodology,²² producing results accurate enough, and still significantly reducing computation times and strength needed for them. Larger models, like whole amino acids, or parts of protein chain, would unnecessary complicate calculations and probably even bring in the errors. Numerous interactions mechanisms are possible in a larger protein structure, and a single binding energy computation cannot always correctly determine which of these interactions are present and to what amount they contribute to overall stabilization. As a result, separating the involvement of the π - π interaction and their energy contributions from the interacting pair residues involved in other noncovalent interactions is difficult.

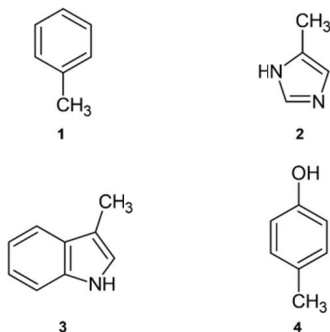


Fig. 2. Structurally reduced structures used for calculations of $\pi-\pi$ interaction energy: 1 instead of Phe; 2 instead of His; 3 instead of Trp; 4 instead of Tyr.

Ab initio calculations were performed using Jaguar from Schrödinger Suite 2018-1,²³ using LMP2 method with triple zeta Dunning's correlation consistent basis set²⁴ and ++ diffuse functions.²⁵ All calculations were performed in vacuum. The LMP2 method applied to the study of $\pi-\pi$ interactions, showed to be considerably faster than the MP2 method, while the calculated interaction energies and equilibrium distances were almost identical for both methods.²⁶ Several authors found that LMP2 represents an excellent method for calculation of interaction energies in proteins.^{27,28} Sometimes, *ab initio* calculation results can be largely influenced by BSSE, and considering it is mandatory, making the calculation times significantly longer. Local correlation methods (such as LMP2) not only reduce the cost of the calculations, but the local Møller–Plesset second-order method LMP2 is well known for reducing intramolecular BSSE.^{29–31}

Geometries of interacting structures were optimized using LMP2/cc-pVTZ(-f)++ level of theory and their single point energies calculated at LMP2/cc-pVTZ++ level. For transition metal atoms, we used the LMP2/LACVP** for geometry optimization and LMP2/LACV3P** for energy evaluation with effective core potentials (*ECPs*). The LACV3P basis set is a triple-contraction of the LACVP basis set,³² developed and tested at Schrödinger, Inc.²³ Optimized geometries were placed in space to match corresponding complexes by superimposing heavy atoms onto their respective coordinates from crystal structures and then the energies of dimeric structures produced in that way were calculated.

The $\pi-\pi$ interaction energies in dimers ($\pi-\pi$ pairs) were calculated as the difference between the energy of the complex and the sum of the energies of the monomers in their optimized geometries. The $\pi-\pi$ interaction energies in the ternary complex with metal were calculated as:

$$\Delta E_{\pi\pi} = E_{M\pi\pi} - (E_{M\pi} + E_\pi) \quad (1)$$

where $E_{M\pi\pi}$, $E_{M\pi}$ and E_π are the total energies of the ternary (metal– $\pi-\pi$), binary (metal– π) and monomeric systems (π).³³

Computation of stabilization centres

Stabilization centres (SCs) are defined as the clusters of residues making cooperative, noncovalent long-range interactions.³⁴ Measured as individual interactions, stabilisation forces resulting from noncovalent long-range interactions are not very strong, but since they are cooperative by their nature, in regions where they act in a group (SC), they could play an important role in maintaining the overall stability of protein structures. In order to analyse SC of interaction-forming residues, we used the SCide program.³⁵ The criteria SCide uses for determining SC are as follows: 1) two residues are in contact if there is, at least, one heavy atom–

–atom distance smaller than the sum of their van der Waals radii plus 1 Å; 2) a contact is recognized as “long-range” interaction if the interacting residues are, at least, ten amino acids apart; 3) two residues form a stabilization centre if they are in long-range interaction and if it is possible to select one–one residue from both flanking tetrapeptides of these two residues that make, at least, seven contacts between these two triplets.³⁴

Computation of conservation of amino acid residues

The conservation of amino acid residues in each protein was computed using the ConSurf server.³⁶ This server computes the conservation based on the comparison of the sequence of given PDB chain with the proteins deposited in Swiss–Prot database³⁷ and identifies ones that are homologous to the PDB sequence. The number of PSI–BLAST iterations and the *E*-value cut-off used in all similarity searches were 1 and 0.001, respectively. All the sequences, evolutionary related to each one of the proteins in the dataset, were used in the subsequent multiple alignments. Based on these protein sequence alignments, the residues were classified into nine categories, from highly variable to highly conserved. Residues with a score of 1 are considered to be highly variable and residues with a score of 9 are considered to be highly conserved.

RESULTS AND DISCUSSION

In this study, we have investigated the structural stability patterns of π – π interactions in active centres of SOD proteins in relation to other environmental preferences like preference of π – π interaction forming residues, interaction geometries and energetic contribution of π – π interactions, stabilization centres and conservation patterns. The analyzed protein set contains 43 protein chain crystal structures and 1116 π – π interactions, there is an average of 26 π – π interactions per active center in SOD.

Preference of aromatic residues for forming π – π interactions

We have analyzed the frequency of occurrence of aromatic amino acid residues which are involved in π – π interactions. The results are given in Table I. It can be seen that the contribution of His residue exceeds those of other three aromatic residues. The reason for this could be because, of all the aromatic amino acids, His occurs most frequently in both coordination spheres of SOD active centres.^{17,38} The number of interactions involving other aromatic residues is similar. We compared the occurrence of interacting pairs to find the preference by SOD proteins (Table I). The highest percentage of interactions are seen between His–His pairs. Among the hetero-pairs, the occurrences of His–Trp pair are more frequent than other interacting pairs. Hence, these interactions may be quite important in the structural stability of SOD proteins.

A larger π -network will add more stability and play an important role in understanding the structure of proteins.³⁹ We analyzed the π – π networks in these proteins as well. The analysis showed that about 73 % of the total π – π interactions in the dataset are involved in the formation of multiple π interactions. The connectivity of π -ring is found to increase along the length of a network from 2π

to 7π . A large π -network can enhance the stability of a protein conformation and can have a considerable influence on protein–ligand interactions. It has also been shown that addition of an aromatic pair on the protein surface increases its stability.⁴⁰ An illustrative example of a typical 7π -network of cambialistic SOD from *Propionibacterium shermanii* is shown in Fig. 3.

TABLE I. Frequency of occurrence of π – π interaction-forming residues in active centers of superoxide dismutase

Residue	Number of occurrences ^a	Occurrence ^b , %
His	1067	47.80
Phe	256	11.47
Trp	510	22.85
Tyr	399	17.88
Total	2232	100
Interacting pair		
His–His	344	30.82
His–Phe	64	5.73
His–Trp	204	18.28
His–Tyr	111	9.95
Phe–Phe	28	2.51
Phe–Trp	93	8.33
Phe–Tyr	43	3.85
Trp–Trp	69	6.18
Trp–Tyr	75	6.72
Tyr–Tyr	85	7.63
Total	1116	100

^aThe number of times a particular amino acid occurs in an appropriate interaction; ^bpercent of amino acid occurs in an appropriate interaction

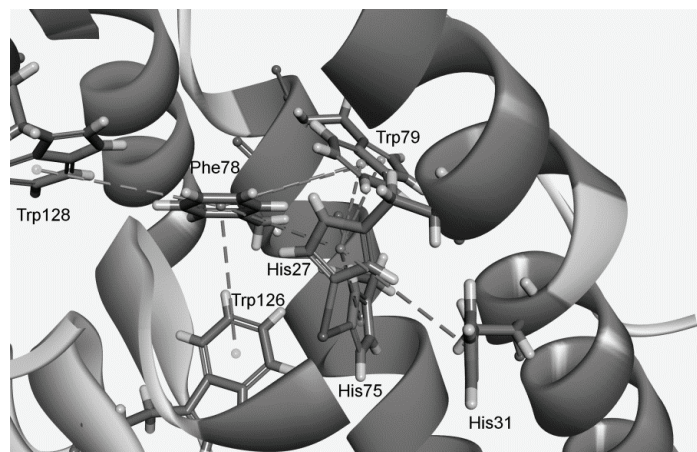


Fig. 3. Example of a multiple π interactions (π -network) for the cambialistic SOD from *Propionibacterium shermanii* (PDB code 1ar5); The interactions are marked with a dashed lines (color version is given in Supplementary material to this paper).

Interaction geometries and energetic contribution of π - π interactions

On the basis of orientation of the aromatic rings, the π - π interactions between two aromatic species have been broadly classified into three categories: edge to face (T-shaped), parallel displaced, and parallel stacked.⁴¹ For example, McGaughey *et al.* analyzed 505 proteins and determined that an offset parallel-stacked conformation was on average 4.2 kJ mol⁻¹ more stabilizing than a T-shaped geometry.^{10,42} We have also analyzed the frequency distribution of the distance and angle parameters of π - π interacting pairs. These results are shown in

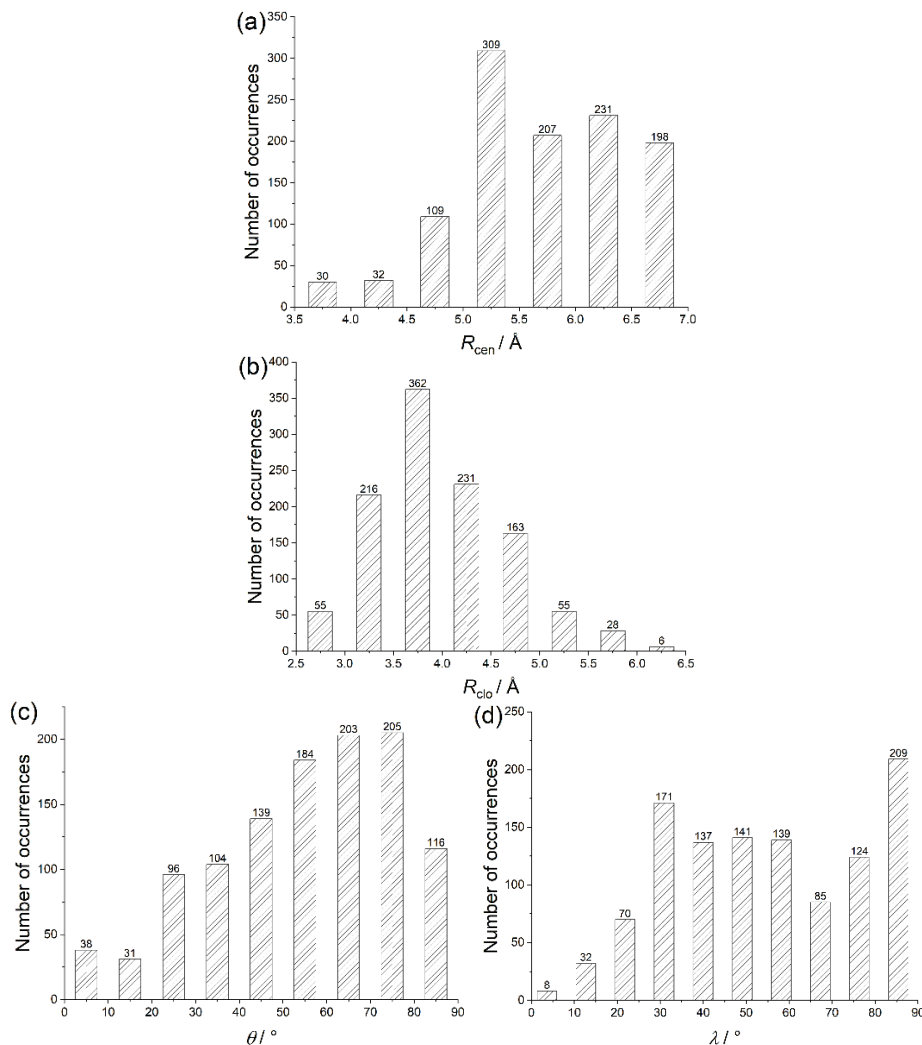


Fig. 4. Interaction geometries of π - π interactions in SOD: a) R_{cen} distance distribution, b) R_{clo} distance distribution c) θ angle distribution, d) λ angle distribution.

Figs. 4 and 5. The distribution of the centroid–centroid distance (R_{cen}) for π – π interactions was found to be most favorable in the distance range of 5–7 Å (Fig. 4a). This is because of T-shaped orientations having a longer R_{cen} than parallel orientations. At separation distances below 4.5 Å, aromatic pairs are rarely observed, a result of obvious physical constraints. The plot of R_{clo} distance distribution derived from π – π interaction pairs (Fig. 4b), shows distribution mainly below 5.0 Å. An analysis of the plane–plane angles (θ) indicate that coplanarity, capable to maximizing π – π stacking and packing,⁴³ was observed in relatively high number of cases (Fig. 4c). An analysis of angle λ showed a preference for T-shaped orientations with angles above 30° (Fig. 4d). The native structure is the compromise of a large number of noncovalent interactions that exist in proteins and the geometrical features relating two residue-types are expected to be rather broad. Overall, there was no clear overall preference for either “stacked” or “T-shaped” arrangements. For the latter, a clear orientational preference has not been determined experimentally.^{44,45}

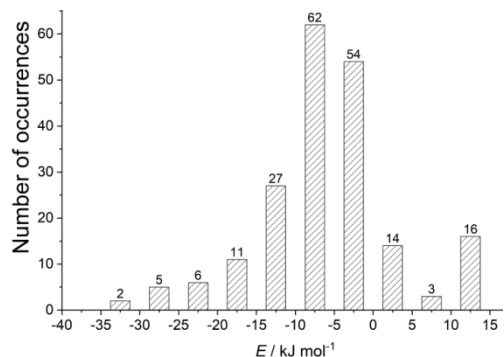


Fig. 5. Interaction energies of π – π interactions in SOD.

To estimate the stabilization energy of the different π – π pairs, energy calculations were carried out. To avoid calculation of more than 1000 interactions, we carefully selected 200 structures representing almost all the interactions which had been found. The results of calculations of the interaction energies for all possible interacting pairs are presented in Fig. 5.

The calculated energies range between –33.5 and 16.7 kJ mol^{–1}, with a most populated bin in the range from –4.2 to –12.6 kJ mol^{–1}. The energies calculated for many of the π – π interactions are substantially stabilizing, with 16 % of the total showing positive (repulsive) predicted interaction energies. The repulsive nature of those interactions emerges from the unfavourable geometries of π – π interactions in the crystal structures and is usually counterbalanced by other interactions.¹⁷ The strongest attractive interaction (–32.7 kJ mol^{–1}) arises for the His27–Tyr11 pair in MnSOD structure from *Escherichia coli* (PDB code 1d5n; Fig. 6a). The energies associated with π – π interactions may be important contri-

butors to the overall stability of biomolecular structures and complexes and to their function through substrate binding and protein–protein interactions.

As support for the context of the π – π interactions in the protein structure affecting the energetics of the system, we have analyzed the occurrence of M– π – π (M = Zn²⁺) interactions in the dataset and found 40 cation– π interactions between Zn²⁺ and the π systems of surrounding amino acids. For these ternary complexes the interaction energies are large (at least ten times larger than those calculated for individually interactions). The π – π interaction energies are large and negative, ranging from –83.7 to –334.7 kJ mol^{–1} due to the strong electrostatic effect caused by the proximity of the metal centre, thus revealing a synergistic effect between the different interactions. Quantum chemical calculations indicate that the metal ion assisted π – π interaction strengths may become comparable in magnitude to that of the hydrogen bonding interaction. From our results on the interplay between cation– π and π – π interactions we suggest that these interactions can provide additional stability to the SOD proteins. Due to the presence of a great number of cation– π and π – π interactions in biological systems, this effect is important and helps to understand some biological processes where the interplay between both interactions exist. It also should be taken into account in supramolecular chemistry and crystal engineering fields.³⁹

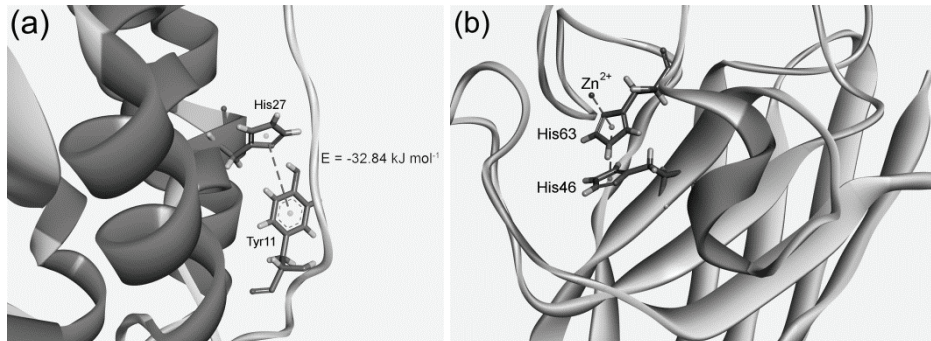


Fig. 6. Details of π – π interactions: a) the strongest attractive π – π interaction of *Escherichia coli* MnSOD (PDB code 1d5n). The interaction is marked with a dashed line: A:His27–A:Tyr11; $R_{\text{cen}} = 5.70 \text{ \AA}$, $R_{\text{clo}} = 3.61 \text{ \AA}$, $\theta = 59.77^\circ$, $\lambda = 51.92^\circ$, $E = -32.7 \text{ kJ mol}^{-1}$; b) interaction energy of π – π interaction in the presence of metal cation (Zn²⁺) in Cu/Zn tomato chloroplast SOD (PDB code 3pu7): A:Zn²⁺–A:His27–A:Tyr11; $R_{\text{cen}} = 3.97 \text{ \AA}$, $R_{\text{clo}} = 2.98 \text{ \AA}$, $\theta = 26.01^\circ$, $\lambda = 41.21^\circ$, $E = -327.7 \text{ kJ mol}^{-1}$ (color version in SM).

In Fig. 6b, we showed structural details of the π – π interaction involving transition metal ion of bovine Cu/Zn Tomato Chloroplast SOD (PDB code 3pu7). The degree of cooperativity of cation– π and π – π interaction may be quantified by comparing interaction energies in the absence of Zn²⁺ (–19.3 kJ mol^{–1}) and in the presence of this cation (–327.7 kJ mol^{–1}).

Stabilization centres and conservation of amino acid residues

Proteins should have well-balanced stability allowing structural fluctuations and concomitantly ensuring the long-lasting equilibrium structure. Residues can be considered part of stabilization centers if they are involved in medium or long-range interactions.³⁴ We have computed the stabilization centers for all π - π interaction forming residues in SOD active centers. Considering the whole data set, 45.2 % of all stabilizing residues are involved in building π - π interactions. It was interesting to note that all residues involved in π - π interactions were included in at least one stabilization center. These observations strongly reveal that these residues may contribute significantly to the structural stability of these proteins in addition to participating in π - π interactions.

The level of evolutionary conservation was often used as an indicator for the importance of certain position in maintaining the protein's structure and/or function.⁴⁶ Among the π - π interacting residues, 74.6 % of them showed a conservation score of higher or equal to 6. From our results we are able to infer that most of the amino acid residues involved in π - π interactions might be evolutionarily conserved and might have a significant contribution to the stability of SOD proteins.

CONCLUSION

In the present study, the analysis of the role of π - π interactions in SOD proteins indicate that most of the aromatic residues are involved in π - π interactions and contribute significantly to the structural stability of SOD proteins. Considering the individual contribution of aromatic residues towards π - π interactions, His residues are found to have exceeded the other three aromatic amino acids. Among the interacting pairs, the His-His and His-Trp pairs have the highest frequency of occurrence than other pairs. The significant number of π - π interacting residues identified in the dataset is involved in the formation of π -networks. We also find that all these interacting pairs are favorable in the distance range of 5–7 Å. An analysis of the plane-plane angles indicate no clear overall preference for either the “stacked” or “T-shaped” arrangements. The analysis of the energetic contribution of the protein interacting residues has revealed that most of the π - π interactions have an energy in the range -4.2 to -12.6 kJ mol⁻¹. The strongest interactions (from -83.7 to -334.7 kJ mol⁻¹) arise for the metal assisted π - π interactions. We found that, all the residues found in π - π interactions are important in locating one or more stabilization centers, 45.2 % of all stabilizing residues are involved in building π - π interactions, providing an additional stabilization of the SOD proteins. Moreover, the majority of the residues (74.6 %) involved in π - π interactions were evolutionarily conserved. In conclusion, the results obtained from this study will be very helpful in further understanding the structural stability and functions of SOD proteins.

SUPPLEMENTARY MATERIAL

Additional data and information are available electronically at the pages of journal website: <https://www.shd-pub.org.rs/index.php/JSCS/article/view/11744>, or from the corresponding author on request.

Acknowledgement. The authors would like to thank the Ministry of Education, Science and Technological Development of Republic of Serbia (Grant No: 451-03-68/2022-14/200026 and 451-03-68/2022-14/200168) for financial support.

ИЗВОД
ИСПИТИВАЊЕ УЛОГЕ КАТЈОН- π ИНТЕРАКЦИЈА У АКТИВНИМ ЦЕНТРИМА
СУПЕРОКСИД-ДИСМУТАЗА

СРЂАН Ђ. СТОЈАНОВИЋ¹ и МАРИО В. ЗЛАТОВИЋ²

¹Универзитет у Београду – Институт за хемију, технологију и металургију, Београд и ²Хемијски факултет, Универзитет у Београду, Београд

У овом раду анализирани су утицаји π - π интеракција у активним центрима супероксид-дисмутазе (SOD). Већина ароматичних остатака је укључена у π - π интеракције. Парови His-His и His-Trp су доминантни тип парова у интеракцији. Поред π - π интеракција, π остаци такође формирају π -мреже у SOD протеинима. π - π интерагујући парови су најповољнији у опсегу дистанци од 5–7 Å. Приметили смо да већина π - π интеракција има енергију у опсегу од -4,2 до -12,6 kJ mol⁻¹, док су π - π интеракције уз асистенцију метала показале енергију у опсегу -83,7 до -334,7 kJ mol⁻¹. Већина π - π интерагујућих остатака били су еволутивно конзервирани и могли би бити важни у одржавању структурне стабилности кроз ове интеракције. Висок проценат ових остатака може се сматрати стабилизационим центрима који доприносе нето стабилности SOD протеина.

(Примљено 4. априла, ревидирано 25. маја, прихваћено 11. јуна 2022)

REFERENCES

1. C. D. Andersson, B. K. Mishra, N. Forsgren, F. Ekström, A. Linusson, *J. Phys. Chem., B* **124** (2020) 6529 (<https://doi.org/10.1021/acs.jpcb.0c03778>)
2. E. Lanzarotti, L. A. Defelipe, M. A. Martí, A. n. G. Turjanski, *J. Cheminf.* **12** (2020) 30 (<https://doi.org/10.1186/s13321-020-00437-4>)
3. K. S. Chatterjee, R. Das, *J. Biol. Chem.* **297** (2021) (<https://doi.org/10.1016/j.jbc.2021.100970>)
4. H. B. Gray, J. R. Winkler, *Chem. Sci.* **12** (2021) 13988 (<https://doi.org/10.1039/D1SC04286F>)
5. Z. Y. Yan, X. J. Xu, L. Fang, C. Geng, Y. P. Tian, X. D. Li, *Phytopathol. Res.* **3** (2021) 10 (<https://doi.org/10.1186/s42483-021-00088-9>)
6. S. Sasidharan, V. Ramakrishnan, *Aromatic interactions directing peptide nano-assembly. Advances in Protein Chemistry and Structural Biology*. Academic Press, Cambridge, MA, 2022 (<https://doi.org/10.1016/bs.apcsb.2022.01.001>)
7. S. K. Burley, G. A. Petsko, *Science* **229** (1985) 23 (<https://www.science.org/doi/10.1126/science.8235619>)
8. E. Cauët, M. Rooman, R. Wintjens, J. Liévin, C. Biot, *J. Chem. Theory Comput.* **1** (2005) 472 (<https://doi.org/10.1021/ct049875k>)
9. M. O. Sinnokrot, C. D. Sherrill, *J. Am. Chem. Soc.* **126** (2004) 7690 (<https://doi.org/10.1021/ja049434a>)

10. G. B. McGaughey, M. Gagné, A. K. Rappé, *J. Biol. Chem.* **273** (1998) 15458 (<https://doi.org/10.1074/jbc.273.25.15458>)
11. R. Bhattacharyya, U. Samanta, P. Chakrabarti, *Protein Eng.* **15** (2002) 91 (<https://doi.org/10.1093/protein/15.2.91>)
12. N. Kannan, S. Vishveshwara, *Protein Eng.* **13** (2000) 753 (<https://doi.org/10.1093/protein/13.11.753>)
13. S. Tsuzuki, K. Honda, T. Uchimaru, M. Mikami, K. Tanabe, *J. Am. Chem. Soc.* **124** (2002) 104 (<https://doi.org/10.1021/ja0105212>)
14. A. V. Morozov, K. M. S. Misura, K. Tsemekhman, D. Baker, *J. Phys. Chem., B* **108** (2004) 8489 (<https://doi.org/10.1021/jp037711e>)
15. C. Chipot, R. Jaffe, B. Maigret, D. A. Pearlman, P. A. Kollman, *J. Am. Chem. Soc.* **118** (1996) 11217 (<https://doi.org/10.1021/ja961379l>)
16. E. Lanzarotti, R. R. Biekofsky, D. O. A. Estrin, M. A. Marti, A. n. G. Turjanski, *J. Chem. Inf. Model.* **51** (2011) 1623 (<https://doi.org/10.1021/ci200062e>)
17. V. R. Ribić, S. Đ. Stojanović, M. V. Zlatović, *Int. J. Biol. Macromol.* **106** (2018) 559 (<https://doi.org/10.1016/j.ijbiomac.2017.08.050>)
18. S. Stojanović, M. Zlatović, *J. Serb. Chem. Soc.* **87** (2022) 465 (<https://doi.org/10.2298/JSC220109013S>)
19. P. W. Rose, B. Beran, C. Bi, W. F. Bluhm, D. Dimitropoulos, D. S. Goodsell, A. Prlic, M. Quesada, G. B. Quinn, J. D. Westbrook, J. Young, B. Yukich, C. Zardecki, H. M. Berman, P. E. Bourne, *Nucleic Acids Res.* **39** (2011) D392 (<https://doi.org/10.1093/nar/gkq1021>)
20. J. M. Word, S. C. Lovell, J. S. Richardson, D. C. Richardson, *J. Mol. Biol.* **285** (1999) 1735 (<https://doi.org/10.1006/jmbi.1998.2401>)
21. *Discovery Studio Visualizer*, Release 2020. Accelrys Software Inc., San Diego, CA
22. J. Hostaš, D. Jakubec, R. A. Laskowski, R. Gnanasekaran, J. Řezáč, J. Vondrášek, P. Hobza, *J. Chem. Theory. Comput.* **11** (2015) 4086 (<http://dx.doi.org/10.1021/acs.jctc.5b00398>)
23. *Schrödinger*, Release 2018-1: Jaguar, Schrödinger, LLC, New York, 2018
24. T. H. Dunning, *J. Chem. Phys.* **90** (1989) 1007 (<https://doi.org/10.1063/1.456153>)
25. T. Clark, J. Chandrasekhar, G. n. W. Spitznagel, P. V. R. Schleyer, *J. Comput. Chem.* **4** (1983) 294 (<https://doi.org/10.1002/jcc.540040303>)
26. A. D. Bochevarov, E. Harder, T. F. Hughes, J. R. Greenwood, D. A. Braden, D. M. Philipp, D. Rinaldo, M. D. Halls, J. Zhang, R. A. Friesner, *Int. J. Quantum Chem.* **113** (2013) 2110 (<https://doi.org/10.1002/qua.24481>)
27. K. E. Riley, J. A. Platts, J. Řezáč, P. Hobza, J. G. Hill, *J. Phys. Chem., A* **116** (2012) 4159 (<https://doi.org/10.1021/jp211997b>)
28. G. J. Jones, A. Robertazzi, J. A. Platts, *J. Phys. Chem., B* **117** (2013) 3315 (<https://doi.org/10.1021/jp400345s>)
29. S. Saebø, W. Tong, P. Pulay, *J. Chem. Phys.* **98** (1993) 2170 (<https://doi.org/10.1063/1.464195>)
30. A. Reyes, L. Fomina, L. Rumsh, S. Fomine, *Int. J. Quantum Chem.* **104** (2005) 335 (<https://doi.org/10.1002/qua.20558>)
31. R. M. Balabin, *J. Chem. Phys.* **132** (2010) 231101 (<https://doi.org/10.1063/1.3442466>)
32. P. J. Hay, W. R. Wadt, *J. Chem. Phys.* **82** (1985) 299 (<https://doi.org/10.1063/1.448975>)
33. D. Vijay, G. N. Sastry, *Chem. Phys. Lett.* **485** (2010) 235 (<https://doi.org/10.1016/j.cplett.2009.12.012>)

34. Z. Dosztányi, A. Fiser, I. Simon, *J. Mol. Biol.* **272** (1997) 597 (<https://doi.org/10.1006/jmbi.1997.1242>)
35. Z. Dosztányi, C. Magyar, G. Tusnady, I. Simon, *Bioinformatics* **19** (2003) 899 (<https://doi.org/10.1093/bioinformatics/btg110>)
36. H. Ashkenazy, E. Erez, E. Martz, T. Pupko, N. Ben-Tal, *Nucleic Acids Res.* **38** (2010) W529 (<https://doi.org/10.1093/nar/gkq399>)
37. B. Boeckmann, A. Bairoch, R. Apweiler, M. C. Blatter, A. Estreicher, E. Gasteiger, M. J. Martin, K. Michoud, C. O'Donovan, I. Phan, S. Pilbouth, M. Schneider, *Nucleic Acids Res.* **31** (2003) 365 (<https://doi.org/10.1093/nar/gkg095>)
38. S. Stojanović, Z. Petrović, M. Zlatović, *J. Serb. Chem. Soc.* **86** (2021) 781 (<https://doi.org/10.2298/JSC210321042S>)
39. A. S. Mahadevi, G. N. Sastry, *Chem. Rev.* **116** (2016) 2775 (<https://doi.org/10.1021/cr500344e>)
40. B. Ma, T. Elkayam, H. Wolfson, R. Nussinov, *Proc. Natl. Acad. Sci. USA* **100** (2003) 5772 (<https://doi.org/10.1073/pnas.1030237100>)
41. E. G. Hohenstein, C. D. Sherrill, *J. Phys. Chem., A* **113** (2009) 878 (<https://doi.org/10.1021/jp809062x>)
42. P. Chakrabarti, R. Bhattacharyya, *Prog. Biophys. Mol. Biol.* **95** (2007) 83 (<https://doi.org/10.1016/j.pbiomolbio.2007.03.016>)
43. S. Marsili, R. Chelli, V. Schettino, P. Procacci, *Phys. Chem. Chem. Phys.* **10** (2008) 2673 (<https://doi.org/10.1039/B718519G>)
44. S. Ishikawa, T. Ebata, H. Ishikawa, T. Inoue, N. Mikami, *J. Phys. Chem.* **100** (1996) 10531 (<https://doi.org/10.1021/jp960267d>)
45. A. Banerjee, A. Saha, B. K. Saha, *Crystal Growth Design* **19** (2019) 2245 (<https://doi.org/10.1021/acs.cgd.8b01857>)
46. M. Landau, I. Mayrose, Y. Rosenberg, F. Glaser, E. Martz, T. Pupko, N. Ben-Tal, *Nucleic Acids Res.* **33** (2005) W299-W302 (<https://doi.org/10.1093/nar/gki370>).

SUPPLEMENTARY MATERIAL TO
 **π – π interactions in structural stability: Role in superoxide
dismutases**

SRĐAN Đ. STOJANOVIĆ¹ and MARIO V. ZLATOVIĆ^{2*}#

¹*University of Belgrade – Institute of Chemistry, Technology and Metallurgy, Department of Chemistry, Belgrade, Serbia* and ²*Faculty of Chemistry, University of Belgrade, Belgrade, Serbia*

J. Serb. Chem. Soc. 88 (3) (2023) 223–235

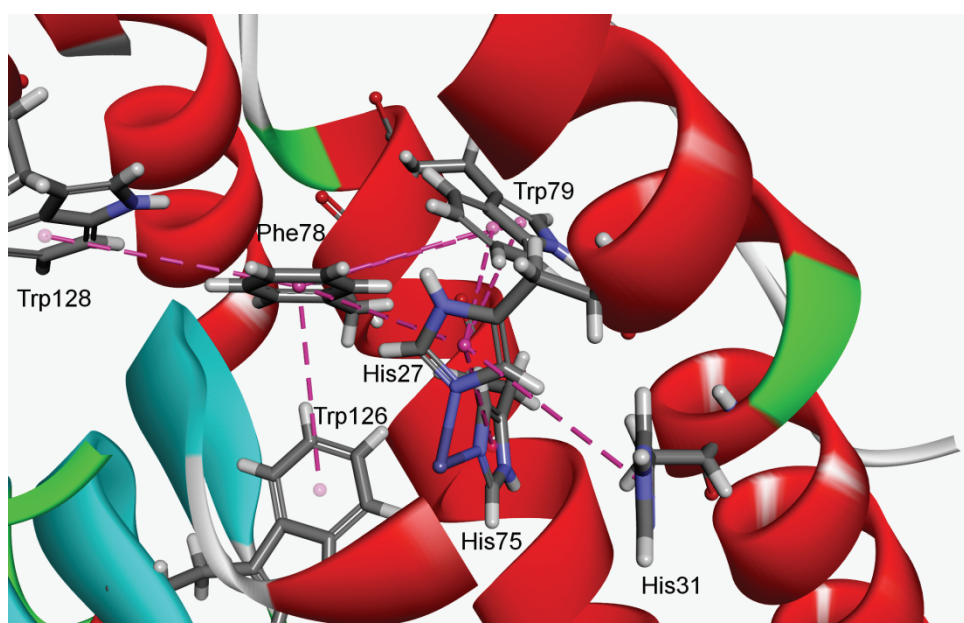


Fig. S-1. Example of a multiple π interactions (π -network) for the cambialistic SOD from *Propionibacterium shermanii* (PDB code 1ar5); The interactions are marked with a pink dashed lines.

* Corresponding author. E-mail: mario@chem.bg.ac.rs

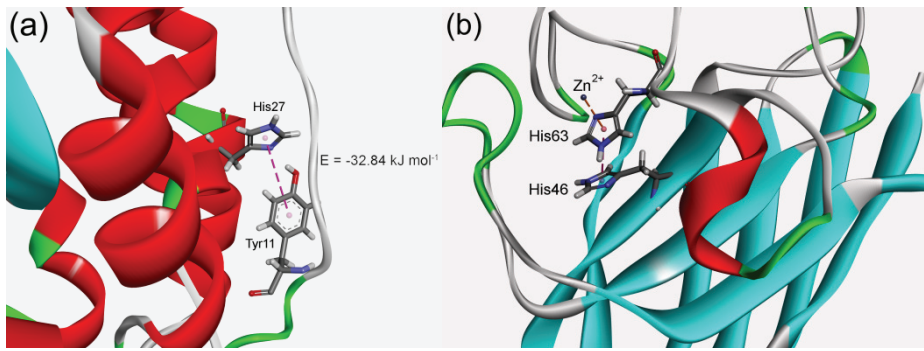


Fig. S-2. Details of $\pi-\pi$ interactions: a) The strongest attractive $\pi-\pi$ interaction of *Escherichia coli* MnSOD (PDB code 1d5n). The interaction is marked with a pink dashed line: A:His27—A:Tyr11; $R_{cen} = 5.70 \text{ \AA}$, $R_{clo} = 3.61 \text{ \AA}$, $\theta = 59.77^\circ$, $\lambda = 51.92^\circ$, $E = -32.7 \text{ kJ mol}^{-1}$; b) Interaction energy of $\pi-\pi$ interaction in the presence of metal cation (Zn^{2+}) in Cu/Zn Tomato Chloroplast SOD (PDB code 3pu7): A: Zn^{2+} —A:His27—A:Tyr11; $R_{cen} = 3.97 \text{ \AA}$, $R_{clo} = 2.98 \text{ \AA}$, $\theta = 26.01^\circ$, $\lambda = 41.21^\circ$, $E = -327.7 \text{ kJ mol}^{-1}$.



Antioxidant response of sweet pepper fruits infected with *Alternaria alternata*

MARIJANA PEIĆ TUKULJAC^{1*}, DARIO DANOJEVIĆ², SLAĐANA MEDIĆ-PAP²,
JELICA GVOZDANOVIĆ-VARGA² and DEJAN PRVULOVIĆ¹

¹University of Novi Sad, Faculty of Agriculture, Trg D. Obradovića 8, 21000 Novi Sad, Serbia
and ²Institute of Field and Vegetable Crops Novi Sad, M. Gorkog 30, 21000 Novi Sad, Serbia

(Received 15 November, revised 23 December, accepted 24 December 2022)

Abstract: *Capsicum annuum* is valuable source of many bioactive compounds with the protective role in plants against biotic and abiotic stress as well as beneficial effect on humans' health. This vegetable is susceptible to many infections, including postharvest decay caused by fungus *Alternaria alternata*. In order to better understanding pepper fruits defense system, the concentration of phenols and ascorbic acid, scavenging activity and antioxidant enzyme activity in three kapia type sweet pepper fruits (Amfora, Una and Kurtovka kapia) infected with fungus *A. alternata* were determined in this study. Amfora fruits had the highest tolerance to *Alternaria* infection. Amfora and Una increase total phenol and vitamin C content after wounding and inoculation, while Kurtovska kapia decreased amount of vitamin C. Depending on reaction mechanism, antioxidant tests showed no changes or decrease in antioxidant capacity in treated fruits. Except for phenylalanine ammonia-lyase activity in Amfora and Kurtovska kapia and ascorbate peroxidase activity in wounded Kurtovska kapia fruits, all measured enzyme activity showed no changes or decrease by wounding and/or *Alternaria* infection. According to results of intensity of lipid peroxidation as biological marker of oxidative stress, it can be concluded that wounding and infection disturb redox balance in all examined genotypes. The tested genotypes showed certain difference in antioxidant defence against wounding and pathogen stress.

Keywords: *Capsicum annuum*; non-enzymatic antioxidants; *Alternaria* infection; oxidative stress; antioxidant enzymes.

INTRODUCTION

Pepper (*Capsicum annuum* L.) is a member of *Solanaceae* family¹ and globally adopted important horticultural crop. Besides their nutritional value, Capsicum fruits have health-protective effect. They are a significant source of min-

* Corresponding author. E-mail: marijana.peic@polj.uns.ac.rs
<https://doi.org/10.2298/JSC221115091P>

erals, vitamins, carotenoids, capsaicinoids and phenolic compounds with a beneficial effect on human health due to their antioxidant properties as well as ability to protect cells against damages caused by oxidative stress and prevent development of illness such as cardiovascular deceases, Parkinson's, Alzheimer's, cancer and diabetes.²

On the other side, many abiotic and biotic stress factors affect the production of *Capsicum* species, including a great number of fungi. The following fungal species: *Fusarium solani*, *Fusarium subglutinans*, *Alternaria alternata*, *Alternaria tenuis*, *Botrytis cinerea*, *Colletotrichum* species complex and *Verticillium* spp are the common causal agents of pepper fruit rots.³ The numerous *Alternaria* species are known as widespread plant pathogens of various types of horticultural crops, responsible for significant economic losses. *A. alternata* is the main causal agent of diseases of different vegetable species including internal mold in *Capsicum annuum*.⁴

In plants, pathogen infections provoke the production of reactive oxygen species (ROS) as one of the earliest responses in pathogen-plant interaction. ROS are by-product of aerobic metabolism and have a role as a messenger in signal transduction, regulation of metabolism, or memory formation *via* DNA methylation.⁵ The main ROS in cells includes free radicals such as superoxide anion ($\cdot\text{O}_2^-$), hydroxyl radical ($\cdot\text{OH}$), and molecular non-radical forms – singlet oxygen ($^1\text{O}_2$) and hydrogen peroxide (H_2O_2). ROS overproduction under unfavourable conditions: extreme temperatures, heavy metals, drought, salinity (abiotic stress) or pathogen infection (biotic stress), lead to oxidative stress and cause damages to major macromolecules, *i.e.*, proteins, lipids and nucleic acid.⁶ In order to manage cascades of uncontrolled oxidation and protect plant cells from oxidative damage, plants possess potent non-enzymatic (phenolic compounds, tocopherols, carotenoids, glutathione (GSH), ascorbic acid (AA)) and enzymatic antioxidant defense system (superoxide dismutase (SOD), catalase (CAT), guaiacol peroxidase (GPX), ascorbate peroxidase (APX), monodehydroascorbate reductase (MDHAR), dehydroascorbate reductase (DHAR) and glutathione reductase (GR)).⁷

Knowledge of the relationship between the level of bioactive compounds and the antioxidant activity of sweet pepper could lead to a better understanding of pepper fruits defense system against infection. The aim of our study was to determine the concentration of phenolic compounds and ascorbic acid, scavenging activity as well as antioxidant enzyme activity in three different genotypes of kapia type sweet pepper fruits infected with fungus *A. alternata*.

EXPERIMENTAL

Collection of plant material and inoculation procedure

As plant material in this study, fruits of three different sweet peppers genotypes, Amfora, Una and Kurtovska kapia was used. The fruits were grown in the experimental field of the Institute of Field and Vegetable Crops, Novi Sad, Serbia, in 2019 and harvested on the 16th of

October at technological maturity. Typical fruits without visible injury were selected and kept in cold storage during the night. Pericarp thickness, fruit length, width and weight were measured on 21 fruits from each genotype.

Nine selected fruits of each genotype for the disease assessment were divided into three groups: the intact fruits (control group); the fruits injected with sterile water and fruits inoculated with a fungal spore suspension. The inoculation was done following the procedure described by Fallik *et al.*⁸ For the inoculation monohyphal isolate (K-93) of *A. alternata*, originated from infected pepper fruit was used. The isolate was identified by polymerase chain reaction (PCR) method and preliminary pathogenicity test was done before the experiment. The spore suspension (10^5 conidia/ml) of the 10 days isolate grown on potato-dextrose-agar at 20 °C was used in inoculation process. Six fruits of each genotype were wounded at 3 points and inoculated by pipetting 40 µl sterile water (3 fruits) or spore suspension in each puncture (3 fruits). Intact fruits were used as a control. The fruits were put into PVC bags (due to obtain high humidity) and incubated at 20 °C for 10 days. The fruit assessment was done 10 days after inoculation. In order to evaluate the rate of the severity of fungal infection on pepper fruits, internal and external lesion diameters as well as mycelium were measured by vernier caliper.⁹ Also, the surface area of lesions and mycelia were calculated according to the formula for the area of a circle. After disease assessment fruits were cut into small pieces and stored at -70 °C until the biochemical analyses were performed.

Sample extraction

Total reduction capacity (TRC), 2,2-diphenyl-1-picrylhydrazyl (DPPH) and nitroblue tetrazolium (NBT) assays were performed and total phenolic content was determined in methanol extracts of fruits. 4 g plant material was homogenized with 10 ml of 70 % aqueous methanol solution and after 24 h centrifuged at 5000 rpm for 15 min. Separated supernatant was kept in cold storage. PAL, SOD, CAT, APX, GPX and propoxyphene (PPX) activity assays and lipid peroxidation (LP) were measured in phosphate buffer extract prepared by extraction 2 g plant material with 10 ml 0.1 M phosphate buffer (pH 7.0). After the centrifugation (5000 rpm) at 4 °C for 15 min, supernatant was separated and kept in cold storage.

Biochemical assays

Folin-Ciocalteau method was used to evaluate the total phenolic content following the procedure described by Wootton-Beard *et al.*¹⁰ with slight modification. The results were expressed as quercetin equivalents in mg per 100 g of fresh weight (mg QE (100 g FW)⁻¹). The level of vitamin C in sweet pepper samples was estimated by spectrophotometric measurements.¹¹ Extracts for this assay were prepared by weighing 1 g of sweet pepper fruits, homogenized with 10 ml 5 % metaphosphoric acid + 10 % acetic acid solution. The supernatant was used for the assay. The content of vitamin C was expressed as ascorbic acid equivalents in mg per 100 g of fresh weight (mg AA (100 g FW)⁻¹).

Antioxidant activity

DPPH assay was carried out by the method based on reaction between stable DPPH radical and a substance that can donate a hydrogen atom as described by Floegel *et al.*¹² TRC was obtained as Govindan and Muthukrishnan¹³ previously described with some modifications. The results of antioxidant activity estimated by DPPH and TRC were expressed as mg of Trolox equivalents per 100 g of fresh weight (mg Trolox (100 g FW)⁻¹). The methanol extract was used to estimate superoxide radical scavenging activity, while phosphate buffer was used to determine superoxide dismutase (SOD, EC 1.15.1.1) enzyme activity, while both assays were performed following the same procedure.¹⁴ The results of superoxide radical scavenging

activity were expressed as the percentage inhibition of superoxide anion generation. SOD enzyme activity was expressed as units per mg of protein ($\text{U} (\text{mg protein})^{-1}$). A Bradford¹⁵ method was used to quantify the total protein content and for the construction of standard curve different concentrations of albumin were taken. The total protein content was reported as protein equivalents in mg per g of fresh weight ($\text{mg protein (g FW)}^{-1}$).

Antioxidant enzyme assays

Catalase enzyme activity (CAT; EC 1.11.1.6) was determined according to the method of Aebi,¹⁶ based on decreasing absorbance measured at 240 nm due to the dismutation of H_2O_2 . The results were reported as units per mg of protein ($\text{U} (\text{mg protein})^{-1}$) where one unit of CAT activity was defined as the amount of enzyme that caused the composition of one μmol of H_2O_2 per min at 25 °C. Ascorbate peroxidase (APX; EC 1.11.1.11) activity was assayed according to the protocol of Nakano and Asada.¹⁷ A decrease in absorbance was recorded at 290 nm for 5 min and the APX activity was expressed as units per mg of protein ($\text{U} (\text{mg protein})^{-1}$). For the measurement of guaiacol (GPX; EC 1.11.1.7) and pyrogallol peroxidase (PPX; EC 1.11.1.7) activity, Morkunas and Gmerek¹⁸ methods were used, and substrate oxidation was followed by the decrease in the absorbance at 470 and 420, respectively. The GPX and PPX activities were expressed as units per mg of protein ($\text{U} (\text{mg protein})^{-1}$). A protocol of Gerasimova *et al.*¹⁹ was used to determine phenylalanine ammonia-lyase (PAL; EC 4.3.1.5). The PAL activity was expressed as *trans*-cinnamic acid equivalents in mg per 100 g of fresh weight ($\text{mg tCA (100 g FW)}^{-1}$).

Lipid peroxidation

The intensity of lipid peroxidation was assayed by the protocol of Heath and Packer.²⁰ The level of LP was expressed as μmol malondialdehyde (MDA) equivalents per mg protein ($\mu\text{mol MDA (mg protein)}^{-1}$).

Statistical analysis

The data were analyzed using TIBCO Data Science-Statistica software. The normality of obtained values was tested using Shapiro-Wilk (SW) test. Given that values of diameters and area of mycelia as well as lesion did not show normal distribution, for comparing samples non-parametric Kruskal-Wallis (KW) test and Mann-Whitney U test were used. Values of morphometric parameters and biochemical assays were tested by ANOVA. In the case of biochemical assays, a comparison of means was done by the Bonferroni *post hoc* test ($p < 0.05$), while for morphometric parameters was used Fisher least significant difference (LSD) *post hoc* test ($p < 0.05$). All the evaluated parameters and their importance in the fruit-pathogen interaction was investigated by the principal component analysis (PCA).

On the graphs, results are expressed as the mean \pm standard deviation of three independent samples. Different letters within one genotype represent statistically significant differences between treatments ($p < 0.05$).

RESULTS AND DISCUSSION

All tested genotypes have elongated fruits and intensively red at physiological maturity. Amfora and Kurtovska kapia have dark green fruits, whereas the colour of Una fruits is yellow-green at technological maturity. Measured morphometric characteristics of fruits are given in Table I.

TABLE I. Morphometric characteristics of genotypes; values preceded by the same letter in the vertical do not differ significantly according to the test of Fisher LSD ($p < 0.05$)

Genotype	Pericarp thickness, mm	Fruit length, cm	Fruit width, cm	Fruit weight, g
Amfora	4.98 ^a	13.30 ^b	6.38 ^a	117.33 ^a
Una	5.09 ^a	14.69 ^a	4.90 ^b	91.74 ^b
Kurtovska kapia	4.14 ^b	12.91 ^b	4.82 ^b	63.73 ^c

Significant differences were observed among genotypes in morphometric characteristics. According to ANOVA Amfora and Una have higher values of pericarp thickness, compared to Kurtovska kapia.

The measured values of lesions and mycelium developed on pepper fruits as a consequence of fungal infection are presented in Table II. Lesions formed on the surface of the Una genotype had the largest size. Compared with the other two tested genotypes, Amfora had ten times smaller external and internal lesions. According to the Mann-Whitney U test, the difference between lesion sizes of Una and Kurtovska kapia was not significant. On the other side, the mycelium size of all tested genotypes did not show a significant difference by KW test. This probably means that mycelium stopped growing, but fungal compounds still spread within the plant tissue. On intact fruits and sterile water injected fruits no lesions development was observed.

TABLE II. The rate of *A. alternata* infection on pepper fruits, values preceded of same letter in the vertical do not differ significantly according to the tests of Kruskal-Wallis and Mann-Whitney U ($p < 0.05$)

Genotype	Lesion				Mycelium			
	Diameter, mm		Area, mm ²		Diameter, mm		Area, mm ²	
	External	Internal	External	Internal	External	Internal	External	Internal
Amfora	1.43 ^a	2.39 ^a	6.22 ^a	10.89 ^a	1.38 ^a	13.44 ^a	1.76 ^a	6.11 ^a
Una	10.27 ^b	11.20 ^b	111.44 ^b	129.33 ^b	0.77 ^a	4.11 ^a	3.32 ^a	19.22 ^a
Kurtovska kapia	5.47 ^b	6.94 ^b	27.67 ^b	43.22 ^b	0.62 ^a	1.86 ^a	1.33 ^a	7.22 ^a

Differences in lesions diameter between tested genotypes suggested that there are probably differences in the biochemical response. Focusing on the biochemistry of the plant defence system, it had been reported that the host-pathogen interaction leads to changes in primary and secondary plant metabolites, as well as the enzyme profile as a result of excessive ROS production during host colonization.²¹

In the present study, ANOVA indicated that genotype, treatment, and their interaction had a significant influence (at 5 % level) on measured bioactive compounds and antioxidant capacity in fruits (F values are given in the Supplementary material to this paper; Table S-I). Results for measured biochemical parameters were presented in Figs. 1–5.

Obtained results demonstrated an increase in TP content in Amfora and Una in case of fungus infection (Fig. 1). This may indicate that these genotypes biosynthesize phenolic compounds as a part of the defence system against *Alternaria* infection. In the previous studies it was affirmed that the pathogen inoculation and mechanical damages provoke the accumulation of phenols.^{22,23} The production of phytoalexins, one of the phenolic compounds toxic to many pathogens, is a systemic early response to presence of fungus and bacteria.²⁴ On the other hand, the non-existence of difference in TP content in Kurtovska kapia genotypes can suggest that this antioxidant response is genotype dependent, which is in agreement with Ribes-Moya *et al.*²⁵ Antioxidant capacity measured by DPPH, NBT and TRC showed variability depending on genotype and treatment (Fig. 1).

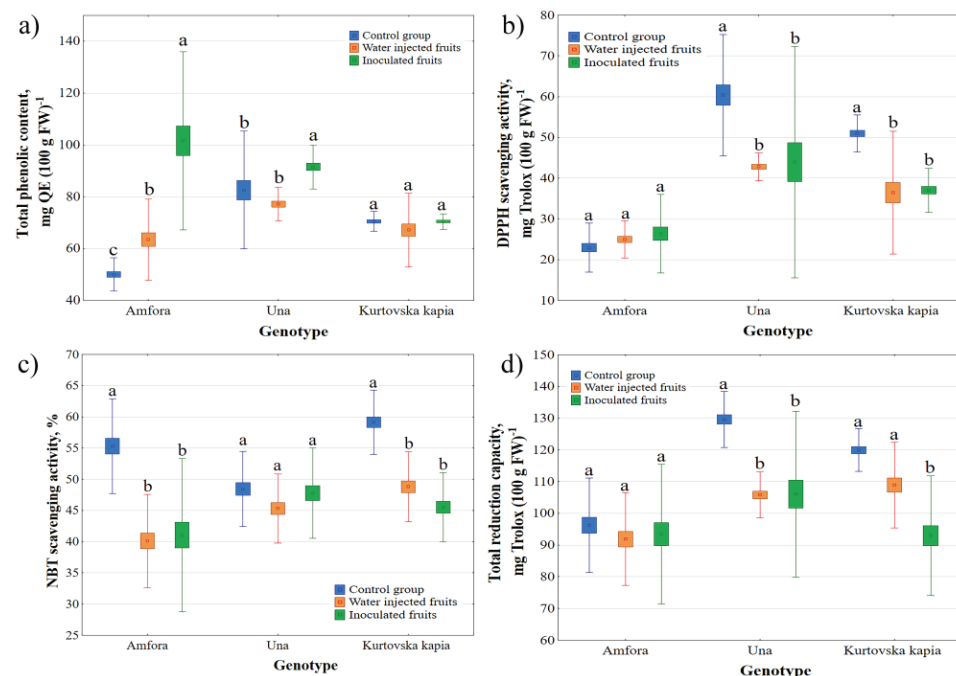


Fig. 1. Changes in a) Total phenolic content (TP) and antioxidant capacity measured by:
b) DPPH; c) NBT; d) total reduction capacity (TRC).

Based on DPPH and TRC test results, in the Amfora significant changes among experimental groups were not observed. Contrary, NBT test showed decrease in antioxidant activity when treatments were applied. The opposite trend in antioxidant activity was noticed in treated fruits of Una. In Kurtovska kapia, all antioxidant tests showed decrease in antioxidant activity in infected fruits. Rubio-Melgarejo *et al.*²⁴ suggested that pathogen may manipulate the defense res-

ponse, modifying the signalling network and cause decrease in the antioxidant activity. Variations in the results of antioxidant activity may be related to the different reaction mechanisms of applied tests and the nature of the antioxidant compounds present in the sample.²⁶

Vitamin C or ascorbic acid (AA) is one of the substances with the potential scavenging activity on pathogen-induced excessive ROS molecules. Variation in vitamin C content is related to genotype, maturity stage and agro-climatic conditions Żurawik *et al.*²⁷ The present work confirmed variations in amount of vitamin C content related to genotypes and treatment (Fig. 2). In the present study, the reduction in vitamin C level in inoculated pepper fruits of Kurtovska kapia is in accordance with findings of Tripathi and Mishra.²⁸ This fact may be associated with the oxidation of vitamin C by some degenerating oxidases produced during pathogenesis²⁹ or because of increasing rate of respiratory activity in infected tissue.³⁰ On the other hand, in Amfora and Una, vitamin C content was significantly increased by a fungal infection. Fujiwara *et al.*³¹ also described that total AA accumulates after viral infection as well as wounding stress.

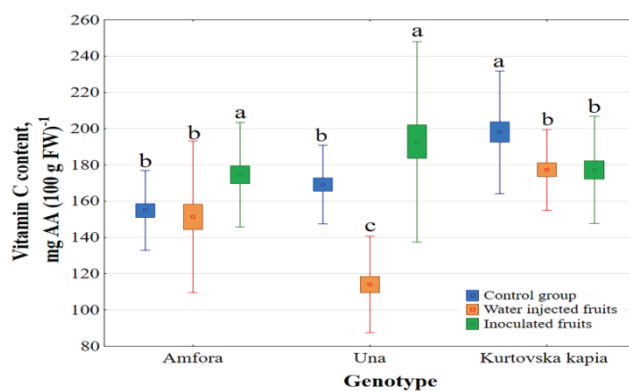


Fig. 2. Changes in vitamin C content assayed in three different genotype pepper fruits in control, water injected and inoculated groups.

ANOVA results obtained for enzymatic activity indicated that it is affected by genotype, type of treatment and the interaction of these factors. The influence of genotype, group of fruits treatment and their interaction significantly affected measured enzymatic activity at the level of 5 % (Supplementary material; Table S-II). The results of the tested enzymes are presented in Fig. 3.

CAT, SOD and peroxidases are the ROS-detoxifying enzymes which convert superoxide radicals and hydrogen peroxide into less toxic and more stable components. As a first line defence, SOD catalyses the dismutation of superoxide anion into oxygen and hydrogen peroxide, which is further catalysed by peroxidases and CAT. Peroxidases are members of a large family of enzymes, involved

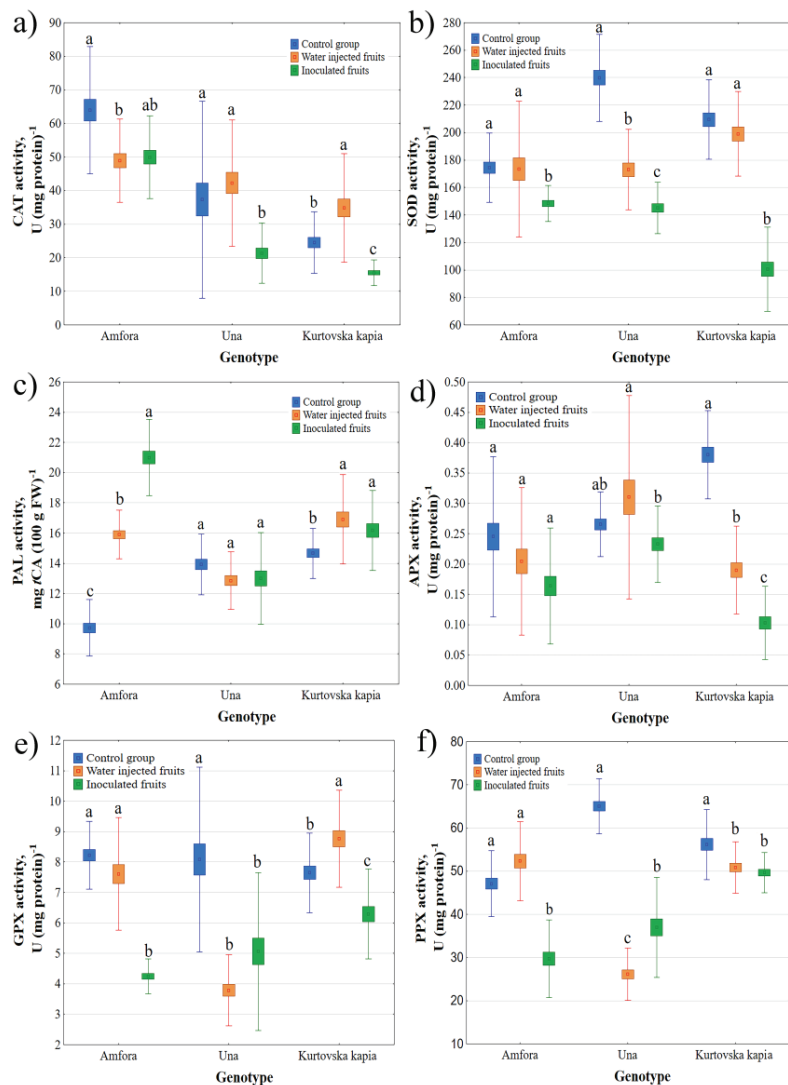


Fig. 3. Changes in: a) CAT; b) SOD; c) PAL; d) APX; e) GPX; f) PPX activity assayed in three different genotype pepper fruits in control, water injected and inoculated groups.

in hydrogen peroxide removal. The main difference between them is the type of a reducing substrate they use: ascorbate peroxidase uses ascorbate, guaiacol peroxidase guaiacol and pirogallol peroxidase pyrogallol.³² Increases in CAT, SOD and peroxidase activity indicates that initial infection induced their activities and consequently the activation of antioxidant plant defense.³³ The activity of CAT was lower in inoculated fruits of Una and Kurtovska kapia than in control fruits. This is consistent with the results of Li *et al.*³⁴ who found decrease in CAT act-

ivity in mango fruits infected by *A. alternata*. However, water-injected fruits of Kurtovska kapia showed the highest CAT activity. In Amfora, CAT activity was significantly reduced in fruits injected with water, compared to the control group. Wounding stress in avocado fruit lead to decrease in CAT and SOD levels.³⁵ Obtained results showed that in Una water-injected fruits had significantly lower SOD activity than the control group, but higher than infected fruits. In Amfora and Kurtovska kapia significant differences were not observed when fruits were just wounded and water-injected, SOD activity in all tested genotypes was reduced by *A. alternata* infection. Wang *et al.*³⁶ reported decrease in CAT, SOD and APX in the citrus fruit infected by *Penicillium digitatum*. In contrast, *Alternaria tenuis* and *Botrytis cinerea* in peach fruits increased the activities of CAT, SOD and peroxidase in comparison to the sterile water treatments.³⁷

GPX and PPX activity in pepper fruits was the lowest in inoculated fruits in Kurtovska kapia and Amfora, while in Una they were reduced compared to the control, being the lowest in water injected fruits. By the contrast, APX enzymatic activity was reduced only in Kurtovska kapia inoculated fruits. Borković *et al.*³⁸ also reported decrease in GPX and PPX in some genotypes of sweet cherry fruits infected by *Monilia laxa*. PAL catalyses the deamination of phenylalanine to form trans-cinnamic acid in the phenylpropanoid pathway. Cinamic acid has role in biosynthesis of hydroxycinnamic acid derivatives like coumaric, caffeic, ferulic acid as well as flavonoids, lignins, stilbenes, tannins and anthocyanins.³⁹ In Amfora and Kurtovska kapia significant increase in PAL activity was observed both in water-injected as well as *A. alternata* inoculated fruits. Additionally, in Amfora increase in PAL activity in inoculated and wounded fruits may be related to the production of phenolic compounds as defense responses in fruits.

The level of lipid peroxidation as an indicator of ROS-induced damage under stress conditions is based on the reaction of malondialdehyde (MDA), an end-product of lipid peroxidation, with thiobarbituric acid (TBA).⁴⁰ Accumulation of ROS is known to increase lipid peroxidation in biological membranes due to its ability to react with the double bond of lipid hydrocarbon chains. The 1,4-pentadiene structure of a polyunsaturated fatty acid (PUFA), either free or esterified to cholesterol or glycerol, is easily oxidized by unbalanced ROS.⁴¹ The level of lipid peroxidation was higher in fruits injected with water than in the control group, but the highest level of lipid peroxidation was found in the inoculated fruits (Fig. 4). Obtained results are in agreement with those of Li *et al.*³⁴ who reported an increase in MDA concentration in mango fruits infected by *A. alternata*.

To observe the relationship among examined bioactive compounds, enzyme activity, genotypes and wounding and infection stress, principal component analysis (PCA), Fig. 5, was applied. The PCA score plot (Fig. 5a) was used for studying the classification of the categorized data, while the PCA loadings plot was

used for obtaining information on the relative importance of the variables to each principal component (Fig. 5b).

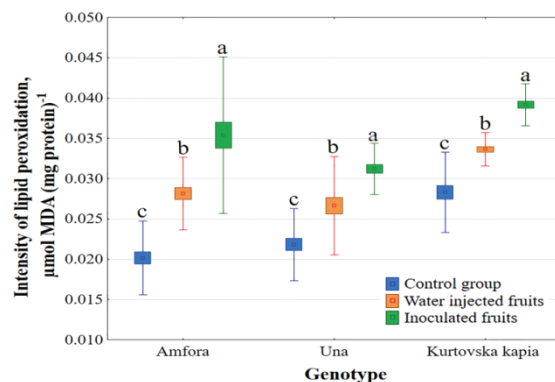


Fig. 4. Intensity of lipid peroxidation in healthy, wounded and sterile water injected as well as infected fruits in all three genotypes.

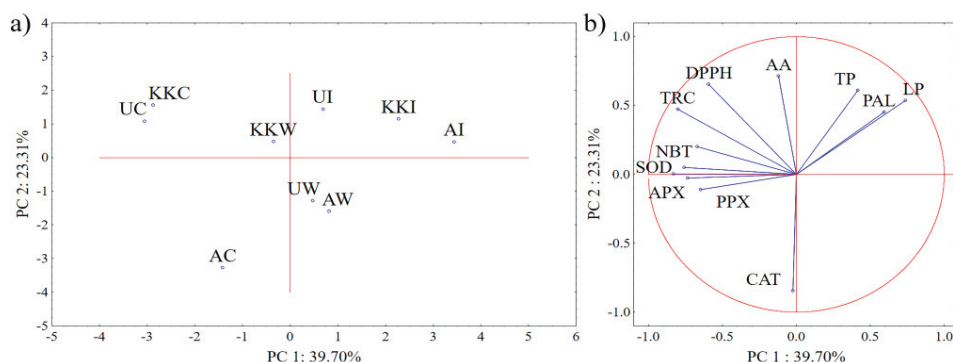


Fig. 5. Biplot of the first two principal components of principal component analysis; a) score plot of genotypes and treatment, Amfora control, water-injected, inoculated (AC, AW, AI), Una control, water-injected, inoculated (UC, UW, UI), Kurtovska kapia control, water-injected, inoculated (KKC, KKW, KKI); b) loadings plot of all evaluated biochemical parameters; total polyphenol content (TP); total ascorbic acid (AA); 2,2-dyphenyl-1-picrylhydrazyl assay (DPPH test); total reduction capacity (TRC); nitroblue tetrazolium test (NBT test); superoxide dismutase activity (SOD); intensity of lipid peroxidation (LP); phenylalanine ammonia-lyase activity (PAL); catalase activity (CAT); ascorbate peroxidase activity (APX); guaiacol peroxidase activity (GPX); pyrogallol peroxidase activity (PPX).

The first two principal components extracted by PCA covered 63.01 % of the data variance. The first component (PC1) accounted for 39.70 % of the total variance and it is highly likely that this dimension separate samples according to treatment, since PC1 separate infected and water-injected fruits (mostly positive scores) from control fruits (negative scores). According to PCA loading plot (Fig.

5b), PC1 was positively correlated with TP, PAL and intensity of lipid peroxidation (LP), while others biochemical assays had shown negative correlation. LP had the most important positive correlation whereas TRC, NBT, SOD and APX had shown the strongest negative correlation with PC1. The second principal component (PC2) accounted for 23.31 % of the total variance. It is likely that this component reflects the effect of genotype on the analysed parameters, considering that it separated Una and Kurtovska kapia (mostly positive scores) from Amfora fruits (mostly negative scores). PC2 showed a positive correlation with most of the assayed parameters, except for CAT, GPX, APX. As could be seen in Fig. 5b, ascorbic acid had the highest positive, while CAT had the highest negative influence on PC2.

CONCLUSION

Considering that the intensity of lipid peroxidation, as biological marker of oxidative stress, was increased in the wounded and sterile water-injected fruits as well as in infected fruits with *A. alternata*, it can be concluded that these factors disturb redox balance in peppers fruits in all examined genotypes. The pericarp thickness had the lowest value for Kurtovska kapia and was statistically different from Amfora and Una. Although the largest lesion developed on the surface of Una, its size was not significantly different from the lesion on Kurtovska kapia. Therefore, this may indicate that the pericarp thickness is not related to the defence network of pepper fruits as structural barrier. In present work, certain differences among genotypes exposed to wounding and pathogen stress were observed. In inoculated Amfora and Una fruits, TP and AA increase compare to control fruits. Given that, it can be concluded that mentioned phytochemicals have a contribution to the defence mechanism of Amfora and Una fruits against pathogen. In Kurtovska kapia level of vitamin C decreased after inoculation, while TP content was not changed either by wounding or inoculation. Except for PAL activity in Amfora and Kurtovska kapia and APX activity in wounded Kurtovska kapia fruits, all measured enzyme activity showed no changes or decrease by wounding and/or pathogen infection.

SUPPLEMENTARY MATERIAL

Additional data and information are available electronically at the pages of journal website: <https://www.shd-pub.org.rs/index.php/JSCS/article/view/12128>, or from the corresponding author on request.

Acknowledgement. This research was supported by the Ministry of Education, Science and Technological Development of the Republic of Serbia, grant numbers: 451-03-9/2022-14/200032 and 451-03-9/2022-14/200197.

ИЗВОД

АНТИОКСИДАТИВНИ ОДГОВОР ПЛОДОВА СЛАТКЕ ПАПРИКЕ НА ИНФЕКЦИЈУ
ГЉИВОМ *Alternaria alternata*

МАРИЈАНА ПЕИЋ ТУКУЉАЦ¹, ДАРИО ДАНОЈЕВИЋ², СЛАЂАНА МЕДИЋ-ПАП², ЈЕЛИЦА
ГВОЗДАНОВИЋ-ВАРГА² ИДЕЈАН ПРВУЛОВИЋ¹

¹Универзитет у Новом Саду, Пољо-и привредни факултет, Трг Д. Обрадовића 8, Нови Сад и ²Институт
за рашарство и повртарство, М. Горкој 30, Нови Сад

Паприка (*Capsicum annuum*) је важан извор многих биоактивних једињења, са заштитном улогом у биљкама од биотичког и абиотског стреса, и има благотворно дејство на здравље људи. Ово поврће је подложно многим инфекцијама, укључујући трулеж плодова након бербе проузроковано гљивом *Alternaria alternata*. У циљу бољег разумевања одбрамбеног система плодова, у раду је мерена концентрација фенола и аскорбинске киселине, антиоксидативна ензимска и неензимска активност у плодовима слатке паприке типа капија (сорте: Амфора, Уна и Куртовска капија) заражене гљивом *A. alternata*. Плодови Амфоре су имали највећу толерантност према инфекцији. Садржај укупних фенола и витамина С повећао се у плодовима Амфоре и Уне након механичког оштећења и инокулације, док су плодови Куртовске капије у та два случаја смањили количину витамина С. У зависности од механизма реакције антиоксидативни тестови нису показали промене ни смањење антиоксидативног капацитета третираних плодова. Осим активности фенилаланин-амонијум лиаза у Амфори и Куртовској капији и активности аскорбат-пероксидазе у механички повређеним плодовима Куртовске капије, све мерење активности ензима нису показале промене услед рањавања и/или инфекције гљивом *A. alternata*. Према резултатима интензитета липидне пероксидације као биолошког маркера оксидативног стреса, може се закључити да механичке повреде и инфекција нарушују редокс равнотежу код свих испитиваних генотипова. Утврђено је да испитивани генотипови показују извесну разлику у антиоксидативној одбрани од механичког оштећења и патогена.

(Примљено 15. новембра, ревидирано 23. децембра, прихваћено 24. децембра 2022)

REFERENCES

1. C. Gebhardt, *Theor. Appl. Genet.* **129** (2016) 2281 (<http://doi.org/10.1007/s00122-016-2804-1>)
2. A. K. Blanco-Ríos, L. Á. Medina-Juárez, G. A. González-Aguilar, N. Gámez-Meza, J. Mex. Chem. Soc. **57** (2013) 137 (<https://doi.org/10.29356/jmcs.v57i2.226>)
3. Jamiołkowska, *Phytopathologia* **62** (2012) 5 (http://web.archive.org/web/20180424103457id_/http://www.up.poznan.pl/~ptfit1/pdf/P62/P62_01.pdf)
4. V. Singh, A. Shrivastava, S. Jadon, N. Wahi, A. Singh, N. Sharma, *Int. J. Agric. Sci.* **7** (2015) 834 (http://bioinfopublication.org/files/articles/7_13_6_IJAS.pdf)
5. F. Collin, *Int. J. Mol. Sci.* **20** (2019) 2407 (<http://doi.org/10.3390/ijms20102407>)
6. S. Sachdev, S. A. Ansari, M. I. Ansari, M. Fujita, M. Hasanuzzaman, *Antioxidants (Basel)* **11** (2021) 277 (<http://doi.org/10.3390/antiox10020277>)
7. V. D. Rajput, Harish, R. K. Singh, K. K. Verma, L. Sharma, F. R. Quiroz-Figueroa, M. Meena, V. S. Gour, T. Minkina, S. Sushkova, S. Mandzhieva, *Biology* **10** (2021) 267 (<http://doi.org/10.3390/biology10040267>)
8. E. Fallik, S. Grinberg, S. Alkalai, S. Lurie, *Plant Pathol.* **45** (1996) 644 (<http://doi.org/10.1046/j.1365-3059.1996.d01-175.x>)

9. M. Frans, R. Aerts, S. Laethem, B. Van Calenbergen, L. Van Herck, K. Heungens, K. Van Poucke, S. Van Gool, J. Ceusters, in *Proceedings of XVI Eucarpia Capsicum and Eggplant Meeting*, 2016, Kecskemet, Hungary, Diamond Congress Ltd, Budapest, p 420 (<http://doi.org/10.5281/zenodo.1255303>)
10. P. C. Wootton-Beard, A. G. Moran, L. Ryan, *Food Res. Int.* **44** (2011) 217 (<http://doi.org/10.1016/j.foodres.2010.10.033>)
11. M. M. Rahman Khan, M. M. Rahman, M. S. Islam, S. A. Begum, *J. Biol. Sci.* **6** (2006) 388 (<http://doi.org/10.3923/jbs.2006.388.392>)
12. A. Floegel, D.-O. Kim, S.-J. Chung, S. I. Koo, O. K. Chun, *J. Food Compos. Anal.* **24** (2011) 1043 (<http://doi.org/10.1016/j.jfca.2011.01.008>)
13. P. Govindan, S. Muthukrishnan, *J. Acute. Med.* **3** (2013) 103 (<http://doi.org/10.1016/j.jacme.2013.06.003>)
14. A. Kumaran, R. J. Karunakaran, *Pharm. Bio.* **44** (2006) 146 (<https://doi.org/10.1080/13880200600596302>)
15. M. Bradford, *Anal. Biochem.* **72** (1976) 248 ([https://doi.org/10.1016/0003-2697\(76\)90527-3](https://doi.org/10.1016/0003-2697(76)90527-3))
16. H. Aebi, *Meth. Enzymol.* **105** (1984) 121 ([http://doi.org/10.1016/s0076-6879\(84\)05016-3](http://doi.org/10.1016/s0076-6879(84)05016-3))
17. Y. Nakano, K. Asada, *Plant Cell Physiol.* **28** (1987) 131 (<https://doi.org/10.1093/oxfordjournals.pcp.a077268>)
18. Morkunas, J. Gmerek, *J. Plant Physiol.* **164** (2007) 185 (<http://doi.org/10.1016/j.jplph.2005.11.005>)
19. N. G. Gerasimova, S. M. Pridvorova, O. L. Ozeretskovskaya, *Appl. Biochem. Microbiol.* **41** (2005) 103 (<https://doi.org/10.1093/oxfordjournals.pcp.a077268>)
20. R. L. Heath, L. Packer, *Arch. Biochem. Biophys.* **125** (1968) 189 ([http://doi.org/10.1016/0003-9861\(68\)90654-1](http://doi.org/10.1016/0003-9861(68)90654-1))
21. A. Zarrillo, M. Minutolo, D. Alioto, A. Errico, *Sci. Hortic.* **225** (2017) 512 (<https://doi.org/10.1016/j.scientia.2017.07.043>)
22. S. M Arias, G. E. G. Alvarez, *Arch Phytopathol. Plant Prot.* **54** (2021) 152 (<https://doi.org/10.1080/03235408.2020.1824339>)
23. M. Wallis, E. R. Galarneau, *Front. Plant Sci.* **11** (2020) 580753 (<http://doi.org/10.3389/fpls.2020.580753>)
24. A. Rubio-Melgarejo, R. Balois-Morales, V. A. Ochoa-Jiménez, P. P. Casas-Junco, J. O. Jiménez-Zurita, P. U. Bautista-Rosales, G. Berumen-Varela, *Plants* **10** (2021) 1432 (<http://doi:10.3390/plants10071432>)
25. M. Ribes-Moya, A. M. Adalid-Martínez, M. B. Gil, P. Esteve-Ciudad, P. Fernández-DeCórdoba, M. D. Raigón, A. Rodriguez-Burrueto, *Bull. Univ. Agric. Sci. Vet. Med. Cluj-Napoca, Food Sci. Technol.* **75** (2018) 68 (<https://pdfs.semanticscholar.org/5bff/0dff68cb33458714d508469fc3cc7f10c7640.pdf>)
26. M. Becker, G. Nunes, D. Ribeiro, F. Silva, G. Catanante, J. Marty, *J. Braz. Chem. Soc.* **30** (2019) 1108 (<http://dx.doi.org/10.21577/0103-5053.20190003>)
27. A. Żurawik, D. Jadczak, N. Panayotov, P. Żurawik, *Plant Soil Environ.* **67** (2021) 653 (<https://doi.org/10.17221/333/2021-PSE>)
28. S. Tripathi, H. N. Mishra, *Braz. J. Microbiol.* **40** (2009) 139 (<https://doi.org/10.1590/S1517-83822009000100024>)
29. V. A. Adisa, *Food Chem.* **22** (1986) 139 ([https://doi.org/10.1016/0308-8146\(86\)90031-2](https://doi.org/10.1016/0308-8146(86)90031-2))
30. O. A. Oke, K. M. Banjoko, *Mycopathologia* **116** (1991) 199 (<http://doi.org/10.1007/bf00436835>)

31. A. Fujiwara, S. Togawa, T. Hikawa, H. Matsuura, C. Masuta, T. Inukai, *J. Exp. Bot.* **67** (2016) 4391 (<https://doi.org/10.1093/jxb/erw223>)
32. M. Mourato, R. Reis, L. L. Martins, in *Advances in Selected Plant Phisiology Aspects*, G. Montanaro, B. Dicio, Eds., IntechOpen, London, 2012 (<https://doi.org/10.5772/34557>)
33. M. Ramzan, S. Sana, N. Javaid, A. A. Shah, S. Ejaz, W. N. Malik, N. A. Yasin, S. Alamri, M. H. Siddiqui, R. Dutta, S. Fahad, N. Tahir, S. Mubeen, M. A. Ali, A. El Sabagh, S. Danish, *Sci. Rep.* **11** (2021) 9445 (<https://doi.org/10.1038/s41598-021-88797-1>)
34. J. Li, L. Mao, Y. Zhang, L. Zhang, H. Jiang, *Czech J. Food Sci.* **36** (2018) 227 (<https://doi.org/10.17221/328/2017-CJFS>)
35. E. Castro-Mercado, Y. Martinez-Diaz, N. Roman-Tehandon, E. Garcia-Pineda, *Protoplasma* **235** (2009) 67 (<http://dx.doi.org/10.1007/s00709-009-0034-y>)
36. Y. Wang, D. Ji, T. Chen, B. Li, Z. Zhang, G. Qin, S. Tian, *Int. J. Mol. Sci.* **20** (2019) 2994 (<https://doi.org/10.3390/ijms20122994>)
37. S. Zhang, Q. Zheng, B. Xu, J. Liu, *Toxins* **11** (2019) 322 (<https://doi.org/10.3390/toxins11060322>)
38. Borković, Đ. Malenčić, D. Prvulović, J. Šućur, M. Grahovac, B. Kiprovska, A. Manojlović, *Ann. Agron.* **41** (2017) 21 (<http://polj.uns.ac.rs/sites/default/files/letopis-naucnih-radova/3%20Borkovi%C4%87%20et%20al.%20OR%20Ann%20Agron.%2041%282%29%20ENG.pdf>)
39. S. B. França, P. R. dos S. Correia, I. B. D. de Castro, E. F. da Silva Júnior, M. E. de S. B Barros, D. J. da P. Lima, *Res., Soc. Dev.* **10** (2021) e28010111691 (<https://doi.org/10.33448/rsd-v10i1.11691>)
40. D. Alché, *Redox Biol.* **23** (2019) 101136 (<https://doi.org/10.1016/j.redox.2019.101136>)
41. A. Sofo, A. Scopa, A. Hashem, E. F. Abd-Allah, in *Plant-Environment Interaction: Responses and Approaches to Mitigate Stress*, M. M. Azooz, P. Ahmad, Eds., Wiley, Hoboken, NJ, 2015, p.205 (ISBN: 978-1-119-08099-2).



SUPPLEMENTARY MATERIAL TO
**Antioxidant response of sweet pepper fruits infected with
*Alternaria alternata***

MARIJANA PEIĆ TUKULJAC^{1*}, DARIO DANOJEVIĆ², SLAĐANA MEDIĆ-PAP²,
JELICA GVOZDANOVIC-VARGA² and DEJAN PRVULOVIĆ¹

¹University of Novi Sad, Faculty of Agriculture, Trg D.Obradovića 8, 21000 Novi Sad, Serbia
and ²Institute of Field and Vegetable Crops Novi Sad, M. Gorkog 30, 21000 Novi Sad, Serbia

J. Serb. Chem. Soc. 88 (3) (2023) 237–250

TABLE S-I. *F* values for total phenolic content (TP), DPPH – radical cation scavenging activity; NBT test – nitroblue tetrazolium test; TRC – total reduction capacity and vitamin C content in pepper fruits; *d.f.* – degree of freedom, * – significant at 5% level; *n* = 9;

Parameter	<i>d.f.</i>	<i>F</i> value				
		TP	DPPH	NBT test	TRC	Vitamin C
Genotype (G)	2	24.96*	102.28*	17.37*	43.52*	20.25*
Treatment (T)	2	52.54*	20.11*	62.13*	35.50*	31.59*
G × T	4	27.56*	8.40*	11.93*	8.50*	16.14*

TABLE S-II. *F* values of enzyme activity: CAT – catalase; PAL – phenylalanine ammonia lyase; APX – ascorbate peroxidase; GPX – guaiacol peroxidase; PPX – pyrogallol peroxidase; SOD – superoxide dismutase, and intensity of lipid peroxidation; *d.f.* – degree of freedom, * - significant at 5% level; *n* = 9;

Parameter	<i>d.f.</i>	<i>F</i> value						Intensity of lipid peroxidation
		CAT	PAL	APX	GPX	PPX	SOD	
Genotype (G)	2	95.02*	41.97*	11.94*	31.39*	51.03*	14.01*	58.64*
Treatment (T)	2	23.73*	80.90*	45.74*	65.83*	142.12*	179.85*	142.30*
G × T	4	7.94*	73.15*	18.80*	29.09*	90.66*	32.81*	3.11*

*Corresponding author. E-mail: marijana.peic@polj.uns.ac.rs



Deeper inside, the use of chitooligosaccharides, in wound healing process. A computational approach

MARIANA A. MATICA¹, DIANA L. ROMAN^{2,3}, VASILE OSTAFE^{2,3}
and ADRIANA ISVORAN^{2,3*}

¹Department of Chemistry-Biology, Institute for Advanced Environmental Research, West University of Timisoara, Oituz 4C, 300086 Timisoara, Romania, ²Department of Biology-Chemistry, Faculty of Chemistry, Biology, Geography, West University of Timisoara, 16 Pestalozzi, 300115 Timisoara, Romania and ³Advanced Environmental Research Laboratories (AERL), West University of Timisoara, Oituz 4A, 300086 Timisoara, Romania

(Received 2 July, revised 13 November, accepted 20 November 2022)

Abstract: Chitooligosaccharides (COs) containing up to 10 monomeric units of N-acetyl D-glucosamine and/or D-glucosamine are water-soluble molecules revealing numerous biological activities and low toxicological profiles. Within this study, a computational approach has been used to predict the involvement of the COs having distinct chemical properties (molecular weight, deacetylation degree and acetylation pattern) in all the four wound healing phases: hemostasis, inflammation, proliferation and tissue remodeling. There are predictions, for the investigated COs, regarding their molecular targets and the biological activities that are reliant to the wound healing process. Furthermore, a molecular docking approach was used to assess the interactions of the investigated COs with the myeloid differentiation factor 2 (MD-2), a protein involved in the inflammatory processes. The investigation confirms the functional roles of the investigated COs in wound healing. The molecular targets predicted for the COs containing totally and partially acetylated units are galectins and selectins and those predicted for COs containing totally deacetylated units are fibroblast growing factors, the COs containing 3 units revealing the higher number of molecular targets. All these proteins are involved in mediating immune response, inducing cell division, growth and cell adhesion during the process of wound healing. All the COs containing from 2 to 8 monomeric units are able to interact with the MD-2 protein, the interactions being stronger for the COs containing 6 and 8 monomeric units. The interaction energies increase with the increasing molecular weight and with decreasing deacetylation degree and are reliant on acetylation patterns. Among the investigated COs, the totally acetylated COs containing 6 and 8 N-acetyl glucosamine units can be

* Corresponding author. E-mail: adriana.isvoran@e-uvt.ro
<https://doi.org/10.2298/JSC220702081M>

better inhibitors of the LPS binding to MD-2 protein. Consequently, mixtures of COs with distinct properties should be considered suitable candidates as adjuvants in developing scaffolds for the wound healing process.

Keywords: immune response; myeloid differentiation factor 2 (MD-2); inflammatory process; cell adhesion; molecular docking.

INTRODUCTION

Chitin, the second most abundant biopolymer on Earth, consists of *N*-acetyl-D-glucosamine units. Chitin is difficult to use due to its poor solubility in most organic solvents and water. Its partial deacetylated form, the chitosan, is soluble in acidic environment, which makes it more easy to process and use.¹ Chitosan consists of D-glucosamine and *N*-acetyl-D-glucosamine, with at least a 60 % deacetylation degree (percent of deacetylated units in the polymer).¹ Both chitin and chitosan are biodegradable, biocompatible and non-toxic² polymers of a great medicinal and economical interest. Chitooligosaccharide is the term used in specific literature to describe chitosan oligosaccharides with a polymerization degree below 20 and an average molecular weight of up to 3.9 kDa.³ Chitooligosaccharides (COs) are obtained by chitosan enzymatic or chemical degradation and are composed by oligomers of D-glucosamine (GlcN or D) and *N*-acetyl-glucosamine (GlcNAc or A).

COs with a maximum of 10 monomeric units are considered water-soluble molecules, with enhanced biological activities such as antimicrobial, anti-cancer, anti-inflammatory, stimulation of the immune system, blood pressure control and so on.⁴ The chemical characteristics of the COs, based on the molar fraction of D-glucosamine in the molecule (deacetylation degree, DaD) and the pattern of *N*-acetylation (PA), have a great impact on their biological activities.³ Furthermore, the position of the acetyl groups along the glycan chain strongly influences their biological activities.⁵ A computational study exposed that COs, regardless of their physicochemical properties, revealed promising pharmacological profiles and few toxicological effects on humans: the inhibition of the organic anion transporting peptides OATP1B1 and/or OATP1B3, low potential of cardiotoxicity, and the COs with high DaD exposed the potential of producing phospholipidosis.⁶ A molecular docking study revealed favorable interactions of COs with plasma proteins, the interaction energies increasing with the molecular weight (*MW*), decreasing with increasing DaD and being reliant on the PA.⁷ Furthermore, other studies emphasized that the COs characteristics conducted to distinct affinities for chitin deacetylases⁸ and lysozyme.⁹

The wound healing process depends on four wound healing phases: hemostasis, inflammation, proliferation and tissue remodeling. Scientific literature has shown that COs can be useful in all stages of wound healing having a hemostatic effect, being able to protect the wound from infections, to have anti-inflamm-

ory and immunostimulatory activities, to stimulate healing by enhancing the permeability of air and moisture, to support cell adhesion and promote cell proliferation. The chemical characteristics of COs influence their wound healing effects.¹⁰ COs used in the mentioned study are not well characterized in terms of their chemical properties, especially in terms of the acetylation pattern.

This study aims to predict the molecular targets and biological activities of the COs having various chemical properties, with a focus on their anti-inflammatory properties. One of the molecules responsible for triggering the inflammatory response is the lipopolysaccharide (LPS), present in the outer membrane of Gram-negative bacteria. If a wound gets infected by a Gram-negative pathogen, a very small amount of LPS is sufficient to initiate an immune response and the inflammatory process will begin.¹¹ Normally, the inflammatory process will help the human body to overcome the damage produced by the foreign pathogens, but when the inflammatory response is excessive, this can cause severe damage to tissues and organs. LPS are crucial for the pathogenesis of inflammation, and septic shock syndrome is often related to the uncontrolled inflammatory response to LPS.¹¹ Various LPS receptors and accessory proteins, like LPS binding protein (LBP), CD14 and the toll-like receptor 4 (TLR4) – myeloid differentiation factor 2 (MD-2) complex, are involved in helping the immune system to recognize LPS. It was revealed that LPS has an analogous affinity for MD-2 as for the TLR4-MD-2 complex indicating that MD-2 is the component assuring the LPS binding.¹² COs have been proven to inhibit the inflammatory process triggered by LPS.¹⁰ Literature data reveal that COs, usually containing between 2 and 8 monomeric units and characterized by a deacetylation degree of 95 % and uncharacterized acetylation pattern, inhibit the binding of LPS to the TLR4–MD-2 receptor complex reducing the production of pro-inflammatory mediators.¹³

Within this study, a computational approach is considered in order to enhance the knowledge regarding the influence of the chemical properties of COs on the wound healing process and to emphasize the best composition of COs to increase the wound healing effect. COs having various *MW* (but no more than 8 monomeric units), DaD and AP are considered, their molecular targets and biological activities related to the wound healing process are predicted, respectively their anti-inflammatory effect through interactions with MD-2 protein using a molecular docking approach is assessed.

EXPERIMENTAL

Within the present study, COs having between 2 and 8 monomeric units were considered as it was specified in the scientific literature that they are efficient for wound healing and especially for the anti-inflammatory effect.¹³ Since open wounds usually have a neutral to alkaline pH and chronic wounds exist at alkaline pH,¹⁴ COs with the amino groups that are not protonated have been considered. The simplified molecular-input line-entry system (SMILES) formulas of the COs under investigation (Table I) were built using ACD/ChemSketch soft-

ware (<https://chemicalize.com>). The COs 3D structures were obtained and minimized using Chimera software.¹⁵

TABLE I. Chitooligosaccharides considered in this study (A – unit of *N*-acetyl-glucosamine, D – unit of glucosamine, DaD – deacetylation degree)

DaD = 0	DaD = 33 %	DaD = 50 %	DaD = 67 %	DaD = 100 %
2A, 3A, 4A, 5A, 6A, 8A	ADA	DA, AADD, ADAD, ADDA, DAAD, DDAA, DADA, ADADAD, DADADA, DADADADA	DDA, DDDADA ADDDAD	2D, 3D, 4D, 5D, 6D, 8D

In order to predict the COs molecular targets, the Swiss Target Prediction Tool has been considered.¹⁶ It allows predictions of the macromolecular targets of bioactive small molecules and is based on the similarity principle, meaning that two similar bioactive molecules are probable to share their molecular targets. In this study we have considered human targets in the top 15 predictions being known that the level of predictive performance is usually higher than 70 % in this case. Only the molecular targets that can be involved in the wound healing process have been listed.

Prediction of activity spectra of substances (PASS) computational tool¹⁷ has been considered for predicting the biological activities of the investigated COs. It estimates the probability that the query molecule belongs to the particular class of active (*Pa*) or inactive (*Pi*) compounds based on the analysis of structure–activity relationships for more than 250,000 biologically active substances. The values of the two probabilities (*Pa* and *Pi*) vary from 0 to 1 and are independent. Only those activities with *Pa* > *Pi* are considered promising for a particular compound and a good accuracy of prediction is obtained when *Pa* > 0.7. The average accuracy of prediction estimated for the whole PASS training set is about 95 %.¹⁷ Only the biological activities related to the wound healing process have been listed in this article.

The molecular docking approach has been used for assessing the possible inhibitory effect of COs having various *MW*, DaD and AP against MD-2 protein. The crystallographic structure of the TLR4–MD-2 complex with the eritoran as a ligand bound to MD2 has been extracted from Protein Data Bank (PDB ID 2Z65). Eritoran is an analog of LPS antagonizing its activity by binding to the TLR4–MD-2 complex, this binding being mediated by the hydrophobic internal pocket in MD-2 and the opening region of the pocket containing positively charged residues,¹⁸ as visualized in Fig. 1 using Chimera software.¹⁵ Eritoran occupies almost all the volume of the binding pocket.

The MD-2 structure has been considered target molecule and was prepared for docking using Chimera software. Molecular docking has been implemented using the SwissDock facility¹⁹ that proposes binding modes for the ligand to the target and computes the energy of the interactions. A blind and accurate docking protocol has been considered. Chimera software has been used for the analysis of docking results. To evaluate the docking results and characterize the molecular interactions in the complexes between COs and MD-2 protein that were obtained by molecular docking, the PLIP (protein–ligand interaction profiler) software has been considered with default settings.²⁰ This software yields the list of detected interactions on a single atom level and enables analyses of specific binding characteristics. Seven interaction types can be detected by using this software: hydrophobic contacts, hydrogen bonds, salt bridges, water bridges, pi-stacking, pi-cation interactions and halogen bonds.

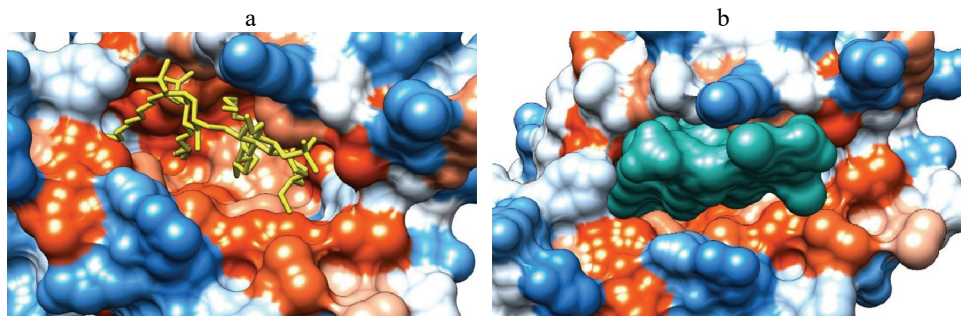


Fig. 1. Visualization of the hydrophobicity surface (blue regions are hydrophilic and orange regions are hydrophobic) of the MD-2 protein in complex with eritoran (PDB ID 2Z65) revealed as yellow sticks (a) and green surface (b).

RESULTS AND DISCUSSION

The molecular targets predicted for the investigated COs using Swiss Target Prediction Tool, and that relevant for wound healing, are revealed in Table II. The probability of every prediction is also presented. Preceding studies demonstrated that any value above 0 for the probability was considered to be reasonable.¹⁶ The molecular targets for COs containing more than 6 monomeric acetylated units were not predicted due to their high molecular weight.

Data presented in Table II reveal distinct molecular targets for the totally deacetylated COs by comparison to totally and partially acetylated COs. Moreover, there are distinct values for the probabilities of the predicted molecular targets for COs with various chemical properties. COs containing 3 monomeric units, regardless of their acetylated status, exhibit the higher values for the probabilities. Among the COs containing 3 monomeric units totally or partially acetylated, the totally acetylated COs reveal the wider spectra of the molecular targets.

In the case of totally and partially acetylated COs, galectins are the main group of proteins considered molecular targets. Galectins are β -galactoside-binding proteins that modulate re-epithelialization, an important stage in wound healing, *via* a carbohydrate-based recognition system.²¹ From the group of galectins, totally and partially deacetylated COs target galectin-3, galectin-4 and galectin-8. Galectin-3 is involved in the acute inflammatory response, triggering neutrophil activation and adhesion being also responsible for macrophage and monocytes chemotaxis. Galectin-4 is linked with gastro-intestinal tract wound healing, being expressed particularly in GI tissue, and it promotes both cell migration and cell proliferation. Galectin-8 mediates the cell adhesion process through interactions with integrins, other cell-surface proteins.²¹

Selectins, other targeted proteins by totally and partially acetylated COs, are adhesion molecules that regulate the leukocyte migration, from the circulatory system to inflammatory sites.²² It is well known that the lack of adhesion

molecules lead to; suppressed angiogenesis, keratinocyte migration, granulation tissue formation and inhibits early wound healing, also decrease the growth factor expression and inflammatory cell infiltration.²³

TABLE II. The predicted molecular targets that are involved in wound healing of the investigated chitooligosaccharides. Between parentheses are the probability value for every predicted target

COs	Predicted molecular targets and the probability of the predictions
Totally acetylated COs	
2A	Galectin-3 (0.297), galectin-4 (0.104), galectin-8 (0.104)
3A	Galectin-3 (0.219), galectin-4 (0.152), galectin-8 (0.152), myelin-associated glycoprotein (0.066), selectin E (0.066), adenosine A1 receptor (0.066), adenosine A2a receptor (0.066), adenosine A3 receptor (0.066), galectin-9 (0.066)
4A	Galectin-3 (0.020), adenosine A1 receptor (0.012)
5A	Galectin-4 (0.122), galectin-8 (0.122), galectin-3 (0.064), leukocyte adhesion molecule-1 (0.064), selectin E (0.064), P-selectin (0.064)
Partially acetylated COs	
DA	Galectin-4 (0.166), galectin-8 (0.166), galectin-3 (0.109), selectin E (0.109)
ADA	Galectin-4 (0.170), galectin-8 (0.170), galectin-3 (0.105)
DDA	Galectin-4 (0.208), galectin-8 (0.208), galectin-3 (0.175), myelin-associated glycoprotein (0.126), selectin E (0.126)
ADAD, DADA, AADD, DAAD, DDAA	Galectin-4 (0.118), galectin-3 (0.118), galectin-8 (0.118), leukocyte adhesion molecule-1 (0.050), selectin E (0.050), P-selectin (0.050)
ADDA	Galectin-4 (0.118), galectin-8 (0.118), galectin-3 (0.060), leukocyte adhesion molecule-1 (0.050), selectin E (0.050)
ADADAD, ADDDAD, DDDADA	Galectin-4 (0.122), galectin-3 (0.122), galectin-8 (0.122), myelin-associated glycoprotein (0.064), leukocyte adhesion molecule-1 (0.064), selectin E (0.064), P-selectin (0.064)
Totally deacetylated COs	
2D	Vanilloid receptor (0.127), acidic fibroblast growth factor (0.102), vascular endothelial growth factor A (0.102), heparanase (0.102), heat shock protein HSP 90-alpha (0.102)
3D	Vanilloid receptor (0.128), vascular endothelial growth factor A (0.120), basic fibroblast growth factor (0.120), heparanase (0.120), acidic fibroblast growth factor (0.120), heat shock protein HSP 90-alpha (0.120)
4D	Vanilloid receptor (0.084), vascular endothelial growth factor A (0.056), basic fibroblast growth factor (0.056), heparanase (0.056), acidic fibroblast growth factor (0.056), heat shock protein HSP 90-alpha (0.056)
5D	Vanilloid receptor (0.022), vascular endothelial growth factor A (0.022), basic fibroblast growth factor (0.022), heparanase (0.022), acidic fibroblast growth factor (0.022), heat shock protein HSP 90-alpha (0.022)
6D	Vanilloid receptor (0.083), vascular endothelial growth factor A (0.064), basic fibroblast growth factor (0.064), heparanase (0.064), acidic fibroblast growth factor (0.064), heat shock protein HSP 90-alpha (0.064)

Adenosine receptors, which are considered molecular targets of the COs containing 3 acetylated units, are linked to the accelerated wound healing process. They are initiators of the first stage of the wound healing process and can promote cell migration, cell proliferation, growth factor secretion and angiogenesis.²⁴ The leukocyte adhesion molecules play important roles in hemostasis, wound healing, morphogenesis, maintenance of tissue architecture.²⁵ The myelin-associated glycoproteins are involved in axon regeneration and cell adhesion.²⁶

Growth factors are the main group of targets for totally deacetylated COs. They are signaling molecules characterized by chemotactic activities that attract fibroblast and inflammatory cell to the wound site, also can stimulate angiogenesis and cell proliferation.²⁷

Heat shock protein-90 α (Hsp-90 α), another target of the totally deacetylated COs, is a possible enhancer of wound closure by promoting cell survival and cell motility.²⁸ Keratinocyte-secreted Hsp90 α is involved in wound closure,²⁹ its expression being induced by heat stress and wounding of the epidermis. Studies have shown the great potential of Hsp-90 α in treating different types of skin wounds and topical application of Hsp90 α improved the wound healing time.²⁸

Heparanase and vanilloid receptor are other molecules targeted by totally acetylated COs. Heparanase is responsible for mediating cell adhesion and migration³⁰ and the vanilloid receptor is linked to pain management involving different types of wounds.³¹ Similar molecular targets have been predicted for a totally deacetylated chitoooligosaccharide containing 9 units, chondroitin sulphate and agar.³²

Several of these predicted molecular targets have been already noticed in specific literature and it underlines the validity of the predictions. The interactions between oligosaccharides and various galectins have been revealed, the preferred ligands of galectins being *N*-acetyl lactosamine and related disaccharides.³³

Literature data also reveal that chitosan was able to interact with fibroblast growth factor-2 and consequently protect it from inactivation³⁴ and the inhibition of heparanase by COs has been already emphasized.³⁵ Experimental studies demonstrated that the COs having molecular weights of 800 Da and prepared by degradation of chitosan with a DaD of 92.3 % promoted peripheral nerve regeneration with functional recovery in rats having sciatic nerve crush injury.³⁶

Similar results were obtained in other studies, therefore COs accelerated peripheral nerve regeneration, improved the number of myelinated nerve fibers and increased the thickness of regenerated myelin sheaths in rabbits, promoted Schwann cell proliferation, enhanced the axonal myelination, increased the expression of cell adhesion proteins and increased cell survival in a dose-dependent manner.³⁷

The outcomes obtained using PASS software and regarding the wound healing of investigated COs are presented in Table III. Only the activities predicted

with a probability of being active (Pa) higher than 0.7 are shown, being known that a good accuracy of prediction is obtained when $Pa > 0.7$. Because of the molecular weight limit of the PASS software, there are no predictions for the COs containing 8 monomeric units.

TABLE III. Predicted wound healing activities of investigated COs using PASS software. Pa is the probability to be active and is shown between parentheses for every predicted activity

COs	Predicted wound healing activities
2A–6A	Hyaluronic acid agonist (0.894), angiogenesis stimulant (0.799), membrane integrity agonist (0.793), macrophage stimulant (0.781)
DA, ADA, DDA, AADD, DADA, ADAD, DAAD, DDA, ADDA, ADADAD, DADADA, ADDDAD, DDDADA	Macrophage stimulant (0.872), hyaluronic acid agonist (0.859), angiogenesis stimulant (0.772)
2D–6D	Macrophage stimulant (0.916), hyaluronic acid agonist (0.795), angiogenesis stimulant (0.781), membrane integrity agonist (0.719), transcription factor stimulant (0.711)

Prediction obtained using PASS shows that all investigated COs, regardless of their chemical properties, exhibit a variety of biological activities concerning the wound healing process. Aspects such as membrane integrity, hyaluronic acid agonists, angiogenesis, growth factor, and macrophage stimulants, are among those biological processes that are very important in wound healing. Membrane integrity is an essential condition for maintaining the cell viability and normal functions. Hyaluronic acid promotes wound healing and accelerates wound healing even in chronic wounds.³⁸ The totally deacetylated COs act as transcription factor stimulants as well. Transcription factor NF kappa B stimulant for example, mediates the wound healing through anti-inflammatory and anti-oxidant effects.³⁹

Among these predicted wound healing activities, macrophage and angiogenesis stimulant activity have been reported. An experimental *in vitro* study revealed that COs having distinct polymerization degrees could promote the proliferation of macrophages cells and stimulate angiogenesis, the best results being obtained for chitopentaose hydrochloride.⁴⁰ COs also revealed anti-angiogenic effects.³⁵

The outcomes of the molecular docking study reveal that investigated COs are able to bind to the active site of the MD-2 protein. These results are in strong correlation with experimental data revealing that COs significantly inhibited binding of LPS to TLR4/MD-2 complex.¹³ Fig. 2 present the best binding position of the 6A and respectively 6D chitooligosaccharides to MD-2 protein and the Fig. 3 illustrates the registered binding energies for the best binding poses of all investigated COs to MD-2 protein.

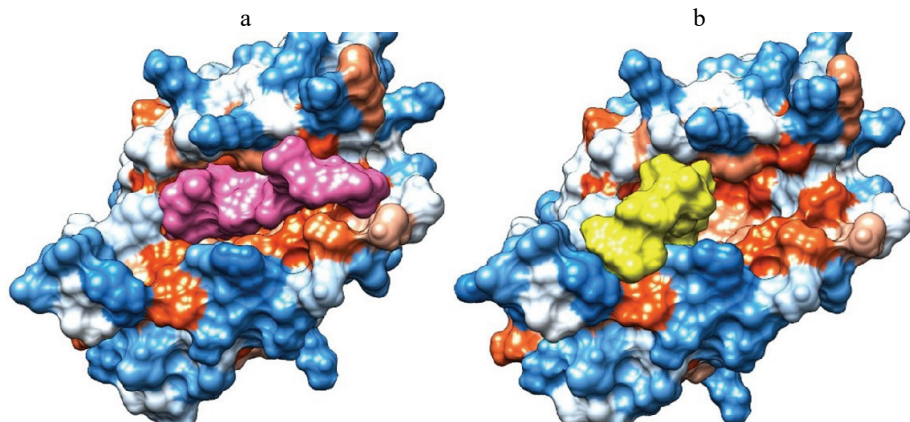


Fig 2. Visualization of the best docked binding poses to MD-2 protein of: a) the chito-oligosaccharide containing 6 acetylated units (6A) visualized as magenta surface; b) the chito-oligosaccharide containing 6 deacetylated units (6D) visualized as yellow surface. MD-2 protein is visualized as hydrophobicity surface, blue regions are hydrophilic and orange regions are hydrophobic.

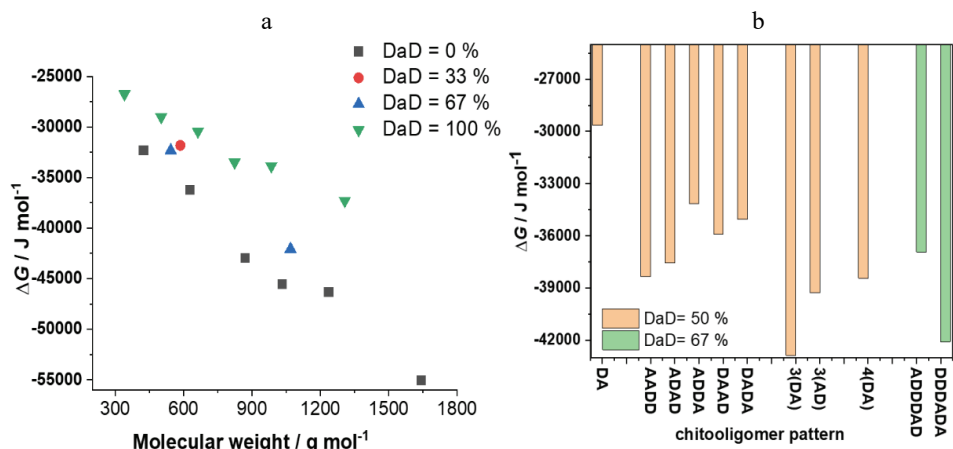


Fig 3. The interacting energies obtained for the best binding poses of COs to MD-2 protein taking into account: a) the molecular weight and deacetylation degrees (DaD) and b) the deacetylation degree and acetylation pattern.

Fig. 2 shows that both 6A and 6D COs bind to the active site of MD-2 protein, but 6A chito-oligosaccharide occupies almost the entire internal surface of the cavity and 6D chito-oligosaccharide occupies only a region of the cavity. This is consistent with the values of the Gibbs energy change revealing a stronger interaction between the 6A and MD-2; $\Delta G = -46339 \text{ J mol}^{-1}$, compared with $-35246.12 \text{ J mol}^{-1}$ for binding of 6D to MD-2.

Data presented in Fig 3a reveal that interacting energy between COs and MD-2 protein increases with the molecular weight, chitooligosaccharides containing 6 and 8 monomeric units exhibit stronger interactions. The interaction energies also increase with decreasing deacetylation degree, the totally acetylated chitooligosaccharides prove better inhibitors of the LPS binding to MD-2 protein. This result is in good agreement with the hydrophobic nature of the active site cavity of the MD-2 protein, as the acetylated COs have a higher hydrophobicity than deacetylated ones. Fig 3b emphasizes that, for the same DaD and *MW*, the acetylation pattern also influences the interactions of COs with MD-2 protein. Quite similar results have been obtained when assessing the interactions of COs having various chemical properties with human and hen egg-white lysozymes. Therefore, COs containing only GlcNAc units revealing higher interaction energies with the two proteins compared with COs containing only GlcN units, and the selectivity of the interactions was dependent on the *MW*, DaD and AP of COs.⁹ It was also true for the interactions between the COs and human plasma proteins (alpha-1 acid glycoprotein and human serum albumin), the interacting energies increased with the molecular weight and with decreasing of deacetylation degree also were dependent on the AP.⁷ In addition, a molecular docking study suggested that chitin deacetylases from fungi and marine bacteria were able to bind both totally acetylated and partially acetylated COs, but the binding energy was usually higher in the cases of the interactions with totally acetylated COs.⁸ Not at least, COs with different chemical properties revealed quite distinct pharmacological profiles.⁶

Results obtained using PLIP software and regarding the types of the interaction between the investigated COs and MD-2 and the amino acids involved in these interactions are presented in Table IV.

TABLE IV. The types of the interaction between the investigated COs and MD-2 and the amino acids involved in these interactions. The interactions between MD-2 and the ligand (eritoran, E55) present in the crystallographic structure (PDB ID 2Z65) are also characterized for comparison purposes; A means *N*-acetyl glucosamine, D means glucosamine

Complex MD-2-COs	Amino acids involved in the interactions	
	Hydrophobic interactions	Hydrogen bonds
Complex made with the ligand present in the crystallographic structure (eritoran)		
Complex MD-2-E55	ILE46, LEU61, ILE63, TYR65, PHE76, PHE104 ILE117, PHE119, PHE121, PHE151	SER120
Complexes made with totally acetylated COs		
Complex MD-2-2A	PHE151, ILE153	—
Complex MD-2-3A	PHE76, GLU92, PHE121, VAL135, PHE151	TYR102, SER120
Complex MD-2-4A	PHE76, PHE121, PHE151	TYR102, SER120

TABLE IV. Continued

Complex MD-2-COs	Amino acids involved in the interactions	
	Hydrophobic interactions	Hydrogen bonds
Complex MD-2-5A	VAL48, ILE52, PHE 76, ILE117, PHE119	TYR102, SER120
Complex MD-2-6A	LEU54, ILE63, PHE76, PHE121, ILE153	TYR102, SER120
Complex MD-2-8A	GLU92, ILE117, PHE119, TYR131, ILE153	ARG96, TYR102, LYS125, SER127
Complexes made with totally deacetylated COs		
Complex MD-2-2D	—	GLU92
Complex MD-2-3D	—	TYR102
Complex MD-2-4D	—	VAL93
Complex MD-2-5D	—	GLU92, VAL93
Complex MD-2-6D	—	ARG96, TYR102(2)
Complex MD-2-8D	—	GLU92, VAL93, TYR102, SER120, LYS122, GLY123
Complexes made with partially deacetylated COs		
Complex MD-2-DA	PHE119	—
Complex MD-2-ADA	ILE63, PHE76, ILE117	TYR102, SER120
Complex MD-2-DDA	ILE32, PHE151, ILE153	TYR102(2), SER120
Complex MD-2-AADD	VAL48, PHE119, PHE121	GLU92, TYR102
Complex-MD-2-ADAD	ILE52, LEU54, PHE121, ILE153	GLU92, TYR102
Complex MD-2-DAAD	LEU61, PHE76, ILE117, PHE119	TYR102(2)
Complex MD-2-DADA	ILE46, LEU61, PHE121	TYR102
Complex MD-2-DDAA	TYR131, PHE151	GLU92, TYR102(2)
Complex-MD-2-ADDA	ILE80, TYR131	GLU92, TYR102, CYS122
Complex-MD-2-DADADA	ILE52, LEU54, PHE121, ILE153	GLU92, ARG96, TYR102
Complex-MD-2-ADADAD	LEU78, PHE119	GLU92, VAL93, CYS95, ARG96, ASP100, ASP101, TYR102, SER120
Complex-MD2-ADDDAD	LEU87, PHE119	GLU92, TYR102, SER120
Complex-MD-2-DDDADA	ILE153	VAL93, ARG96, TYR102(2)
Complex-MD-2-DADADADA	VAL48, LEU61, PHE121, PHE151	ARG90, GLU92, VAL93, TYR102, GLY123, LYS132

Data presented in Table IV reveal that the interactions between totally deacetylated COs and MD-2 protein are based on hydrogen bonds, whereas par-

tially and totally acetylated COs form both hydrophobic interactions and hydrogen bonds with MD-2. The amino acids identified as being involved in the COs interactions with MD-2 usually are among those involved in the interaction of MD-2 with eritoran, the ligand that is present in the crystallographic structure. It underlines that COs are able to interact with MD-2 protein.

The limitations of this study are common to all *in silico* studies, the predictions of the molecular targets and biological activities are totally dependent on the models used by the computational programs and do not allow to take into consideration the concentration of the query molecule. The computational tools considered in this study are widely used in the fields of cheminformatics and/or bioinformatics and have good accuracies for the predictions. Furthermore, the predictions were in the applicability domain for both used predictions tools. In the case of molecular docking study, the main limitation is due to the lack of flexibility of both protein and ligand, also a limitation that is specific to these types of studies. However, further experimental studies are necessary to assess the predicted activities of the COs related to wound healing and their interactions with MD-2 protein, but the experimental design should consider COs with better characterized composition in terms of molecular weight, acetylation degree and acetylation pattern.

CONCLUSION

In the present study, chitooligosaccharides with distinct chemical properties have been analyzed using a computational approach to evaluate their role in the wound healing process. Because it is still not straightforward to obtain COs with well-defined chemical characteristics (length, deacetylation degree and acetylation pattern), the computational approaches offer an advantage in such cases and their results may guide further experimental studies. This investigation confirms the functional role of COs in wound healing. Regardless of their chemical properties, all investigated COs reveal various wound healing activities. However, there are several distinct activities that are revealed by COs with dissimilar chemical properties. The molecular targets for the totally deacetylated COs are different by comparison to totally and partially acetylated COs and COs containing 3 totally acetylated, respectively totally deacetylated monomeric units disclose the wider spectra of the molecular targets. The main molecular targets predicted for the totally and partially acetylated COs are galectins and selectins, proteins that mediate immune response and respectively the cell adhesion during the process of wound healing. Other molecular targets, the myelin-associated glycoproteins are involved in the development of neural network in the damaged region. Fibroblast growth factors are the main class of molecular targets for the totally deacetylated COs and they are involved in inducing cell division and growth by promoting angiogenesis for the regrowth of damaged tissues. Besides the macro-

phage stimulant, hyaluronic acid agonist, angiogenesis stimulant, and membrane integrity agonist, which are predicted activities related to wound healing for all COs regardless of their chemical properties, totally deacetylated COs also act as transcription factors stimulant. The totally acetylated chitoooligosaccharides proved to be better inhibitors of the LPS binding to MD-2 protein.

Taking into account that COs with dissimilar chemical properties may have obvious activities related to the wound healing process, mixtures of COs with distinct properties can be considered suitable candidates as adjuvants in developing scaffolds for the wound healing process.

ИЗВОД

ДУБЉИ УВИД У УПОТРЕБУ ХИТООЛИГОСАХАРИДА У ПРОЦЕСУ ЗАРАСТАЊА РАНА. РАЧУНАРСКИ ПРИСТУП

MARIANA A. MATICA¹, DIANA L. ROMAN^{2,3}, VASILE OSTAFE^{2,3} и ADRIANA ISVORAN^{2,3}

¹Department of Chemistry-Biology, Institute for Advanced Environmental Research, West University of Timisoara, Oituz 4C, 300086 Timisoara, Romania, ²Department of Biology-Chemistry, Faculty of Chemistry, Biology, Geography, West University of Timisoara, 16 Pestalozzi, 300115 Timisoara, Romania и ³Advanced Environmental Research Laboratories (AERL), West University of Timisoara, Oituz 4A, 300086 Timisoara, Romania

Хитоолигосахариди (COs) који садрже до 10 мономерних јединица *N*-ацетил-D-глукозамина и/или D-глукозамина су у води растворни молекули који показују бројне биолошке активности и ниске токсиколошке профиле. У овој студији коришћен је рачунарски приступ за предвиђање укључености хитоолигосахарида који имају посебне хемијске особине (молекулска маса, степен деацетилације и образац ацетилације) у све четири фазе зарастања рана: хемостази, упали, пролиферацији и формирању ткива. Има предвиђања, за изучавање хитоолигосахарида, у погледу њихових молекулских мета и биолошких активности на које се ослања процес зарастања рана. Даље, приступ молекулског доковања коришћен је за процењивање интеракција проучаваних хитоолигосахарида са мијелоидним диференцијацијским фактором 2 (MD-2), протеином укљученим у запаљењским процесима. Истраживање потврђује функционалне улоге проучаваних хитоолигосахарида у зарастању рана. Молекулске мете предсказане за хитоолигосахариде који садрже потпуно и делимично ацетиловане јединице су галектини и селектини, а они предсказани за хитоолигосахариде што садрже потпуно деацетиловане јединице су фактори раста фибробласта, хитоолигосахариди који садрже 3 јединице показујући већи број молекулских мета. Сви ови протеини су укључени у посредовање имуног одговора, индукујући деобу ћелија и лепљење ћелија током процеса зарастања рана. Сви хитоолигосахариди који садрже од 2 до 8 мономерних јединица у стању су да интерагују са MD-2 протеином, стимулишући да су интеракције јаче за хитоолигосахариде који садрже 6 и 8 мономерних јединица. Енергије интеракције расту са порастом молекулске масе и са опадајућим степеном деацетиловања и зависи од обрасца ацетиловања. Међу проучаваним хитоолигосахаридима, потпуно ацетиловани хитоолигосахариди који садрже 6 и 8 *N*-ацетил глукозаминских јединица могу бити бољи инхибитори за LPS везивање на MD-2 протеин. Према томе, смесе хитоолигосахарида са различитим особинама треба сматрати погодним кандидатима за катализаторе у развијању скелета за процес зарастања рана.

(Примљено 2. јула, ревидирано 13. новембра, прихваћено 20. новембра 2022)

REFERENCES

1. I. Aranaz, A. R. Alcántara, M. C. Civera, C. Arias, B. Elorza, A. Heras Caballero, N. Acosta, *Polymers* **13** (2021) 3256 (<https://doi.org/10.3390/polym13193256>)
2. B. Moghadas, A. Solouk, D. Sadeghi, *Polym. Bull.* **78** (2021) 4919 (<https://doi.org/10.1007/s00289-020-03352-8>)
3. L. A. M. van den Broek, C. G. Boeriu, C. V. Stevens, *Chitin and Chitosan: Properties and Applications*, Wiley, New York, 2020, pp. 232–238 (<https://doi.org/10.1002/9781119450467>)
4. X. Guo, T. Sun, R. Zhong, L. Ma, C. You, M. Tian, H. Li, C. Wang, *Front. Pharmacol.* **9** (2018) (<https://doi.org/10.3389/fphar.2018.01412>)
5. J. Li, D. Wang, S.-C. Chang, P.-H. Liang, V. Srivastava, S.-Y. Guu, J.-J. Shie, K.-H. Khoo, V. Bulone, Y. S. Y. Hsieh, *J. Agric. Food. Chem.* **69** (2021) 3371 (<https://doi.org/10.1021/acs.jafc.0c06804>)
6. D. L. Roman, M. Roman, C. Som, M. Schmutz, E. Hernandez, P. Wick, T. Casalini, G. Perale, V. Ostafe, A. Isvoran, *Front. Bioeng. Biotechnol.* **7** (2019) (<https://doi.org/10.3389/fbioe.2019.00214>)
7. D. L. Roman, V. Ostafe, A. Isvoran, *Mar. Drugs* **19** (2021) (<https://doi.org/10.3390/md19030120>)
8. D. L. Roman, M. Roman, H. Sletta, V. Ostafe, A. Isvoran, *J. Mol. Graph. Model.* **88** (2019) 41 (<https://doi.org/10.1016/j.jmgm.2019.01.002>)
9. D. L. Roman, V. Ostafe, A. Isvoran, *J. Mol. Graph. Model.* **100** (2020) 107676 (<https://doi.org/10.1016/j.jmgm.2020.107676>)
10. H. Jafari, K. V. Bernaerts, G. Dodi, A. Shavandi, *Mater. Sci. Eng., C* **117** (2020) 111266 (<https://doi.org/10.1016/j.msec.2020.111266>)
11. B. S. Park, J. O. Lee, *Exp. Mol. Med.* **45** (2013) e66 (<https://doi.org/10.1038/emm.2013.97>)
12. S. Viriyakosol, P. S. Tobias, R. L. Kitchens, T. N. Kirkland, *J. Biol. Chem.* **276** (2001) 38044 (<https://doi.org/10.1074/jbc.M105228200>)
13. Y. Qiao, Y. Ruan, C. Xiong, Q. Xu, P. Wei, P. Ma, X. Bai, Y. Du, *Carbohydr. Polym.* **82** (2010) 405 (<https://doi.org/10.1016/j.carbpol.2010.04.079>)
14. E. M. Jones, C. A. Cochrane, S. L. Percival, *Adv. Wound. Care.* **4** (2015) 431 (<https://doi.org/10.1089/wound.2014.0538>)
15. E. F. Pettersen, T. D. Goddard, C. C. Huang, G. S. Couch, D. M. Greenblatt, E. C. Meng, T. E. Ferrin, *J. Comput. Chem.* **25** (2004) 1605 (<https://doi.org/10.1002/jcc.20084>)
16. D. Gfeller, A. Grosdidier, M. Wirth, A. Daina, O. Michielin, V. Zoete, *Nucleic Acids Res.* **42** (2014) W32 (<https://doi.org/10.1093/nar/gku293>)
17. D. A. Filimonov, A. A. Lagunin, T. A. Gloriozova, A. V. Rudik, D. S. Druzhilovskii, P. V. Pogodin, V. V. Poroikov, *Chem. Heterocycl. Cmpd.* **50** (2014) 444 (<https://doi.org/10.1007/s10593-014-1496-1>)
18. H. M. Kim, B. S. Park, J. I. Kim, S. E. Kim, J. Lee, S. C. Oh, P. Enkhbayar, N. Matsushima, H. Lee, O. J. Yoo, J. O. Lee, *Cell* **130** (2007) 906 (<https://doi.org/10.1016/j.cell.2007.08.002>)
19. A. Grosdidier, V. Zoete, O. Michielin, *Nucleic Acids Res.* **39** (2011) W270 (<https://doi.org/10.1093/nar/gkr366>)
20. S. Salentin, S. Schreiber, V. J. Haupt, M. F. Adasme, M. Schroeder, *Nucleic Acids Res.* **43** (2015) W443 (<https://doi.org/10.1093/nar/gkv315>)

21. N. Panjwani, *Ann. Transl. Med.* **2** (2014) 89 (<https://doi.org/10.3978/j.issn.2305-5839.2014.09.09>)
22. M. Subramaniam, S. Saffaripour, L. Van De Water, P. S. Frenette, T. N. Mayadas, R. O. Hynes, D. D. Wagner, *Am. J. Pathol.* **150** (1997) 1701 (<https://pubmed.ncbi.nlm.nih.gov/9137094/>)
23. H. Tomita, Y. Iwata, F. Ogawa, K. Komura, K. Shimizu, A. Yoshizaki, T. Hara, E. Muroi, K. Yanaba, S. Bae, M. Takenaka, M. Hasegawa, M. Fujimoto, S. Sato, *J. Invest. Dermatol.* **129** (2009) 2059 (<https://doi.org/10.1038/jid.2008.446>)
24. D. S. Allen-Gipson, J. Wong, J. R. Spurzem, J. H. Sisson, T. A. Wyatt, *Am. J. Physiol. Lung. Cell. Mol. Physiol.* **290** (2006) L849 (<https://doi.org/10.1152/ajplung.00373.2005>)
25. A. Ala, A. P. Dhillon, H. J. Hodgson, *Int. J. Exp. Pathol.* **84** (2003) 1 (<https://doi.org/10.1046/j.1365-2613.2003.00235.x>)
26. R. H. Quarles, *J. Neurochem.* **100** (2007) 1431 (<https://doi.org/10.1111/j.1471-4159.2006.04319.x>)
27. S. Yamakawa, K. Hayashida, *Burns Trauma* **7** (2019) 10 (<https://doi.org/10.1186/s41038-019-0148-1>)
28. W. Li, Y. Li, S. Guan, J. Fan, C.-F. Cheng, A. M. Bright, C. Chinn, M. Chen, D. T. Woodley, *EMBO J.* **26** (2007) 1221 (<https://doi.org/10.1038/sj.emboj.7601579>)
29. J. Guo, C. Chang, W. Li, *Expert. Rev. Proteomics* **14** (2017) 665 (<https://doi.org/10.1080/14789450.2017.1355244>)
30. S. Gingis-Velitski, A. Zetser, M. Y. Flugelman, I. Vlodavsky, N. Ilan, *J. Biol. Chem.* **279** (2004) 23536 (<https://doi.org/10.1074/jbc.M400554200>)
31. M. D. Bagood, R. R. Isseroff, *Int. J. Mol. Sci.* **22** (2021) (<https://doi.org/10.3390/ijms22116135>)
32. L. Thomas, S. Mathew, S. Johnson, *Inform. Med. Unlocked* **20** (2020) 100406 (<https://doi.org/10.1016/j.imu.2020.100406>)
33. G. R. Vasta, *Nat. Rev. Microbiol.* **7** (2009) 424 (<https://doi.org/10.1038/nrmicro2146>)
34. K. Masuoka, M. Ishihara, T. Asazuma, H. Hattori, T. Matsui, B. Takase, Y. Kanatani, M. Fujita, Y. Saito, H. Yura, K. Fujikawa, K. Nemoto, *Biomaterials* **26** (2005) 3277 (<https://doi.org/10.1016/j.biomaterials.2004.07.061>)
35. H. Quan, F. Zhu, X. Han, Z. Xu, Y. Zhao, Z. Miao, *Med. Hypotheses* **73** (2009) 205 (<https://doi.org/10.1016/j.mehy.2009.02.018>)
36. M. Jiang, X. Zhuge, Y. Yang, X. Gu, F. Ding, *Neurosci. Lett.* **454** (2009) 239 (<https://doi.org/10.1016/j.neulet.2009.03.042>)
37. M. Jiang, Q. Cheng, W. Su, C. Wang, Y. Yang, Z. Cao, F. Ding, *Neurochem. Res.* **39** (2014) 2047 (<https://doi.org/10.1007/s11064-014-1387-y>)
38. V. Voinchet, P. Vasseur, J. Kern, *Am. J. Clin. Dermatol.* **7** (2006) 353 (<https://doi.org/10.2165/00128071-200607060-00003>)
39. T. Liu, L. Zhang, D. Joo, S.-C. Sun, *Signal. Transduct. Target.* **2** (2017) 17023 (<https://doi.org/10.1038/sigtrans.2017.23>)
40. H. Huang, Y. Zou, H. Chi, *Drug. Des. Devel. Ther.* **12** (2017) 67 (<https://doi.org/10.2147/DDDT.S148064>).



Formation of intermediate gas–liquid system in aromatics’ thin layers

ROSTISLAV V. KAPUSTIN¹, IOSIF I. GRINVALD^{1*}, ANDREY V. VOROTYNTEV²,
ANTON N. PETUKHOV^{2,3}, VLADIMIR M. VOROTYNTEV¹, SERGEY S. SUVOROV²
and ALEXANDRA V. BARYSCHEVA²

¹Alekseev State Technical University of Nizhny Novgorod, Nizhny Novgorod, Russia,

²Lobachevsky State University of Nizhny Novgorod, Nizhny Novgorod, Russia

and ³Dmitry Mendelev University, Moscow, Russia

(Received 3 October, revised 25 November, accepted 9 December 2022)

Abstract: The present work discusses IR spectroscopic experiments and quantum-chemical DFT study of structure and intermolecular binding in the intermediate gas–liquid systems of aromatics, namely, benzene, furane, pyridine and thiophene. These systems can be generated in thin layers near a solid surface by two different methods, depending on the physical properties of the sample. The first method includes evaporation with a subsequent compression of a sample in an optical cell of variable thickness, and it is applied to volatile components: benzene, furane, thiophene. For benzene and pyridine the second method is used, which involves a heating-initiated evaporation into a closed inter-window space with an after-cooling of a sample. It was shown that the formed layer is not an adsorbate or a condensate. The IR data obtained by these two methods lead to conclusion that the given systems of the considered aromatics manifest dual gas–liquid spectral properties which can change each into other by varying external conditions. According to the DFT calculation results, the spatial arrangement in the aromatic thin layers can be described as a combination of π - and σ -bonded clusters, which simulate the gas and the liquid phase state properties.

Keywords: fluid-like; intermediate phase; IR spectroscopy; DFT calculations.

INTRODUCTION

The concept of thin layers in the near-surface area was mentioned in the works of Ananikov’s group, which deal with the mechanisms of heterogeneous catalysis.¹ This term primarily refers to catalytically active metal particles, and it can mean both a nanoscale layer and molecular clusters. However, later it was shown that the very concept of the thin layer has a much wider application. The

* Corresponding author. E-mail: grinwald@mts-nn.ru
<https://doi.org/10.2298/JSC211003087K>

thin-layer effect was observed in different phase states of organic liquids: in a solid-film-encapsulated form, in a thin-layer liquid on a solid surface, in dense vapours near a solid surface, and also in a low-temperature matrix.²

Various theoretical and experimental methods for studying transient thin-layer systems have been suggested, including *ab initio* DFT calculations in the Gaussian software package (B3LYP 6–311++G [2d, 2p] basis set), which make it possible not only to optimize the geometry of molecular clusters, but also to compare theoretical IR vibrational spectra with experimental ones directly.³ However, the available computing schemes does not allow to calculate the entire supramolecular system in all its complexity and heterogeneity, being limited only to isolated clusters. Therefore, only the experimental *in situ* IR spectral methods for studying organic-compound thin layers make it possible to reveal their unique phase properties and make assumptions about their spatial structure.⁴

The structure and properties of the thin layers can vary and manifest themselves differently depending on the method of generation, the state of aggregation, and the class of the compound, as well as the types of intermolecular interaction prevailing in it. For example, in liquid chlorocarbons, chlorine acts as the main binding particle for gaseous clusters' and condensed supramolecular structures. Accordingly, tetrachloromethane forms the most stable thin-layer gas-phase system among them. The unusual intermolecular properties of tetrachloromethane were predicted in the spectral study.⁵ There was shown that gas-phase tetrachloromethane exists not only in the single molecular shape that has T_d symmetry, but also in the transformed shape having C_{3v} symmetry. This speculation was confirmed by the spectra of gaseous tetrachloromethane at various temperatures. It was resumed that the pyramidal structure relates to the cluster shape, where the chlorine atom provides the binding between molecules. The chlorine atom shift in the cluster can occur owing to the association of the molecules. It leads to the transformation of the molecular geometry to the almost planar D_{3h} symmetry, in which A_1 stretching band is forbidden in IR spectra. The above interpretation of the liquid chlorocarbons' IR spectral data based on the symmetry point groups' theory showed the appearance of two structural modifications – the pyramidal C_{3v} and the biplanar D_{2h} or D_{2v} symmetry. The DFT calculations also predicted the transformation of the initial isomer into biplanar and pyramidal ones. Thus, it was concluded that the phase characteristics in chlorocarbons can be combined: in the gas phase, some interactions resembling liquid ones may retain, and *vice versa*.

The most unusual and chemically resistant form of the studied thin layers are solid-phase chlorosilane films with an encapsulated liquid, generated in an argon atmosphere – they are able to selectively protect the internal component, preventing its air hydrolysis (which could be explosive),⁶ but allowing slow oxidation

over months, which was repeatedly confirmed by IR spectroscopy and electron microscopy data.⁷

Systems that combine gaseous and liquid physicochemical properties are known as supercritical fluids (SCF).⁸ They can dissolve large volumes of gases and mix indefinitely with each other. In addition, a slight adjustment of pressure and temperature within the limits of supercritical values makes it possible to influence the density of the SCF and its other parameters to such an extent that, in the phase diagram, the SCF is even conditionally divided into gas-like and liquid-like states. Although there is actually no clear boundary between these two states, many researchers conditionally draw it along the so-called Widom line, the transition through which is described by the term pseudo-boiling, which once again emphasizes the variability degree of the SCF physicochemical properties under changing external conditions. One of the most reliable methods for tracking such phase transformations is considered to be IR spectroscopy, since it allows one to unambiguously assign some individual characteristic bands to the gas or liquid phase and thus clearly distinguish between the gas and liquid properties of the sample.⁹ In the thin layers of chloromethanes and chloroethanes, it was possible to reproduce the main properties of SCF. Specifically, in the IR spectra, two separate phases – gas-like and liquid-like – were distinguished by their manifestation in the characteristic bands that change a shape depending on the phase state of the substance. Similar to the SCF, in the thin layers these states smoothly and continuously change each into other with a slight adjustment of pressure and temperature. Depending on the boiling point of the component, under ambient conditions it may appear in the thin layers more as a gas-like or liquid-like one.¹⁰ It is important to note that the terms “gas-like” and “liquid-like” used in the thin-layer system description are not accidental or intended to emphasize the similarity of a given state with a fluid. The states observed by IR spectroscopy are in fact neither a real gas nor a real liquid, but only exhibit some of their spectral properties, which is easy to prove: it is almost impossible to obtain the IR spectrum of a real gas at an equilibrium vapor pressure in the thin spectral cell (1–6 mm).

As already mentioned, the properties of thin-layer gas–liquid systems are largely determined by the types of intermolecular bonding. For this reason, the compounds with aromatic properties, both proper hydrocarbons and heterocycles, are of particular interest for study since they are distinguished from the other previously studied organic compounds by their intermolecular interactions. Back in the 70s Shakhpargonov, who predicted the existence of the specific interactions in the non-polar hydrogen-bonded liquids, suggested the formation of molecular π -complexes (molecular stacks) between aromatic rings.¹¹ Later, this concept was confirmed and developed by Abramovich's group.^{12–14} The single benzene molecule geometry is usually taken as a planar ring. This geometry corresponds

to D_{6h} symmetry point group; according to the selection rules, only one stretching C–H band (*E*-specie) should be active in its IR spectra. Nevertheless, in the real liquid benzene spectra there are three bands, and in the solid benzene there are even four bands in C–H stretching region. Three bands that have isotopic H/D shift close to the theoretical prediction also are observed in benzene-d₆ spectrum. This spectral picture is assigned to the existence of two molecular forms in the liquid phase: a planar shape, in which one IR band is active (D_{6h} symmetry), and a shape with two IR bands (A_1 - and *E*-species), corresponding to the C_{3v} symmetry. Assumedly, the benzene molecule exists in the liquid state as a cluster system, where C–H bonds deviate from the ring plane to the neighbouring molecule, which leads to a distortion of the C–H stretching vibrations' symmetry.¹⁵

In solution of dichlorobenzene, there are strong neighbouring-molecule interactions between chlorine atom and carbon in the aromatic ring and between carbon atoms as well. Since the arrangements of molecules in a crystal always correspond to the potential energy minima of the system, it can be used to verify the results of molecular light scattering experiments combined with modelling procedure and consequently reveal the structure and characteristics of the mutual arrangement in molecules as well as the intermolecular binding types in the liquid phase.¹⁶

A structural element that determines the molecular arrangement in the benzene liquid phase, was earlier presented as a set of dimers that have several geometry configurations. Later, the trimers were considered as a formed element in the stack model of the benzene liquid phase. The conducted DFT calculations with different transformations of the initial molecular geometry predict that the optimal configuration is the stack with a chair shape of the central and two planar rings; the trimers are bonded in a spatial structure by the hydrogen bridges.¹⁷ This concept explained the IR data outside the scope of traditional assignment. In the trimer spectrum, a C–H stretching band assigning to both planar rings should be observed while the C–H central-ring stretching exhibits two bands: the first one assigns to a pair of equivalent (C₁–H₁) and (C₄–H₄) bonds, and the second one – to a quartet: (C_i–H_j), $i = 2.3$ or 5.6 . The stretching bands of the hydrogen bridges shift in the middle IR region due to the mixing of the C–H and C–C stretching. Consequently, there is a pair of bands that corresponds to two bridging C–H bonds' stretching in the stacks bound in two mutually perpendicular plains, as it was shown earlier.¹⁸

Based on the data presented above, it can be stated that the formation mechanism of the thin-layer systems with dual gas–liquid phase characteristics is caused and provided by the intermolecular binding. Using the example of chloro-carbons and chlorosilanes, one can see how the properties of the thin layers change depending on the supramolecular geometry. The formation of certain stable structures with unusual phase properties indirectly confirms the presence

of nonstandard intermolecular binding, which is realized through such structures. Thus, the experimental studies of the thin aromatic layers considered in the present work are intended to find a new and more reliable confirmation of the above assumptions about the supramolecular geometry of aromatics. If the intermolecular binding is indeed the thin-layer systems' basis, then the properties of such systems for aromatics should differ from chlorides to the same extent as their supramolecular characteristics do. Pure benzene, a common organic solvent that can be directly compared with liquid chlorocarbons, is studied as a typical representative of aromatics. Moreover, it is very promising to study heterocycles, which are known to have some aromatic properties as well. Below we consider the question of whether there are some heterocyclic intermolecular interactions, and are they the reason the characteristics of their thin-layer systems differ from those of benzene. In order to clearly distinguish between the proper aromatic properties, which manifest themselves to the same extent in various heterocycles, from the intermolecular interactions of the heteroatom itself, which change depending on the compound, we have selected three aromatic heterocycles with different heteroatoms: thiophene, furane and pyridine. The main objective of the work is to study the four selected substances under conditions as close as possible to those in which the chlorides were considered, for the most accurate comparison. As a part of the presented work, we have concluded an extensive quantum-chemical study based on the DFT calculations, which is also expected to complement the earlier theoretical studies of chlorocarbons with the data on intermolecular binding in the aromatics and allow the quantum chemical model of the gas-liquid thin-layer system structure to be evaluated for the varied classes of compounds in terms of DFT study.

EXPERIMENTAL

In the present work, as mentioned above, four components were studied: benzene, thiophene, furane and pyridine. The optimal parameters for thin-layer gas-liquid systems' generation (evaporation time, τ , cell type, heating temperature, T and boiling point, T_B) depend on the individual properties of each component, primarily its boiling point, as shown in the Table I.

TABLE I. The optimal parameters for the selected compounds' transient state formation

Compound	τ / min	Cell type	T / K	T_B / K
Benzene	60	VTOC/MCOH	295/323	353
Thiophene	60	VTOC	295	357
Furane	25	VTOC	295	304
Pyridine	10	MCOH	363	389

For the selected components, whose intense evaporation do not require additional heating, a Perkin-Elmer variable-thickness optical cell was applied (here we use the abbreviation VTOC). This method was described in detail in the earlier paper.¹⁰ The formation of the dual gas-liquid thin-layer system occurred under the compression-extension procedure of the cell

inter-window distance from 6 to 1 mm and in reverse. The optimal evaporation time required for the gas–liquid state formation depends on the boiling point of compound and varies from 25 to 60 min.

The effect of the thin gas–liquid layers generation for benzene and low-volatile pyridine has been achieved by the method of evaporation of liquid sample placed between optical window in following way. The sample drops (Fig. 1, 1) on the edge of a KBr optical window (Fig. 1, 2) so that to prevent its falling into the IR optical beam (Fig. 1, 3) under a Teflon® 1-mm-thickness gasket (Fig. 1, 4), covering them from above with another optical window (Fig. 1, 5). Then both windows with a gasket between them are placing and clamping in a manual collapsible optical holder (here we use the abbreviation MCOH) for subsequent heating up to optimal for this experiment’s temperature (Table I).

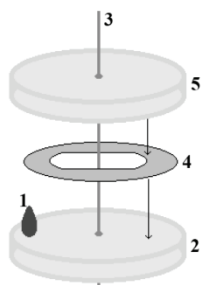


Fig. 1. The scheme of the thin-layer system heating-accelerated generation and detection.

For the spectral detection and study of the generated state, IR spectra recorded in the VTOC and the MCOH were compared with those obtained in a gas cell (for a gas phase) and for a liquid phase between optical windows at ambient conditions. The effectiveness and accuracy of the two methods used for the study of the thin-layer systems generation was previously demonstrated in our works.^{7,10}

It was proved that the revealed layer is not an adsorbate or a condensate because the IR spectra of substances, evaporated into the VTOC at 6 mm thickness, disappeared after the cell thickness compression to 0.05 mm. Besides, the layer origin was tested by described heating method. The layers have been formed by the heating-accelerated evaporation into the cell with 1 mm gasket, while at the same procedure conducted with 0.2 mm gasket, the intermediate shape was not detected.

IR-spectra were recorded by IR-Fourier spectrometers IR Affinity1 (Shimadzu Co. Inc.) and FISM 1202 (InfraSpec Co. Ltd.) in 500–4000 cm⁻¹ range with 2 cm⁻¹ resolution and 60 scans. The spectra fragments are given in the figures with the wavenumber axis expansion according to the original record. The VTOC used was manufactured by Perkin–Elmer Co. Ltd.

The purity of the components was not less than 99.9 % as it was confirmed by chromat–mass spectrometry data obtained by GCMS–QP2010 Plus spectrometer (Shimadzu Co. Inc.).

RESULTS AND DISCUSSION

In this section, the IR results for selected aromatics, including benzene and heterocycles, are presented. We highlighted the C–H out-of-plane bending vibration (800–600 cm⁻¹) and high frequencies’ (3000–2000 cm⁻¹) regions. The main manifestations of the thin layer formation could be expected in these ranges, because the first of them is sensitive to the intermolecular “stack” binding

and the second one can display the E···H ($E = C, O, S$ or N) intermolecular binding in “chains”.¹⁷

The most valuable results for benzene were obtained by heating of the sample between optical windows and subsequent evaporation into VTOC (see section Experimental). In the experiments with furane and thiophene, the gas–liquid systems were generated in VTOC, while for pyridine, they were obtained by heating between optical windows.

Gas–liquid system in the thin layers of benzene

The band of C–H out-of-plane bending vibration with maximum at 673 cm^{-1} , resembling the band in a gas phase (Fig. 2, spectrum A) with poorly resolved P-, Q- and R-branches, was revealed at the sample evaporation procedure in VTOC by the thickness compression from 6 to 1 mm (Fig. 2, spectrum C). At the minimal cell thickness of 0.05 mm, the C band disappears. At the thin-layer generation by heating of the sample between optical windows without a gasket, the C band of spectrum was not observed as well. Therefore, we can conclude that this band is not assigned to the adsorbed molecular layer. As the spectrum of the equilibrium gas phase cannot be observed at 1 mm optical cell thickness, the observed band can be attributed to the transient shape that appears in the thin layers and combines gas and liquid properties. The band of liquid benzene can be considered as the gas-phase band transformation through the transitional phase state band (Fig. 2, spectrum A).

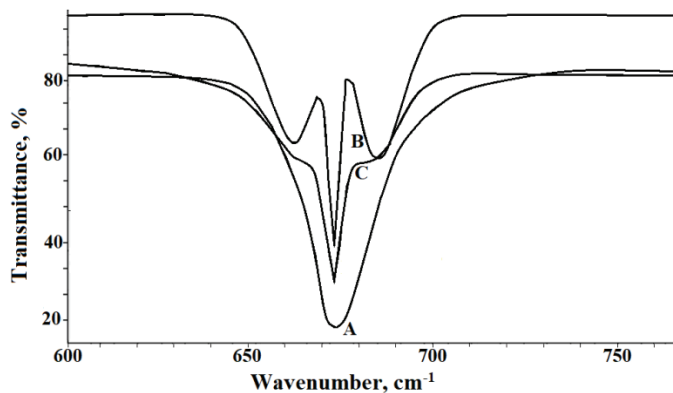


Fig. 2. Fragment of benzene spectra in C–H out-of-plane bending vibration range.
Spectra: A – liquid phase; B – gas phase; C – transient phase in the thin layer.

In the spectra obtained by evaporation of the sample, placed between optical windows, with the heating to 323 K, the new bands at $654, 685$ and 730 cm^{-1} were revealed (Fig. 3, spectrum B). The first two of them appears near the P- and R-branches of gaseous benzene, at 659 and 687 cm^{-1} , respectively (Fig. 3, spectrum A), while the third band is located closely to the position of the similar

mono-substituted arenes' band. The spectrum "B" after cooling transforms into the spectrum of the transitional shape, presented in Fig. 2 (spectrum C). These data can be interpreted as a manifestation of the benzene thin layer formation with the structure and binding that differ from the ones obtained in the method above by the evaporation into VTOC.

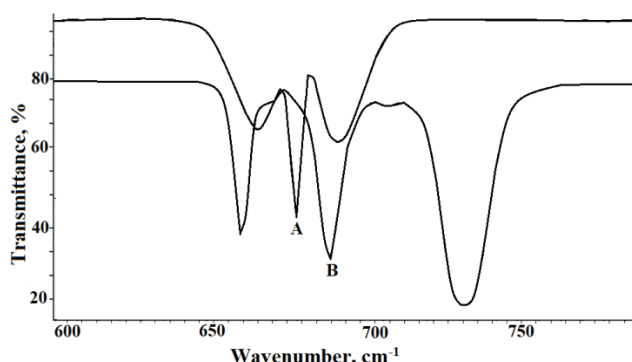


Fig. 3. Fragment of benzene spectra in C–H out-of-plane bending vibration range.
Spectra: A – gaseous benzene; B – benzene transient shape in the thin layer.

Gas–liquid systems in the thin layers of thiophene and furane

In the spectra of furane, obtained at the evaporation into VTOC and subsequent lowering of the cell thickness from 6 to 1 mm, the bands at 759, 749 and 727 cm^{-1} were detected (Fig. 4A, spectrum C). The position of the central band is very close to one in the spectrum of liquid (Fig. 4A, spectrum A) and gaseous furane (Fig. 4A, spectrum B). As the spectrum of a real gas phase cannot be recorded at 1 mm cell thickness, the spectrum C can be assigned to the transient gas–liquid system of furane forming in the thin layer, as well as in the benzene spectrum above.

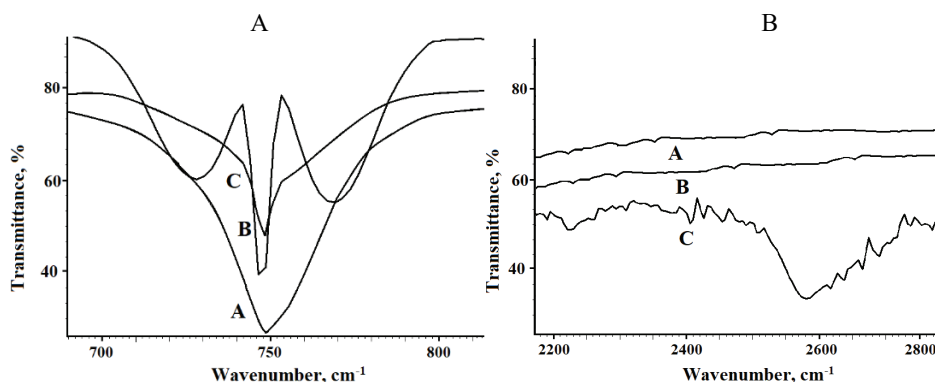


Fig. 4. Furane spectra in C–H out-of-plane bending vibration (A) and high-frequency (B) ranges. Spectra: A – liquid phase; B – gas phase, C – transient shape in the thin layer.

The new bands of the thin layer system are detected at 2598 cm^{-1} , unlike the benzene gas–liquid system (Fig. 4B, spectrum C). In the spectra of liquid and gaseous furane, these bands are absent (Fig. 4B, spectra A and B). Since this region ($3600\text{--}3000\text{ cm}^{-1}$) is characteristic for the O–H stretching vibrations, the revealed band can be assigned to the intermolecular O···H stretching that arises in the thin-layer gas–liquid shape.

The similar spectral picture was observed for thiophene in the C–H out-of-plane bending and the high-frequency regions (Fig. 5A). The band at 2151 cm^{-1} can be assigned to the S···H intermolecular stretching in the thin-layer gas–liquid system of thiophene (Fig. 5B).

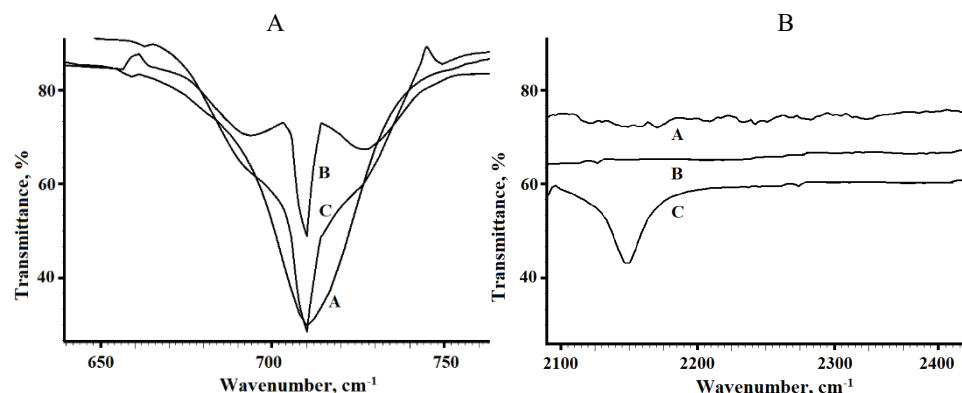


Fig. 5. Thiophene spectra in C–H out-of-plane bending vibration (A) and high-frequency (B) ranges. Spectra: A – liquid phase; B – gas phase; C – transient phase in the thin layer.

Gas–liquid system in the thin layers of pyridine

For pyridine, the generation of the thin layer system can be accomplished by heating to 373 K in the inter-window space with a 1 mm cell gasket. The observed IR absorption (Fig. 6A, spectrum B) is presented in comparison with the liquid phase (Fig. 6A, spectrum A). The spectrum of pyridine equilibrium gas phase spectrum cannot be recorded due to low volatility of the substance. However, in this case, the transition shape with dual gas–liquid spectral properties was also observed.

In the high-frequency region, a new band in the IR spectrum of the generated thin layer at 3420 cm^{-1} was observed (Fig. 6B, spectrum B). This band can be assigned to an intermolecular N···H hydrogen bond forming within an intermediate shape.

DFT modelling of intermolecular binding in the thin layers

The description of the intermolecular binding in a condensed state can be considered in terms of DFT study only as a quantitative model. It is well-known that

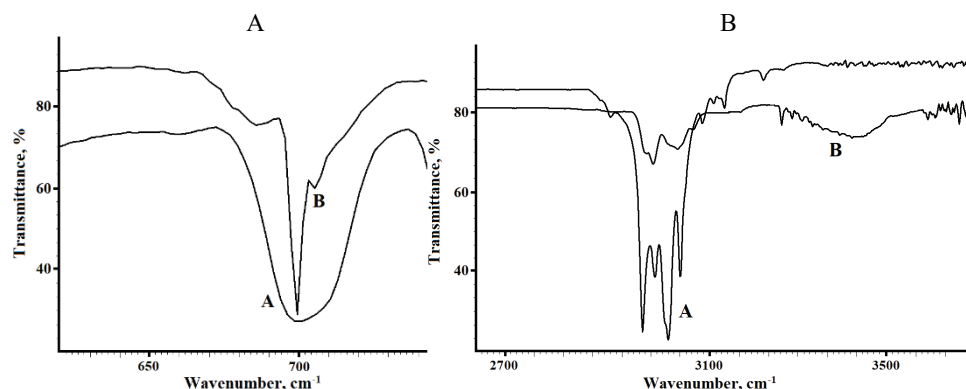


Fig. 6. Pyridine spectra in C–H out-of-plane bending vibration (A) and high-frequency (B) ranges. Spectra: A – liquid phase; B – transient phase in the thin layer.

ab initio quantum chemical calculations simulate the condensed phase for organic molecules as a set of dimers, trimers and rarely as polymolecular clusters.^{3,17,18} Therefore, our effort to evaluate the intermolecular binding in the gas-liquid system of the thin layers is based on the similar conception, including the calculation of the dimer structure parameters for the different molecular shapes. The aromatics' system can exist in spatial arrangements of so called "stack" shape – with parallel and perpendicular oriented aromatic rings.¹⁸ However, the IR data indicate the formation of the C···H interstack σ -binding as well.^{17,18} The results of DFT study, in terms of the similar concept, are presented in this Section.

The calculations were carried out in terms of DFT technique with B3LYP and GD3BJ functionals^{19,20} with 6–311++G (2d, 2p) basis set. For geometry optimization procedure we have used the algorithm²¹. The intermolecular distances calculated by the B3LYP functional are given in Figs. 7–10 in brackets. The additional criterium of a system geometry correct calculation is the absence of negative vibration frequencies in the final data set.

Benzene system. Two types of clusters, which represent the benzene spatial arrangement, are given in Fig. 7. DFT calculations of the optimized geometry for structure A ("stack" shape) in the variant with the B3LYP functional gives a geometry with aromatic rings arranged at an angle, so the comparison of the intermolecular bond lengths with the GD3BJ functional can be taken rather conditionally, hence the bond lengths obtained by the B3LYP functional are not given. The calculated spectral data for these structures generally agree with the experimental IR picture in CH stretching region, in which three bands are observed instead of one CH stretching band prevised for the planar isolated ring (this problem was discussed earlier).¹⁸ The calculations predict two bands assigning to the shape with parallel (Fig. 7A) and one band for the "T" shape (Fig. 7B). The com-

bination of these arrangement variants leads to the appearance of three bands in the spectra (Table II).

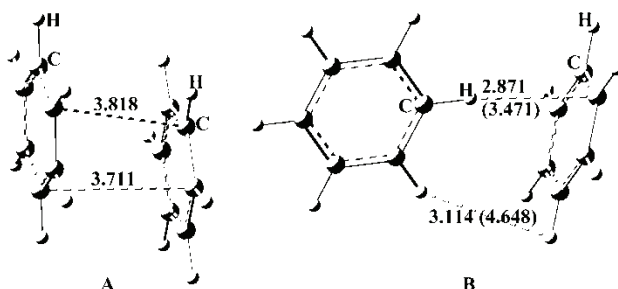


Fig. 7. Elements of spatial arrangement with optimized geometry parameters of the benzene clusters (the distances are given in Å).

The calculated IR frequencies correctly predict the existence of three bands in the CH stretching region arising due to the bands' combination of two molecular shapes – A and B.¹⁷

TABLE II. The experimental and calculated frequencies data of CH stretching bands

Frequencies	Wavenumber, cm ⁻¹
Experimental	3092, 3071, 3036
Calculated	3122, 3053 (shape A), 3179 (shape B)

Furane and thiophene systems. For the furan molecule, the geometry optimization procedure gives two variants of σ-bonded dimers – one with the at-an-angle aromatic rings' arrangement and the intermolecular (C–C) distance of about 3.1 Å (Fig. 8A) and with the distance of about 2.7 Å (Fig. 8B). The thin-layer transient gas-liquid system, in terms of the similar model, can form under the O···H intermolecular bonded clusters with two molecular arrangement types.

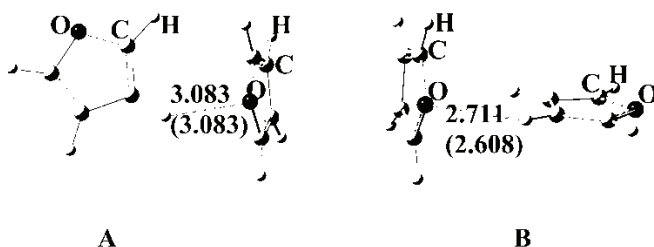


Fig. 8. Elements of spatial arrangement with optimized geometry parameters of the furan clusters (the distances are given in Å).

The structure of thiophene gas-liquid system in the thin layer predicted in DFT calculation can be presented as a state with two different shapes π-bonded

(“stack” shape) and σ -bonded S···H shape (Fig. 9). In this case, DFT calculations with the B3LYP potential do not give an optimized geometry for the “stack” shape, so these values are not shown in Fig. 9.

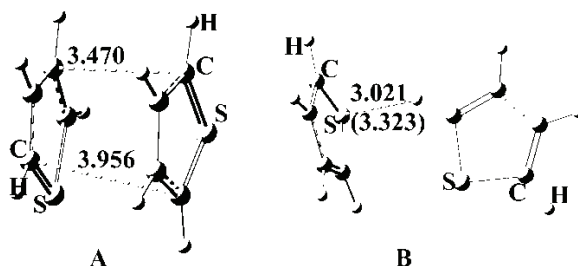


Fig. 9. Elements of spatial arrangement with optimized geometry parameters of the thiophene clusters (the distances are given in Å).

The calculated IR frequencies in CH out-of-plane bending (Q-branch only) and CH stretching ranges, where the manifestation of intermediate phase shape formation was observed, are presented in Table III (for the GD3BJ functional only). The calculated and relative experimental intensities were not listed in Table III, because these values strongly depend on the experimental conditions and do not give any useful information in terms of the considered problem.

TABLE III. The calculated and experimental IR frequencies of heterocyclic aromatics in ranges of CH out of plane bending – $\rho(\text{CH})$ and CH···X stretching – $q(\text{CH})$

Frequencies	Wavenumber, cm^{-1}					
	$\text{C}_5\text{H}_5\text{O}$		$\text{C}_5\text{H}_5\text{S}$		$\text{C}_6\text{H}_6\text{N}$	
	$\rho(\text{CH})$	$q(\text{CH}\cdots\text{O})$	$\rho(\text{CH})$	$q(\text{CH}\cdots\text{S})$	$\rho(\text{CH})$	$q(\text{CH}\cdots\text{N})$
Experimental	749	2598	709	2151	698	3420
Calculated	Shape A	756	3259	723	3253	712
	Shape B	757	3259	723	3253	716
						3156
						3174

Significant differences for the calculated and experimental frequencies for the CH···X stretching vibrations are probably caused by the hydrogen atom shift to the heteroatoms in the real systems.²²

Pyridine system. The cluster structure of pyridine system predicted in the DFT study with the GD3BJ functional can be presented as a state with combination of “stack” shape (Fig. 10A) and σ - one formed under the intermolecular hydrogen N···H bond (Fig. 10B).

CONCLUSION

The presented experimental and computational data allow to make the following main conclusions.

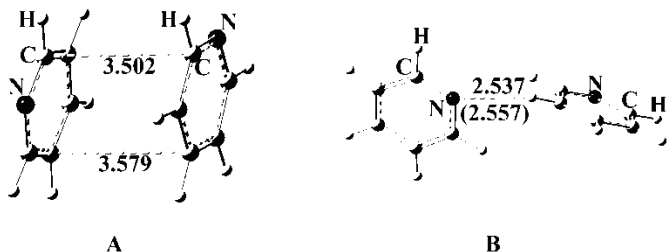


Fig. 10. Elements of spatial arrangement with optimized geometry parameters of the pyridine clusters (distances are given in Å)

1. The gas–liquid systems of aromatics including heterocyclic aromatic compounds can be generated in the thin layers by evaporation and subsequent compression of the substances in VTOC, or by heating of the sample placed between optical windows and evaporation into the small inter-window space.
2. These systems manifest the dual gas–liquid spectral properties of the considered aromatics. In terms of the presented concept, their structure can be interpreted as a transient phase state arising at the liquid state transformation into the gas.
3. The spatial arrangement of the thin layers can be described as a combination of π - and σ - bonded clusters, which can simulate the gas and the liquid phase state properties. Therefore, the thin layers can be considered as an intermediate state of organic liquids.

Acknowledgement. The study was supported by Ministry of Science and Higher Education of the Russian Federation as part of the scientific project FSSM-2021-0013 of the Laboratory of Smart Materials and Technology (LSMT).

ИЗВОД

ФОРМИРАЊЕ ИНТЕРМЕДИЈАРНОГ СИСТЕМА ГАС–ТЕЧНО У ТАНКИМ СЛОЈЕВИМА АРОМАТИЧНИХ ЈЕДИЊЕЊА

ROSTISLAV V. KAPUSTIN¹, IOSIF I. GRINVALD¹, ANDREY V. VOROTYNTSEV², ANTON N. PETUKHOV^{2,3}, VLADIMIR M. VOROTYNTSEV⁴, SERGEY S. SUVOROV² и ALEXANDRA V. BARYSCHEVA²

¹Alekseev State Technical University of Nizhny Novgorod, Nizhny Novgorod, Russia, ²Lobachevsky State University of Nizhny Novgorod, Nizhny Novgorod, Russia и ³Dmitry Mendelev University, Moscow, Russia

У овом раду разматрани су подаци добијени IC спектроскопским експериментима и квантно-хемијским DFT испитивањем структуре и интермолекулских веза у интермедијерним системима гас–течно ароматичних једињења бензена, фурана, пиридина и тиофена. Ови системи могу настати у танким слојевима у близини чврсте површине применом две различите методе, у зависности од физичких особина узорка. Прва метода, која укључује исправање а затим компресију узорка у оптичкој ћелији променљиве дебљине, је примењена на испарљива једињења: бензен, фуран и тиофен. За бензен и пиридин, коришћена је друга метода, која подразумева испаравање иницирано загревањем у затвореном простору између прозора са накнадним хлађењем узорка. Показано је да настали слој није адсорбат или кондензат. На основу IC података добијених овим двема

методама може се закључити да добијени системи кондензованих ароматичних једињења показују дуалне гас–течно спектралне особине које могу прелазити из једних у друге у случају варирања спољних услова. Резултати DFT прорачуна показају да се просторно уређење у танким слојевима ароматичних једињења може описати као комбинација π - и σ -повезаних кластера, које симулирају особине гасне и течне фазе.

(Примљено 3. октобра, ревидирано 25 новембра, прихваћено 9. децембра 2022)

REFERENCES

1. D. B. Eremin, V. P. Ananikov, *Coord. Chem. Rev.* **346** (2017) 2 (<https://dx.doi.org/10.1016/j.ccr.2016.12.021>)
2. I. I. Grinvald, I. Y. Kalagaev, A. N. Petukhov, A. I. Grushevskaya, R. V. Kapustin, I. V. Vorotyntsev, *J. Struct. Chem.* **59** (2018) 313 (<https://dx.doi.org/10.1134/S0022476618020087>)
3. M. A. Palafox, *Phys. Sci. Rev.* **3** (2018) (<https://dx.doi.org/10.1515/psr-2017-0184>)
4. B. C. Smith, *Infrared Spectral Interpretation: A Systematic Approach*, 1st ed., CRC Press, Boca Raton, FL, 2018 (<https://dx.doi.org/10.1201/9780203750841>)
5. I. I. Grinvald, I. Y. Kalagaev, A. N. Petukhov, A. V. Vorotyntsev, R. V. Kapustin, *Struct. Chem.* **30** (2019) 1659 (<https://dx.doi.org/10.1007/s11224-019-01349-2>)
6. G. Szabó, D. Szieberth, L. Nyulászi, *Struct. Chem.* **26** (2015) 231 (<https://dx.doi.org/10.1007/s11224-014-0543-y>)
7. R. V. Kapustin, I. I. Grinvald, A. V. Vorotyntsev, A. N. Petukhov, V. I. Pryakhina, I. V. Vorotyntsev, *React. Kin. Mech. Catal.* **135** (2022) 835 (<https://dx.doi.org/10.1007/s11144-022-02177-y>)
8. E. S. Alekseev, A. Y. Alentiev, A. S. Belova, V. I. Bogdan, T. V. Bogdan, A. V. Bystrova, E. R. Gafarova, E. N. Golubeva, E. A. Grebenik, O. I. Gromov, V. A. Davankov, S. G. Zlotin, M. G. Kiselev, A. E. Koklin, Y. N. Kononevich, A. E. Lazhko, V. V. Lunin, S. E. Lyubimov, O. N. Martyanov, I. I. Mishanin, A. M. Muzafarov, N. S. Nesterov, A. Y. Nikolaev, R. D. Oparin, O. O. Parenago, O. P. Parenago, Y. A. Pokusaeva, I. A. Ronova, A. B. Solovieva, M. N. Temnikov, P. S. Timashev, O. V. Turova, E. V. Filatova, A. A. Philippov, A. M. Chibiryakov, A. S. Shalygin, *Russ. Chem. Rev.* **89** (2020) 1337 (<https://dx.doi.org/10.1070/rer4932>)
9. N. J. Hestand, S. E. Strong, L. Shi, J. L. Skinner, *J. Chem. Phys.* **150** (2019) 054505 (<https://dx.doi.org/10.1063/1.5079232>)
10. I. I. Grinvald, R. V. Kapustin, *J. Serb. Chem. Soc.* **86** (2021) 1067 (<https://dx.doi.org/10.2298/JSC210426048G>)
11. M. I. Shakhparonov, *Contemporary Problems of Physical Chemistry*, Lomonosov Moscow State University Publishing House, Moscow, 1970
12. A. I. Abramovich, L. V. Lanshina, I. D. Kargin, *Russ. Chem. Bull.* **66** (2017) 828 (<https://dx.doi.org/10.1007/s11172-017-1814-8>)
13. I. D. Kargin, L. V. Lanshina, A. I. Abramovich, *Russ. J. Phys. Chem., A* **91** (2017) 1737 (<https://dx.doi.org/10.1134/S003602441709014X>)
14. A. I. Abramovich, *Struct. Chem.* **30** (2019) 545 (<https://dx.doi.org/10.1007/s11224-019-01293-1>)
15. I. I. Grinvald, I. Y. Kalagaev, A. N. Petukhov, R. V. Kapustin, *Russ. J. Phys. Chem., A* **93** (2019) 2645 (<https://dx.doi.org/10.1134/S0036024419130107>)

16. A. I. Abramovich, E. S. Alekseev, T. V. Bogdan, *Russ. J. Phys. Chem., A* **93** (2019) 2108 (<https://dx.doi.org/10.1134/S0036024419110025>)
17. I. I. Grinvald, I. Y. Kalagaev, R. V. Kapustin, in *Density Functional Theory - Recent Advances, New Perspectives and Applications*, D. Grossman-Mitnik, Ed., IntechOpen, London, 2022 (<https://dx.doi.org/10.5772/intechopen.100429>)
18. I. Y. Kalagaev, I. I. Grinvald, *Pure Appl. Chem.* **85** (2012) 135 (<https://dx.doi.org/10.1351/PAC-CON-12-03-06>)
19. S. Grimme, S. Ehrlich, L. Goerigh, *J. Comput. Chem.* **32** (2011) 1456 (<https://dx.doi.org/10.1063/1.3382344>)
20. D. G. A. Smith, L. A. Burns, K. Patkowsky, C. D. Sherrill, *J. Phys. Chem. Lett.* **7** (2016) 2197 (<http://dx.doi.org/10.1021/acs.jpclett.6b00780>)
21. R. Meyer, A. W. Hausera, *J. Chem. Phys.* **152** (2020) 084112 (<https://doi.org/10.1063/1.5144603>)
22. J. M. Mayer, *Acc. Chem. Res.* **44** (2011) 36 (<https://dx.doi.org/10.1021/ar100093z>).



Highly efficient functional materials for modern electrochemical devices

VITALY SMILYK*, YULIIA VOLOSHANOVSKA, VADYM GALAGUZ,
OLEKSANDR IVANENKO and OLHA MEDVEZHYNNSKA

V. I. Vernadsky Institute of General and Inorganic Chemistry of the National Academy of Sciences of Ukraine, 32-34 Acad. Palladina Ave., Kyiv, 03142, Ukraine

(Received 27 July, revised 15 November, accepted 21 November 2022)

Abstract: In order to find new functional materials and materials with improved performance for next-generation electrochemical devices, several new materials for various purposes have been synthesized. In particular, BiVO₄ films were obtained by electrochemical synthesis using interferometric control of film thickness during their deposition. Previously, it was found that the use of thin BiVO₄ films with a thickness of 150 to 400 nm is most effective, where an increase in the quantum yield of photocurrent up to 0.25 at λ of 400 to 450 nm was observed. LiFePO₄ was synthesized in DES medium (low-temperature eutectic solvents): choline chloride-triethylene glycol (ChCl-TEG) and choline chloride-ethylene glycol (ChCl-EG) using NH₄FePO₄ and CH₃COOLi as precursors. It was found that the mode of synthesis of LiFePO₄/C at 973 K for 1 h does not lead to oxidation of LiFePO₄, as evidenced by the values of the ratio Fe²⁺/Fe³⁺ for LiFePO₄ and LiFePO₄/C, which are 2.4 and 2.7, respectively. It was found that the substitution of a part of lead cations (up to 20 mol. %), in the composition of the fluoride-conducting phase Pb_{0.86}Sn_{1.14}F₄, contributes to the increase of its conductivity in the whole temperature range, the higher the concentration of the substituent, to a greater extent. Charge transfer is provided by highly mobile interstitial fluorine anions, the concentration of which increases with the rise of temperature and substituent content.

Keywords: heterostructure; electrodeposition; photoelectrochemical conversion; solid fluoride-ion conductors; quantum yield; photocurrent.

INTRODUCTION

Current trends require quick and high-quality solution to problems of various kinds, and the ever-growing global demand for energy is attracting more and more attention to alternative energy solutions that will remain viable in the long turn. Therefore, one of the actual tasks today is the development and creation of

* Corresponding author. E-mail: VitaliySmilyk@i.ua
<https://doi.org/10.2298/JSC220729082S>

new and promising materials with improved characteristics for alternative sources of energy storage and conversion, sensors and ion-selective electrodes for detection of compounds in gaseous atmospheres, aqueous solutions or melts, environmental monitoring.^{1–12} These include, in particular, solid-state fluoride-ion and lithium-ion current sources, solar energy converters, photoelectrochemical devices for the decomposition of organic compounds.

BiVO_4 is a promising and easy-to-obtain materials for converting solar energy into electricity.^{13–15} Unlike chalcogenides and some oxides, BiVO_4 is a more advantageous material because these compounds contain cadmium and lead. In addition, there is an urgent need to increase the stability of semiconductor sensitizers based on widely used cadmium sulfide and selenide.¹⁶ BiVO_4 has recently attracted increasing attention as a photosensitive material due to the fact that it is a straight-band semiconductor with high absorption of light in the visible region of the solar spectrum.

To create efficient lithium-ion current sources, it is advisable to use nanocrystalline iron (II) phosphate as a cathode material, because, it has high thermal stability and environmental safety.^{17–19} The cathode based on it has a large resource during cycling and a high theoretical capacity. However, obtaining LiFePO_4 , with the necessary properties (single-phase, crystalline, nanoscale, with a conductive coating) is quite a difficult task. Thus, large-scale use of LiFePO_4 as an electrode material is hampered by the disadvantages of commercial synthesis methods, which include a long high-temperature stage of crystal structure formation, which leads to oxidation of iron (II) and recrystallization of LiFePO_4 powder.²⁰ Therefore, it is important to modify existing and develop new methods for obtaining nanocrystalline LiFePO_4 powders with a conductive carbon coating.^{21,22}

Given the depletion of natural resources to increase the production of known energy generating systems (lithium power sources), the development and production of alternative new power sources have not only great scientific and technical, but also social and economic significance. The development of advanced fluoride batteries requires the creation of new electrode and electrolyte materials that have not only a high unipolar conductivity of fluoride in the temperature range close to room temperature, but also a wide window of electrochemical potentials, which provides rapid reversible transfer of fluorides across the interface between the phases of the electrode/electrolyte without destroying their structure. The problem of creating flexible and thin-layer electrode and electrolyte fluoride-conducting materials requires a separate solution.

It follows that the development and creation of new functional materials and materials with improved performance for the next-generation electrochemical devices is an urgent problem today, and its solution should not be scientific only, but also practical and feasible.

EXPERIMENTAL

Electrochemical deposition of BiVO_4 films was performed in galvanostatic mode with a platinum counter electrode. Before electrodeposition of the films, the SnO_2 substrate on the glass was degreased for 5 min in 2M NaOH solution and washed with distilled water. BiVO_4 films were obtained at an anode current of 0.5 mA cm^{-2} from an acidic (HNO_3) electrolyte pH 4.7 based on 10 mmol $\text{Bi}(\text{NO}_3)_3$ and 35 mmol VOSO_4 . The obtained BiVO_4 films were annealed in the air for three hours at 773 K.^{15,23}

The structure of the films was investigated by X-ray phase analysis on a DRON-4 diffractometer. The film thickness was measured by scanning electron microscopy with elemental analysis of the film thickness by oxygen on an EVO 50 XVP microscope. The quantum yield of photoelectrochemical current (η) was measured using an installation that included a monochromator MDR-2 and a xenon lamp DKSSH-500 (Fig. 1). Installation and method for measuring the value of η is described in literature.²⁴ The measurements of electrochemical and photoelectrochemical properties of the films were performed using a potentiostat PGSTAT Elins and the installation shown in Fig. 1. Platinum was used as a counter electrode, films as a working electrode, and Ag/AgCl as a reference electrode; studies of the properties of the films were performed in 0.1 M Na_2SO_4 solution. The stoichiometry of the films was determined using energy-dispersive X-ray spectroscopy based on a scanning electron microscope Philips cpxl 30.

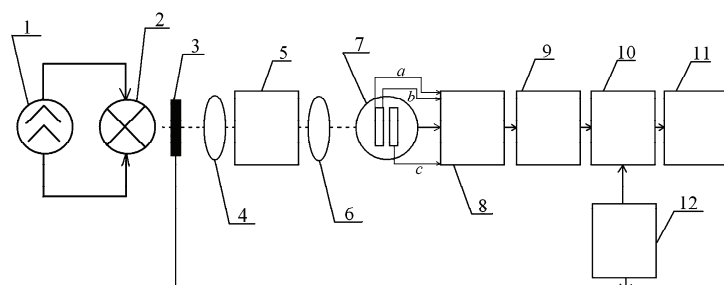


Fig. 1. Scheme for measuring the spectrum of photoelectrochemical current: 1 – power source of the lamp; 2 – xenon lamp of a high pressure of DKSSH-500; 3 – light modulator; 4 – quartz lens; 5 – monochromator MDR-2; 6 – quartz lens; 7 – electrochemical quartz cell (where a – photoelectrode; b – reference electrode; c – counterelectrode); 8 – potentiostat PI-50-1; 9 – amplifier of alternating current U2-8; 10 – phase-sensitive detector UPI-1; 11 – recorder; 12 – alternating current generator.

From X-ray phase analysis of film powder samples (Fig. 2) it was found that after annealing at 773 K in BiVO_4 a monoclinic structure is formed, which is sensitive to visible light at wavelengths of 450–600 nm.²⁵

In order to measure the optical absorption spectra, namely transmission and reflection, it is advisable to use the $\text{BiVO}_4/\text{SnO}_2$ heterostructure, since it is a transparent substrate for which the spectral dependences on the transmission can be measured. This heterostructure is a promising model for use in smart glass. Despite the fact that the adhesion to the substrate in this case is slightly worse than in the same heterostructure based on $\text{BiVO}_4/\text{TiO}_2$, but the use of $\text{BiVO}_4/\text{SnO}_2$ is much higher than in $\text{BiVO}_4/\text{TiO}_2$.

According to the results of energy dispersion analysis (Fig. 3) of the spectrum of bismuth vanadate, it was found that the content of stannous dioxide is dominant with the inclusion of bismuth in vanadium.

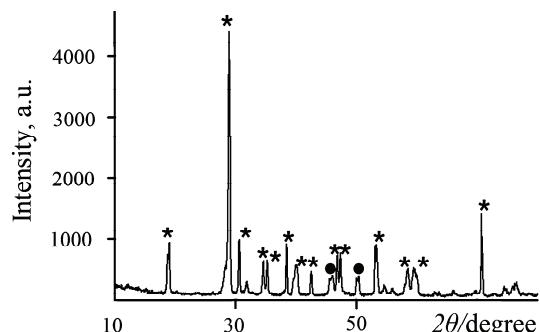


Fig. 2. Diffraction pattern of powder from BiVO_4 films treated at a temperature of $500\text{ }^\circ\text{C}$: * - structure of monoclinic BiVO_4 , ● - tetragonal BiVO_4 .

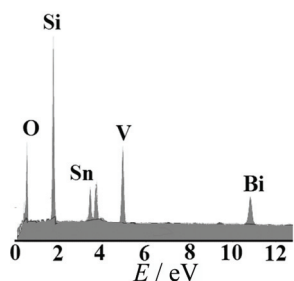


Fig. 3. EDAX spectrum of $\text{BiVO}_4/\text{SnO}_2$ electrode elements.

Polycrystalline samples based on lead and stannum fluorides were synthesized by the fusion method. Pre-dried and ground samples of starting fluorides were fused in a platinum crucible in an argon atmosphere in the range of $773\text{--}823\text{ K}$ and kept at this temperature for 15 min and cooled in the oven off mode (cooling rate $3\text{--}5\text{ }^\circ\text{C}/\text{min}$).

The electrical conductivity properties of the synthesized samples of fluoride-conducting phases were investigated by the electrochemical impedance spectroscopy using a two-electrode circuit using an autochemical module Autolab (Ekochemie) and a frequency response analyzer (FRA) in the frequency range of $10^1\text{--}10^6\text{ Hz}$ at the signal frequency. The pressed polycrystalline cylindrical samples with a diameter of 8 mm and a thickness of $2.0\text{--}3.0\text{ mm}$ were used for research. Platinum plates were used as current leads to the samples. The measurements were performed in an argon atmosphere in the range of $298\text{--}773\text{ K}$ after thermostating in the cooling mode. To level the contribution of the porosity of the samples, the tablets were made in the same molds from fine fractions with a particle size of not more than $60\text{ }\mu\text{m}$ at a pressure of 150 at. The specific conductivity was calculated as:

$$\sigma = (l/s)R \quad (1)$$

where l is the thickness of the cylindrical sample, s is the contact area, R is the active resistance.

Lithium iron phosphate LiFePO_4 was obtained by thermal heating in choline chloride and DEG, which was performed on a magnetic stirrer with a thermostat and the ability to heat up to 623 K . A mixture of choline chloride with ethylene glycol or choline chloride with triethylene glycol (1:2) was placed in a heat-resistant Simax conical flask under reflux/with reflux condenser and kept for 1 h at 353 K and 300 rpm. Then ammonium iron (II) phosphate and lithium precursor were added and heated to $473\text{--}573\text{ K}$ and kept for 1–4 h. After synthesis, the precipitate was washed in distilled water and isopropyl alcohol. The obtained powder was dried for 2 h at 393 K .

The method of galvanostatic cycling (cyclic charge–discharge) was used to obtain information about the amount of electric charge stored or given per unit mass of material, and the stability of this parameter during cycling. The current was determined according to the mass of the cathode and set with a resolution of $0.1\text{ }\mu\text{A}$, the accuracy of maintaining a given current was $0.5\text{ }\mu\text{A}$. The potential limits were set according to the requirement of the experiment and the capabilities of the electrolyte. The specific capacity was calculated as the product of the set current for the operating time divided by the mass of pure cathode material LiFePO₄ in the working electrode. The maximum relative error of determination was 4 %.

RESULTS AND DISCUSSION

Surface studies and spectral dependences of BiVO₄

To increase the efficiency of bismuth vanadate, it is necessary to know such parameters as current density and crystallite size. From the study of BiVO₄ thin films by scanning electron microscopy (Fig. 4) it was found that the obtained films consist of plate crystals with a plate thickness of about 20 nm. From the photomicrographs (Fig. 4b) it was determined that the size of the crystals depends on the current density of the electrodeposition BiVO₄. Fig. 4 shows that an increase in the electrodeposition current leads to an increase in the size of the plate crystals from 60–100 nm to 300–500 nm and a decrease in the developed surface of the film. Analysis of the obtained data leads to the conclusion that the control of such parameters of electrodeposition of BiVO₄ films as current density and, to some extent, the concentration of electrolyte components, promotes the formation of nanoscale crystallites and increase the surface area. As will be shown below (Fig. 5), the quantum yield of the photocurrent directly depends on the film thickness.

The band gap/forbidden zone of a semiconductor material such as BiVO₄ with direct transitions can be estimated using the Taus equation, where the extrapolation to x -axis of the linear region of the graph $(ahv)^2$ related to the electron

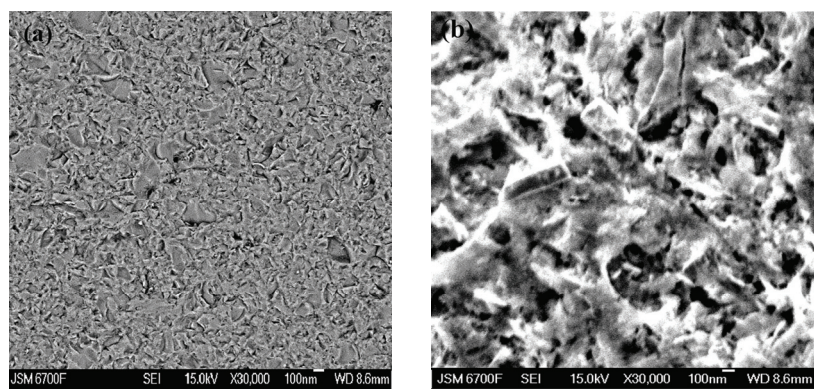


Fig. 4. SEM of the samples of films with a thickness of 140 nm (a) and 1 μm (b), obtained by electrodeposition for 30 min at a current density of 0.5 (a) and 3 mA cm^{-2} (b) with subsequent annealing at 773 K.

energy in eV gives a direct band gap.²⁶ The optical band gap (E_g), which was previously estimated, is 2.5–2.3 eV, which corresponds to a value of 2.4 eV, which is given in the literature for the monoclinic scheelite BiVO₄.^{26–28}

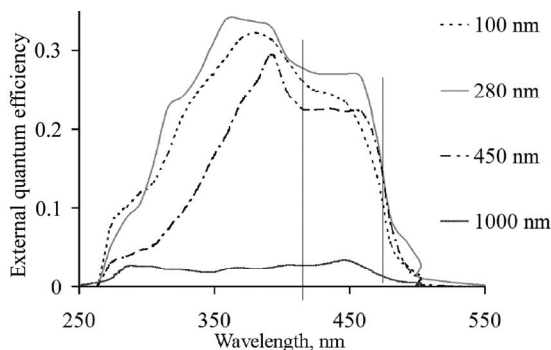


Fig. 5. Spectra of quantum yield of photocurrent of SnO₂/BiVO₄ films of different thickness in a solution of 0.1 M Na₂SO₄ at a potential of 0.8 V vs. Ag/AgCl.

The studies of the effect of BiVO₄ film thickness on the quantum yield of photocurrent (Fig. 5) showed that 0.5–1 μm thick films have a lower quantum yield compared to 80–150 nm thick films. This fact can be explained by the physical properties of polycrystalline BiVO₄ films, namely their low conductivity.^{29,30} In addition as can be seen from the spectra of Fig. 5, on thin films, a greater contribution to the photocurrent gives visible light compared to films thicker than 500 nm, where the area of maximum quantum yield of the photocurrent falls on the near-ultraviolet radiation.

In BiVO₄ films³¹ high efficiency is observed at small thicknesses of ~100 nm (Fig. 5). The increase in thickness leads to an increase in energy costs for recombination losses and an increase in their electrical resistance and, as a result, the efficiency of charge transfer decreases.³¹ Fig. 5 shows that the spectral characteristics with the increasing thickness narrow and decrease in intensity both in UV and in the visible parts of the spectrum. It can be noted that the effective region of the maximum quantum yield of photocurrent in the visible region is observed at film thicknesses of 150–450 nm. Thus, on thin films of 40–200 nm, as can be seen from the spectra, a greater contribution to the photocurrent is given by visible light, compared to films thicker than 500 nm, where the region of maximum quantum photocurrent yield falls on near UV radiation. In addition, at thicknesses of ~100 nm, the formation of a SnO₂/BiVO₄ heterojunction is observed, which is expressed by an increase in the efficiency of the spectral characteristic of the quantum photocurrent yield in the SnO₂ and BiVO₄ light absorption regions (Fig. 5). SnO₂ films with a thickness of 250–300 nm have a high electronic conductivity and, having a band gap of 3.1 eV, provide the appearance of photocurrent under UV illumination due to the transmission of light by thin BiVO₄ films.

Summarizing the research, we can conclude that for effective light absorption by BiVO₄ films it is necessary to grow nanosized crystallites in a matrix of oxides or other vanadates with high electronic conductivity, which will allow you to select the required film thickness for a higher quantum yield of bismuth vanadate fluocurrent and improve the efficiency of such material.

Solid fluoride-conducting electrolytes of composition Pb_{0.86-x}M_xSn_{1.14}F_{4±x} (M = Li, Na, K, Rb, Ba, Nd, Sm)

The X-ray diffraction method established that in the system PbF₂–SnF₂ at a ratio of the initial components of 43 mol. % PbF₂ and 57 mol. % SnF₂ forms a single-phase solid solution with the structure β-PbSnF₄, the formula of which can be represented as Pb_{0.86}Sn_{1.14}F₄.³² The electrical conductivity of this phase at $T \approx 390$ K is an order of magnitude higher compared to β-PbSnF₄ (σ_{373} of 2.9 and 0.902 mS cm⁻¹, respectively). Therefore, in order to search for new substances with improved fluoride-ionic conductivity characteristics, a number of new fluoride-conducting phases based on Pb_{0.86}Sn_{1.14}F₄ compound with β-PbSnF₄ structure were synthesized by replacing some Pb²⁺ with fluorides of metals of different oxidation states (M = Li, Na, K, Rb, Ba, Nd, Sm).

With partial substitution of Pb²⁺ by M⁺, the samples of solid solutions K_xPb_{0.86-x}Sn_{1.14}F_{4-x} ($x = 0.03; 0.05; 0.07; 0.10; 0.15$) and Rb_xPb_{0.86-x}Sn_{1.14}F_{4-x} were synthesized ($0 < x \leq 0.2$) with crystal lattice of tetragonal syngony of the β-PbSnF₄ isostructure (Fig. 6). The substitution of lithium ions leads to the simultaneous formation of two phases: tetragonal (β) and monoclinic (α) modification of PbSnF₄. When Pb²⁺ is replaced by Na⁺, the reflections are recorded on

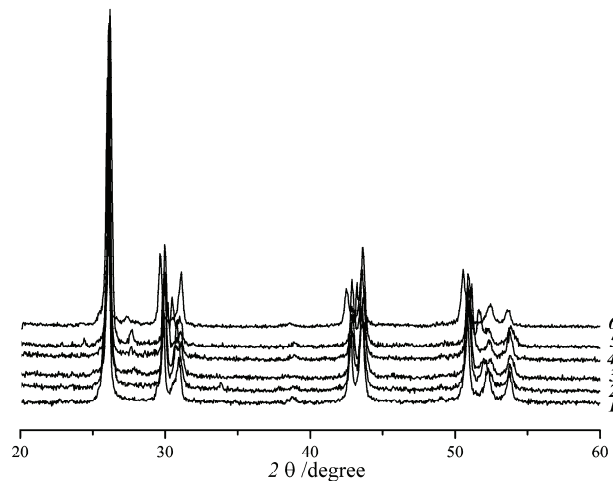


Fig. 6. X-ray diffraction patterns of the synthesized samples: 1 – Pb_{0.86}Sn_{1.14}F₄; 2 – Rb_{0.05}Pb_{0.81}Sn_{1.14}F_{3.95}; 3 – K_{0.05}Pb_{0.81}Sn_{1.14}F_{3.95}; 4 – Pb_{0.81}Nb_{0.05}Sn_{1.14}F_{4.05}; 5 – Pb_{0.76}Sn_{1.14}F_{4.1}; 6 – Pb_{0.731}Ba_{0.129}Sn_{1.14}F₄.

diffractograms even at small amounts of x (up to 3 mol. %), except for the main phase, corresponding to the additional phase of NaSn_2F_5 , the formation of which, according to literature,³³ leads to a deterioration of the electrical conductivity of the samples.

It was established by the X-ray diffraction method that the partial substitution of Pb^{2+} in the compound $\text{Pb}_{0.86}\text{Sn}_{1.14}\text{F}_4$ by Ba^{2+} forms an uninterrupted series of solid solutions $(\text{Pb}_{1-x}\text{Ba}_x)_{0.86}\text{Sn}_{1.14}\text{F}_4$, where x becomes $0 \leq x \leq 1.0$. The symmetry of the crystal lattice of the synthesized phases in the concentration range $0 \leq x \leq 0.50$ corresponds to the structural type $\beta\text{-PbSnF}_4$ (spatial group $P4/nmm$), and with increasing barium fluoride content their crystal lattice is readjusted and approaches the structural type BaSnF_4 , while preserving the spatial group.

By the X-ray diffraction method, it was found that single-phase solid solutions of the composition $\text{Pb}_{0.86-x}\text{R}_x\text{Sn}_{1.14}\text{F}_{4+x}$ ($\text{R} = \text{Nd}, \text{Sm}$) is formed at values of $x \leq 0.15$. When more than 15 mol.% of a rare earth element trifluoride is combined with the structure of the starting compound and the reflexes corresponding to RF_3 are registered on the diffractograms in addition to the main phase, the presence of which in turn can impair the conductive properties of the compounds.

The electrically conductive properties of the synthesized samples of fluoride-conducting phases $\text{M}_x\text{Pb}_{0.86-x}\text{Sn}_{1.14}\text{F}_{4-x}$ ($\text{M} = \text{Li}, \text{K}, \text{Na}, \text{Rb}$) were investigated by the electrochemical impedance spectroscopy. On the impedance diagrams of all studied samples in the high frequency region, only one deformed semicircle is registered, which in the transition to the low-frequency region, and it is transformed into a rectilinear dependence (Fig. 7), which indicates the polarization of the electrolyte/blocking electrode interface.³⁴ In Fig. 7 the typical impedance hodographs on the example of a solid solution $\text{Rb}_x\text{Pb}_{0.86-x}\text{Sn}_{1.14}\text{F}_{4-x}$ is shown.

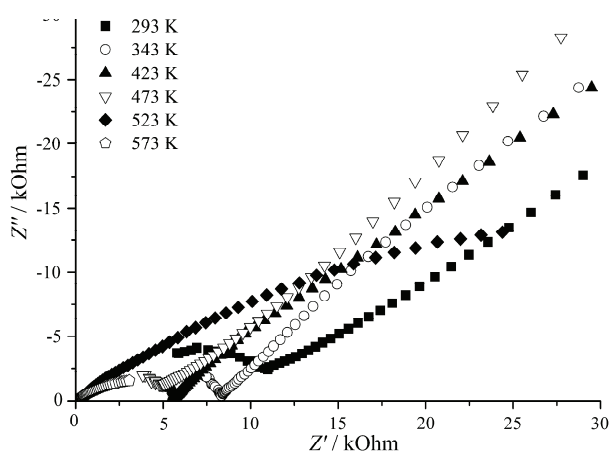


Fig. 7. Impedance diagrams of solid solution $\text{Rb}_{0.1}\text{Pb}_{0.76}\text{Sn}_{1.14}\text{F}_{3.9}$ at different temperatures in Nyquist coordinates.

As the temperature increases, the radius of the deformed semicircles decreases (Fig. 7), and the semicircles shift to the region of higher frequencies. At sufficiently high temperatures, the conductivity of the sample can be estimated by analyzing the dependence of the actual component of the complex conductivity on the frequency in Bode coordinates or by the bridge method at frequencies that exclude the influence of blocking electrodes and frequency-dependent impedance component.^{34,35} This nature of the change in impedance diagrams is typical for disordered ion-conducting electrolytes with relaxation processes due to the structural and energy inequivalence of charge carriers – fluorides.³⁶

The shape of the obtained impedance diagrams indicates the absence of a significant contribution of the conductivity of the crystallite surfaces of the synthesized phases in their total bulk conductivity. This is confirmed by the calculated values of the capacitance of the complex conductivity of the samples at frequencies f_m , which correspond to the maximum values of Z'' of the deformed semicircles. Their value is of the order of 10–40 pF and is much smaller than the conductivity capacity of the crystallite surface 1–100 nF.³⁶

Temperature dependencies of fluoride conductivity were studied in the frequency range that is not affected by polarization and relaxation effects. It was found that a slight substitution (up to 3.0 mol. %) of Pb^{2+} on Rb^+ at $T < 500$ K reduces the conductivity of the obtained samples by an order of magnitude, and the nature of its temperature dependence is similar to the temperature dependence of the conductivity of the $\beta\text{-PbSnF}_4$ sample. When replacing 5 mol. % of Pb^{2+} on Rb^+ fluoride-ion the conductivity at $T > 450$ K becomes higher than the conductivity of the initial sample $\text{Pb}_{0.86}\text{Sn}_{1.14}\text{F}_4$, and at temperatures below 450 K – an order of magnitude lower. When lead ions are replaced by rubidium over 0.1 mole fraction, the electrical conductivity in the entire temperature range increases, reaching the maximum values at $x \geq 0.15$. For samples with $x \geq 0.2$, the electrical conductivity practically does not change (Table I). The highest value of conductivity and the lowest activation energy possesses the sample $\text{Rb}_{0.3}\text{Pb}_{0.56}\text{Sn}_{1.14}\text{F}_{3.7}$ ($\sigma_{573} = 0.41 \text{ S cm}^{-1}$, $E_a = 0.16 \text{ eV}$).

Slight substitution (3.0 mol. %) of Pb^{2+} on K^+ in the structure of $\text{Pb}_{0.86}\text{Sn}_{1.14}\text{F}_4$ causes an increase in electrical conductivity: at 600 K its value is 0.38 S cm^{-1} , and at 330 K – 0.01 S cm^{-1} , which is an order of magnitude higher compared to the original $\text{Pb}_{0.86}\text{Sn}_{1.14}\text{F}_4$ and two orders of magnitude higher compared to pure $\beta\text{-PbSnF}_4$. The activation energy of the electrical conductivity in the high-temperature region does not change (0.08 eV for the original $\text{Pb}_{0.86}\text{Sn}_{1.14}\text{F}_4$ and 0.09 eV for the solid solution $\text{Pb}_{0.83}\text{K}_{0.03}\text{Sn}_{1.14}\text{F}_{3.97}$), and the total electrical conductivity increases due to vacancies in the anionic lattice. The electrical conductivity of the synthesized samples with the content of potassium ions, which replace Pb^{2+} , greater than 0.03 mole fraction in the whole temperature range decreases. In contrast to compounds with a purely internodal conduct-

ion mechanism,³⁴ the activation energy for solid solutions $K_xPb_{0.86-x}Sn_{1.14}F_{4-x}$ at $T > 450$ K increases with the rise of potassium fluoride content. This may be due to the fact that the movement of fluoride ions between vacancies requires more energy than the movement in the interstitial spaces.

TABLE I. Electrical conductivity parameters of the starting compound $Pb_{0.86}Sn_{1.14}F_4$ and solid solutions $Pb_{0.86-x}M_xSn_{1.14}F_{4\pm x}$ ($M = Li, Na, K, Rb, Ba, Nd, Sm$)

Sample	$\Delta E_a / \text{eV}$	$\sigma / \text{S cm}^{-1}$	T / K
$Pb_{0.86}Sn_{1.14}F_4$	0.28	0.0029	373
	0.18	0.0175	473
	0.1	0.0241	573
$K_{0.03}Pb_{0.83}Sn_{1.14}F_{3.97}$	0.49	0.1200	373
	0.19	0.2870	473
	0.09	0.3730	573
$Rb_{0.2}Pb_{0.66}Sn_{1.14}F_{3.80}$	0.51	0.0772	373
	0.15	0.3400	573
$Pb_{0.43}Ba_{0.43}Sn_{1.14}F_4$	0.11	0.1200	373
	0.11	0.3300	573
$Pb_{0.76}Sm_{0.10}Sn_{1.14}F_{4.10}$	0.36	0.0022	373
	0.26	0.0736	573
$Pb_{0.73}Sm_{0.13}Sn_{1.14}F_{4.13}$	0.31	0.0028	373
	0.43	0.0927	573
$Pb_{0.69}Nd_{0.17}Sn_{1.14}F_{4.17}$	0.1	0.0368	373
	0.34	0.2100	473
	0.18	0.3300	573

The slight substitution ($x = 0.03$) of Pb^{2+} by K^+ in the $Pb_{0.86}Sn_{1.14}F_4$ structure causes an increase in electrical conductivity: at 600 K, its value is 0.38 S cm^{-1} and at 330 K is 0.01 S cm^{-1} , which is an order of magnitude higher compared with original $Pb_{0.86}Sn_{1.14}F_4$ and two orders of magnitude higher compared with pure β - $PbSnF_4$. In this case, the conductivity activation energy in the high-temperature region does not practically change (0.08 eV for original $Pb_{0.86}Sn_{1.14}F_4$ and 0.09 eV for $Pb_{0.83}K_{0.03}Sn_{1.14}F_{3.97}$ solid solution), and the total electrical conductivity increases owing to the appearance of vacancies in the anion sublattice. The electrical conductivity of the synthesized samples with the percentage of potassium ions replacing Pb^{2+} of over $x = 0.03$ decreases over the entire temperature range. Unlike the compounds with purely interstitial conduction mechanism, the activation energy for $K_xPb_{0.86-x}Sn_{1.14}F_{4-x}$ solid solutions at $T > 450$ K increases with potassium and fluoride content.³⁸ This may be due to the fact that the motion of fluoride ions between vacant positions requires a higher consumption of energy than that in interstitial spaces.

It was found that the substitution of lead ions by Ba^{2+} in the compound $Pb_{0.86}Sn_{1.14}F_4$ at $x \leq 0.30$ leads to a decrease in the electrical conductivity of the obtained samples in comparison with the original compound $Pb_{0.86}Sn_{1.14}F_4$. The

substitution of lead ions at $0.15 \leq x \leq 0.30$ allows a slight increase of the electrical conductivity of the obtained samples only at temperatures above 500 K, compared to the original compound $\text{Pb}_{0.86}\text{Sn}_{1.14}\text{F}_4$. The nature of the temperature dependences of the electrical conductivity is similar to the compound $\beta\text{-PbSnF}_4$.

Subsequent substitution of lead ions in the compound $\text{Pb}_{0.86}\text{Sn}_{1.14}\text{F}_4$ at $x \leq 0.30$ leads to a decrease in the electrical conductivity of the obtained samples in comparison with the original compound $\text{Pb}_{0.86}\text{Sn}_{1.14}\text{F}_4$. Further increase in the content of barium difluoride ($0.30 \leq x \leq 0.55$) increases the electrical conductivity of the synthesized samples in the entire temperature range. The sample with the highest electrical conductivity and the lowest activation energy of ionic conductivity is $\text{Pb}_{0.43}\text{Ba}_{0.43}\text{Sn}_{1.14}\text{F}_4$ ($\sigma = 0.12 \text{ S cm}^{-1}$, $E_a = 0.11 \text{ eV}$ at 373 K). In this case, the replacement of half of the lead ions by barium ions in the compound $\text{Pb}_{0.86}\text{Sn}_{1.14}\text{F}_4$ allows the electrical conductivity to increase more than 100 times compared to the conductivity of the initial phase of $\beta\text{-PbSnF}_4$.

The introduction to 8 mol. % SmF_3 in the initial structure $\text{Pb}_{0.86}\text{Sn}_{1.14}\text{F}_4$ helps to reduce the electrical conductivity of the obtained samples in the entire temperature range compared to $\text{Pb}_{0.86}\text{Sn}_{1.14}\text{F}_4$, bringing them closer to the values of electrical conductivity of $\beta\text{-PbSnF}_4$. However, at temperatures above 520 K the electrical conductivity of solid solutions is almost three times higher than the value for $\beta\text{-PbSnF}_4$ ($\sigma_{553} = 0.054$ and 0.017 S cm^{-1} , respectively) and twice higher than the electrical conductivity of the original compound $\text{Pb}_{0.86}\text{Sn}_{1.14}\text{F}_4$ (σ_{553} of 0.054 and 0.023 S cm^{-1} , respectively). A further increase in the concentration of Sm^{3+} in the structure of the initial fluoride $\text{Pb}_{0.86}\text{Sn}_{1.14}\text{F}_4$ leads to an increase in electrical conductivity in the entire temperature range. The most significant effect of the heterovalent substituent is manifested at temperatures above 420 K. For example, the value of electrical conductivity for solid solutions $\text{Pb}_{0.76}\text{Sm}_{0.10}\text{Sn}_{1.14}\text{F}_{4.10}$ and $\text{Pb}_{0.73}\text{Sm}_{0.13}\text{Sn}_{1.14}\text{F}_{4.13}$ at $T = 500 \text{ K}$ is 0.038 and 0.046 S cm^{-1} , respectively, while for the compound $\text{Pb}_{0.86}\text{Sn}_{1.14}\text{F}_4$ it is 0.02 S cm^{-1} .

Slight substitution (3.0 mol. %) of Pb^{2+} by Nd^{3+} in the structure of $\text{Pb}_{0.86}\text{Sn}_{1.14}\text{F}_4$ causes an increase in electrical conductivity at $T > 530 \text{ K}$ (68.8 mS cm^{-1} compared with 24.1 mS cm^{-1} for the initial compounds $\text{Pb}_{0.86}\text{Sn}_{1.14}\text{F}_4$), and below this temperature, on the contrary, slightly reduces the electrical conductivity, approaching the values of $\beta\text{-PbSnF}_4$. The activation energy of the conductivity increases in the whole temperature range. With a further increase in the content of Nd^{3+} the fluoride-ion conductivity of the samples increases throughout the temperature range. It should be noted that samples with a content of 10–15 mol. % NdF_3 at $T > 500 \text{ K}$ have comparable values of electrical conductivity, and below this temperature, it increases with the substituent content. The compound $\text{Pb}_{0.69}\text{Nd}_{0.17}\text{Sn}_{1.14}\text{F}_{4.17}$ has the highest values of electrical conductivity and the lowest activation energy. The subsequent introduction of neodymium trifluoride (more than 18 mol. %) into the $\text{Pb}_{0.86}\text{Sn}_{1.14}\text{F}_4$ structure leads

to a decrease in the electrical conductivity of the samples, which can be explained by the formation of an additional NdF_3 phase, as evidenced by the results of X-ray phase analysis.

Thus, it is found that the substitution in the composition of the fluoride-conducting phase $\text{Pb}_{0.86}\text{Sn}_{1.14}\text{F}_4$ part of the cations of lead (up to 20 mol.%) increases its conductivity in the entire temperature range, and to a greater extent, the higher the concentration of the substituent. The highest conductivity and the lowest activation energy have samples of the composition $\text{Pb}_{0.69}\text{Nd}_{0.17}\text{Sn}_{1.14}\text{F}_{4.17}$ ($\sigma_{373} = 0.0368 \text{ S cm}^{-1}$), $\text{Pb}_{0.76}\text{Sm}_{0.10}\text{Sn}_{1.14}\text{F}_{4.10}$ and $\text{Pb}_{0.73}\text{Sm}_{0.13}\text{Sn}_{1.14}\text{F}_{4.13}$ (σ_{500} of 0.038 and 0.046 S cm^{-1} , respectively), $\text{K}_{0.03}\text{Pb}_{0.83}\text{Sn}_{1.14}\text{F}_{3.97}$ ($\sigma_{600} = 0.38 \text{ S cm}^{-1}$, $\sigma_{330} = 0.01 \text{ S cm}^{-1}$), $\text{Rb}_{0.2}\text{Pb}_{0.63}\text{Sn}_{1.14}\text{F}_{3.8}$ (σ_{573} in range 0.34–0.41 S cm^{-1} , $E_a = 0.16 \text{ eV}$ and σ_{373} in range 53.4–81.6 mS cm^{-1} , $E_a = 0.48$ to 0.51 eV in accordance). The transfer numbers for fluorine anions are not less than 0.99 and practically do not depend on the concentration of the substituent.

Lithium iron phosphate as a promising cathode material

Recently, much attention has been paid to systems based on low-temperature deep eutectic solvents (DES), which differ from other ionic liquids. In recent years, DES has begun to be considered as a design solvent for the development of nanomaterials with a well-defined morphology, including nanoparticles with a controlled structure.

It should be noted that of particular interest for the synthesis of cathode materials is the DES composition: choline chloride–ethylene glycol (ChCl–EG), choline chloride–diethylene glycol (ChCl–DEG), choline chloride–triethylene glycol (ChCl–TEG). This system has all the advantages of solvothermal synthesis in ethylene glycol, diethylene glycol, triethylene glycol, which are characterized by high boiling points 473–573 K, the ability to dissolve polar inorganic salts, to form chelated complexes with transition metals. They also provide a reducing reaction medium. Due to these unique physicochemical properties, these glycols can affect the kinetics of the chemical reaction and the morphology of the precipitates obtained in the synthesis of nanomaterials. They are not only solvents and reducing agents, but also play the role of a template for directional growth and self-assembly of hierarchical structures in the formation of nanocrystals. At the same time, DES is characterized by a number of special properties that distinguish them from other ionic liquids and polyols: they are cheap and readily available, non-toxic, and extremely easy to prepare. In addition, DES based on ChCl and the above-mentioned polyhydric alcohols readily dissolve oxides and salts of many metals that are insoluble or sparingly soluble in other ionic liquids.

To obtain such compounds, in particular LiFePO_4 , the method of synthesis by ion exchange reaction was used by using $\text{NH}_4\text{FePO}_4 \cdot \text{H}_2\text{O}$ as a base precursor. The similarity of the crystal structure of $\text{NH}_4\text{FePO}_4 \cdot \text{H}_2\text{O}$ and LiFePO_4 allows

the synthesis of LiFePO₄ by replacing the NH₄⁺ in NH₄FePO₄ with the Li⁺ from the lithium salt.

Synthesis of LiFePO₄ with thermal heating in choline chloride and DEG was performed on a magnetic stirrer with a thermostat and the ability to heat up to 623 K. A mixture of choline chloride and ethylene glycol or choline chloride and triethylene glycol (1:2) was placed in a heat resistant Simax conical flask under reflux condenser and kept for 1 h at 353 K and 300 rpm. Then ammonium iron (II) phosphate was added, and the lithium precursor was heated to 473–573 K and kept for 1 to 4 h. Upon completion of the synthesis, the precipitate was washed in distilled water and isopropyl alcohol. The resulting powder was dried for 2 h at a temperature of 393 K. The precipitation of LiFePO₄ occurs with the formation and evaporation of gaseous reaction products: NH₃, CH₃COOH and H₂O. The ion exchange reaction occurs by replacing the NH₄⁺ in NH₄FePO₄·H₂O with a Li⁺ from lithium acetate. Compared with the usual solid-phase reaction, the ion exchange reaction in EG–choline chloride/TEG–choline chloride does not require high temperatures and occurs in a short time.

At a temperature of 473 K in choline chloride–ethylene glycol and a synthesis time of 1 to 4 h, the precipitates obtained are amorphous in nature with a low content of crystalline phase, as evidenced by radiographs with a characteristic halo for amorphous samples (Fig. 8b). The powder synthesized in the environment of choline chloride–triethylene glycol at a temperature of 573 K is characterized by sufficient crystallinity after the first hour of synthesis (Fig. 8a). In the obtained samples there are no impurities (within the sensitivity of the method), all reflexes are consistent with the standard JCPDSNo: 00-40-1499. The excess of precursor lithium in the reaction medium does not affect the composition of the final product.

To synthesize the composite cathode material with carbon, LiFePO₄ powders were wetted with glucose solution, dried at 323 K, and placed in a quartz reactor, where it was annealed at 973 K. under argon for 1 h. The carbon content in the composite was determined using gravimetric methods. To find out the theoretical content of carbon formed after the carbonization of glucose or malic acid during the production of the composite, the samples of organic components

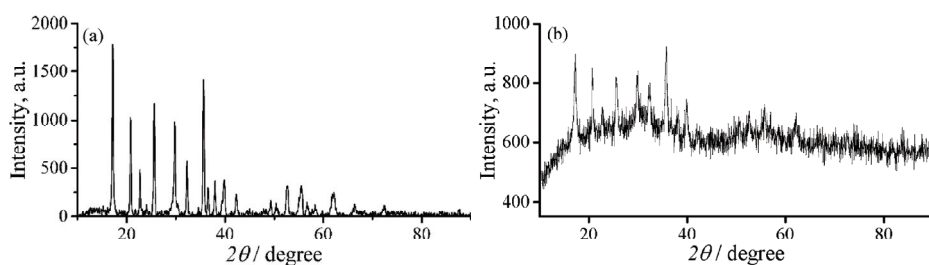


Fig. 8. XRD spectra of LiFePO₄ synthesized in ChCl-TEG (A) ChCl-EG (B).

were subjected to heat under conditions corresponding to the annealing regime of LiFePO₄. Based on the obtained results, the masses of glucose or malic acid were calculated, which were added to the synthesized powder for further annealing and obtaining a composite. With the introduction of the organic component with the calculation of the formation of 10 wt. % C after annealing, in practice the results range from 9.8 to 10.1 %, which is due to losses and inaccuracies of measurement during the experiment.

X-ray photoelectron spectroscopy (XPS) was used to study the surface of the synthesized cathode material – LiFePO₄ and carbon composite based on it – LiFePO₄/C. A study of Fe 2p_{3/2} spectra of LiFePO₄ and LiFePO₄/C composite obtained at 973 K for 1 h was performed.³⁸ The spectra of Fe 2p_{3/2} levels are formed by components in the region 709.6–711.3 eV, which belong to Fe²⁺ states of Fe, and components in the region 712.6 to 714.5 eV to Fe³⁺ states in LiFePO₄.

Galvanostatic charge/discharge characteristics of the electrode based on LiFePO₄ were taken using a 1 M electrolyte based on LiPF₆ in EC:DMC (1:1) in a cell type “coin cell”. Fig. 9a shows the second and third cycles of charge/discharge. The material capacity for the second cycle is about 130 mAh g⁻¹, and for the 3rd ~120 mAh g⁻¹. Continuation of the cycle did not occur due to violation of the integrity of the cell and the probable decomposition of the electrolyte and the formation of dendrites.

For the material LiFePO₄/C with a carbon content of ~10 %, the charge/discharge characteristics were obtained in a T-shaped cell with an electrolyte composition: 0.6 M solution of bis (oxalate) lithium borate (LiBOB) in an equimolar mixture of EC–DMC. The capacity of the material in terms of the content of pure LiFePO₄ in the cathode mass is about 100 mAh g⁻¹ for the best cycle at a current of 0.1C (Fig. 9b). It was not possible to carry out a large number of cycles, which is explained by imperfect assembly conditions and insufficiently clean materials, first of all by the quality of the electrolyte and the “wear” of the cell, which does not ensure tightness. Also, long-term annealing of the material leads to a slight

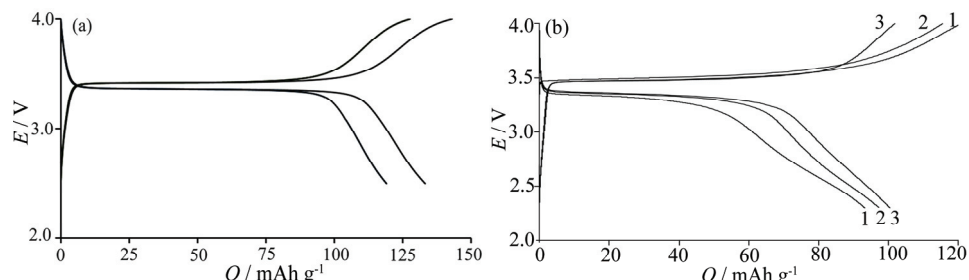


Fig. 9. Charge/discharge characteristics of the electrode based on LiFePO₄/C; a) in a 1 M solution of LiPF₆ in EC: DMC (1:1) at a current of 0.1C; b) in a 0.6 M solution of LiBOB in EC: DMC (1:1) at a current of 0.1C for three cycles.

oxidation of the powder surface, which could lead to the formation of unwanted impurities and slightly underestimate the electrochemical parameters of the material in terms of the content of LiFePO₄ in the cathode mass.

It should be noted that the functional characteristics of LiFePO₄ depend significantly on the materials and assembly methods of the electrochemical cell. Unfortunately, our material and technical conditions for testing electrode materials are imperfect. Therefore, we obtain underestimated results, which is confirmed by the results of testing commercial LiFePO₄ under our assembly conditions.³⁷ For commercial material (LiFePO₄/C "Life Power P1" Phostech Lithium inc., Canada) the capacity is 140 mAh g⁻¹, but under the conditions we worked in, it was 120 mAh g⁻¹ when using a coin cell.³⁷ For comparison, the best material synthesized by us had capacity indicators of ~130 mAh g⁻¹.

CONCLUSION

Monoclinic BiVO₄ films were obtained by electrochemical synthesis. The composition of the film material was determined by X-ray diffraction and EDAX. It has been established that for the efficient absorption of light by BiVO₄ films, it is necessary to grow nanosized crystallites in a matrix of oxides or other vanadates with high electronic conductivity. A study of the effect of the thickness of BiVO₄ films obtained by electrochemical deposition on the quantum yield of photocurrent showed that for the most effective increase in photocurrent from 0.25 such photo anodes, thin BiVO₄ films of 150–400 nm should be used.

It was confirmed that the substitution of part of lead cations (up to 20 mol. %) in the composition of the fluoride-conducting phase Pb_{0.86}Sn_{1.14}F₄ helps to increase its conductivity in the entire temperature range, and the greater the concentration of the substitute, to a greater extent. The transfer numbers for fluorine anions are not lower than 0.99 and practically do not depend on the concentration of the substituent.

Composite materials with carbon based on lithium ferrum (II) phosphate (LiFePO₄/C) were obtained in the environment of DES (low-temperature eutectic solvents): choline chloride-triethylene glycol (ChCl–TEG) and choline chloride–ethylene glycol (ChCl–EG), using NH₄FePO₄ and CH₃COOLi as precursors. Electrochemical studies of the obtained materials were carried out using a t-cell of our own production and a "coin cell" type cell with electrolytes based on commercial LiPF₆ and self-synthesized LiBOV. The best results (capacity based on pure LiFePO₄ is ~130 mAh g⁻¹ for a current of 0.1C) were obtained for powders synthesized in ChCl–TEG and annealed for 1 h at 973 K with a carbon content of ~10 %. Powder (LiFePO₄/C) with a carbon content of ~10 % synthesized in an environment of ethylene glycol and choline chloride with subsequent annealing for 10–12 h at 973 K in an argon atmosphere showed worse results: in terms of LiFePO₄, the capacity was ~100 mAh g⁻¹ for a current of 0.1C.

И З В О Д

ВИСОКО ЕФИКАСНИ ФУНКЦИОНАЛНИ МАТЕРИЈАЛИ ЗА САВРЕМЕНЕ
ЕЛЕКТРОХЕМИЈСКЕ УРЕЂАЈЕ

VITALY SMILYK, YULIA VOLOSHANOVSKA, VADYM GALAGUZ, OLEKSANDR IVANENKO
и OLHA MEDVEZHYNNSKA

*V. I. Vernadsky Institute of General and Inorganic Chemistry of the National Academy of Sciences of Ukraine,
32-34 Acad. Palladina Ave., Kyiv, 03142, Ukraine*

У потрази за новим функционалним материјалима и материјалима побољшаних перформанси за електрохемијске уређаје нове генерације, синтетисано је неколико нових материјала. Конкретно, филмови BiVO_4 су добијени електрохемијском синтезом, при чему је коришћена интерферометријска контрола дебљине филма током талочења. Претходно је нађено да је најефикасније коришћење танких филмова BiVO_4 дебљине 150–400 nm, код којих је запажен пораст квантног приноса фотострује до 0,25 на таласној дужини 400–450 nm. LiFePO_4 је синтетисан из нискотемпературнеeutектичке смеше холин-хлорид-тристилен-гликол (ChCl-TEG) и холин-хлорид-стилен-гликол (ChCl-EG) коришћењем NH_4FePO_4 and CH_3COOLi као прекурсора. Показано је да примењени режим синтезе LiFePO_4/C на 973 K током 1 h не доводи до оксидације LiFePO_4 , јер је однос $\text{Fe}^{2+}/\text{Fe}^{3+}$ у LiFePO_4 и у LiFePO_4/C био 2,4 и 2,7, редом. Утврђено је да замена дела катјона олова (до 20 mol. %) у проводној фази $\text{Pb}_{0.86}\text{Sn}_{1.14}\text{F}_4$ доприноси повећању његове проводљивости у целом температурном опсегу, и у већој мери повећаној концентрацији супституента. Пренос наелектрисања је обезбеђен високо покретљивим интерситицијалним флуоридним анјонима, чија концентрација расте са повећањем температуре и садржаја супституента.

(Примљено 27. јула, ревидирано 15. новембра, прихваћено 20. новембра 2022)

REFERENCES

1. N. Nitta, F. Wu, *Mater. Today* **18** (2015) 252
(<https://doi.org/10.1016/j.mattod.2014.10.040>)
2. T. L. Kulova, *Russ. J. Electrochem.* **49** (2013) 25
(<https://doi.org/10.1134/S1023193513010102>)
3. X. Kang1, *Chem. Rev.* **104** (2004) 4303 (<https://doi.org/10.1021/cr030203g>)
4. M. S. Whittingham, *Chem. Rev.* **104** (2004) 4271 (<https://doi.org/10.1021/cr020731c>)
5. A. B. Yaroslavtsev, T. L. Kulova, *Uspekhi khimii* **84** (2015) 826
(<https://doi.org/10.1070/RCR4497>)
6. X. Li, B. Yue, *App. Catal., A* **390** (2010) 2195
(<https://doi.org/10.1016/j.apcata.2010.10.013>)
7. G. Teran-Escobar, J. Pampel, *Energy Environ. Sci.* **6** (2013) 3088
(<https://doi.org/10.1039/C3EE42204F>)
8. Z. Yang, Y. Li, *J. Catal.* **280** (2011) 247 (<https://doi.org/10.1016/j.jcat.2011.03.026>)
9. H. Miyake, H. Kozuka, *J. Phys. Chem., B* **109** (2005) 17951
(<https://doi.org/10.1021/jp058051b>)
10. N. I. Sorokin, B. P. Sobolev, *Kristallografiya* **52** (2007) 870
(<https://naukarus.com/nestehiomicheskie-ftoridy-tverdye-elektrolity-dlya-elektrohimicheskikh-ustroystv-obzor>)
11. L. N. Patro, K. Hariharan, *Solid State Ionics* **239** (2013) 41
(<https://doi.org/10.1016/j.ssi.2013.03.009>)

12. V. Trnovtsova, P. P. Fedorov, *Elektrokhimiya* **45** (2009) 668
(<https://naukarus.com/ftoridnye-tverdye-elektrolity>)
13. J. Resasco, H. Zhang, *ACS Cent. Sci.* **2** (2016) 80
(<https://doi.org/10.1021/acscentsci.5b00402>)
14. J. Gan, X. Lu, *Nanoscale* **16** (2014) 7142 (<https://doi.org/10.1039/C4NR01181C>)
15. V. O. Smilyk, S. S. Fomanyuk, G. Ya. Kolbasov, I. A. Rusetskyi, V. S. Vorobets, *Res. Chem. Intermed.* **45** (2019) 4149 (<https://doi.org/10.1007/s11164-019-03897-y>)
16. Y. Li, J. Zhu, *Sci. Chin. Chem.* **9** (2014) 1489 (<https://doi.org/10.1007/s11426-015-5348-3>)
17. Z. Yang, Y. Dai, *J. Mater. Chem., A* **4** (2016) 8210
(<https://doi.org/10.1039/C6TA05048D>)
18. L. X. Yuan, Z. H. Wang, *Energy Environ. Sci.* **4** (2011) 269
(<https://doi.org/10.1039/C0EE00029A>)
19. U. S. Kasavajjula, C. Wang, *J. Electrochem. Soc.* **155** (2008) A866
(<https://doi.org/10.1149/1.2980420>)
20. T. V. Satyavani, A. K. Srinivas, *Eng. Sci. Tech.* **19** (2016) 178
(<https://doi.org/10.1016/j.jestch.2015.06.002>)
21. T. Kodera, B. Dongying, *Key Eng. Mater.* **485** (2011) 107
(<https://doi.org/10.4028/www.scientific.net/KEM.485.107>)
22. Y. Lin, M. X. Gao, *J. Power Sources* **184** (2008) 444
(<https://doi.org/10.1016/j.jpowsour.2008.03.026>)
23. V. O. Smilyk, S. S. Fomanyuk, *Ukrayins'kyy khimichnyy zhurnal* **85** (2019) 83
(<https://doi.org/10.33609/0041-6045.85.10.2019.83-90>)
24. Ye.V. Kuzminskii, G.Ya. Kolbasov, *Sol. Energ. Mater. Sol. Cells* **56** (1999) 93
([https://doi.org/10.1016/S0927-0248\(98\)00146-9](https://doi.org/10.1016/S0927-0248(98)00146-9))
25. T. Saison, N. Chemin, *J. Phys. Chem.* **119** (2015) 12967
(<https://doi.org/10.1021/acs.jpcc.5b01468>)
26. R. Katoh, M. Kasuya, *Chem. Phys. Lett.* **471** (2009) 280
(<https://doi.org/10.1016/j.cplett.2009.02.053>)
27. C. A. Grimes, G. K. Mor, *TiO₂ Nanotube Arrays. Synthesis, Properties, and Applications*, Springer, New York, 2009, p. 358 (<https://doi.org/10.1007/978-1-4419-0068-5>)
28. R. Sharma, P.P. Das, *Nanotechnology* **20** (2009) 075704 (<https://doi.org/10.1088/0957-4484/20/7/075704>)
29. C. G. Granqvist, *Handbook of Inorganic Electrochromic Materials*, Elsevier, Uppsala, 1995 (<https://doi.org/10.1016/B978-0-444-89930-9.X5000-4>)
30. N. N. Dinh, D. H. Ninh, *J. Nanomat.* **2012** (2012) 7
(<https://doi.org/10.1155/2012/781236>)
31. M. F. Saenger, T. Höing, *Phys. Status Solidi, A* **4** (2008) 914
(<https://doi.org/10.1002/pssa.200777894>)
32. Yu. V. Pohorenko, R. M. Pshenychnyi, *J. Serb. Chem. Soc.* **86** (2021) 845
(<https://doi.org/10.2298/JSC201124031P>)
33. S. S. Fomanyuk, V. O. Smilyk, *Fr.-Ukr. J. Chem.* **06** (2018) 157
(<https://doi.org/10.17721/fujcV6I1P157-166>)
34. Q. Jia, K. Iwashina, *Proc. Natl. Acad. Sci. USA* **109** (2012) 11564
(<https://doi.org/10.1073/pnas.1204623109>)
35. D. K. Lee, K.-S. Choi, *Nat. Energy* **3** (2018) 53 (<https://doi.org/10.1038/s41560-017-0057-0>)

36. M. G. Mali, H. Yoon, *Appl. Phys. Lett.* **106** (2015) 151603 (<https://doi.org/10.1063/1.4918583>)
37. O. Bohnke, C. Bohnke, *Solid State Ionics* **6** (1982) 267 ([https://doi.org/10.1016/0167-2738\(82\)90048-0](https://doi.org/10.1016/0167-2738(82)90048-0))
38. V. Galaguz, O. Korduban, *J. Serb. Chem. Soc.* **85** (2020) 1047 (<https://doi.org/10.2298/JSC190910011G>).



A facile and sensitive coprecipitation method coupled with flame atomic absorption spectrometry for quantification of Cu(II) ions in complex matrices

DUYGU OZDES^{1*}, CELAL DURAN², HAKAN BEKTAS³ and EMRE MENTESE⁴

¹Gumushane University, Gumushane Vocational School, Chemistry and Chemical Processing Technologies Department, Gumushane, Turkey, ²Karadeniz Technical University, Faculty of Sciences, Department of Chemistry, Trabzon, Turkey, ³Giresun University, Faculty of Arts and Sciences, Department of Chemistry, Giresun, Turkey and ⁴Recep Tayyip Erdogan University, Faculty of Arts and Sciences, Department of Chemistry, Rize, Turkey

(Received 22 January, revised 19 June, accepted 21 September 2022)

Abstract: In the present investigation, the application of an organic coprecipitant, 2-[5,6-dichloro-2-(2-bromobenzyl)-1*H*-benzimidazole-1-yl]acetohydrazide (DIBBA), for separation and preconcentration of Cu(II) ions in fruit and water samples through a new carrier element free coprecipitation (CEFC) method was researched for the first time. Flame atomic absorption spectrometer (FAAS) was used for the analyses of Cu(II) ions. The main effective experimental factors such as solution pH, DIBBA quantity, waiting time, centrifuge speed and duration and volume of sample on the recovery efficiency of Cu(II) ions were explored in detail. Under the optimized conditions the preconcentration factor (*PF*), relative standard deviation (*RSD*), and limits of detection (*LOD*) was achieved as 50, 3.4 % and 0.44 µg L⁻¹, respectively. No interference effects were detected by virtue of the presence of various foreign ions. Satisfactory recoveries (in the range of 94.4 to 103.0 %) in the environmental sample matrix were acquired. After being validated the recommended selective, low cost, simple and rapid CEFC method by spike/recovery tests, it was properly implemented for the low levels detection of Cu(II) ions in sour cherry, mulberry, apple, and peach as fruit samples and stream and sea water samples without any significant matrix effects.

Keywords: copper; fruit analyse; heavy metal; preconcentration; separation; water analyses.

INTRODUCTION

Heavy metal pollution owing to both anthropogenic activities and natural sources is one of the most substantial issues to be considered due to their num-

* Corresponding author. E-mail: duyguozdes@hotmail.com
<https://doi.org/10.2298/JSC220122074O>

erous adverse effects on all living organisms and ecosystem.¹ Heavy metals, which are not degradable in nature and are permanent inorganic pollutants, mostly reach the human body with food and water.² As a result of scientific researches, behavioural disorders due to mental and neurological effects, irregularities in neurotransmitter production and their functions have been observed in people exposed to heavy metals.³ In addition, serious disorders such as disabilities and failure of some organs to function have emerged, depending on the type and concentration of heavy metals exposed. Although a number of heavy metals such as Zn, Se, Mn and Cu are indispensable at certain levels for the human body to maintain their metabolism, they provoke toxic effects if taken at high concentrations.⁴ Long-term exposure to copper causes nose, mouth and eye irritation, stomach aches and headaches, diarrhoea and vomiting. High intake of copper can also trigger liver damage and even induce death.^{5,6} The maximum admissible Cu(II) ions levels specified by the World Health Organization (WHO) in drinking water is 2.0 mg L⁻¹.⁷ In this respect, the development of accurate, precise, and selective methods to determine trace amounts of metal ions in environmental samples is a quite popular research area.⁸

Trace heavy metals can be determined using multitudinous analysis methods including flame atomic absorption spectrometry (FAAS)⁹, inductively coupled plasma atomic emission spectrometry (ICP-AES),¹⁰ UV-Vis spectrometry¹¹ and X-ray fluorescence spectrometry (XRFS).¹² FAAS is among the most prevalently applied methods in recent years in terms of its practicality, cheapness and short analysis time. Two types of critical problems are generally encountered during the quantitation of trace metals in environmental samples by aforementioned methods. One of these problems is the interference effect of the complicated matrix and the other is that the lower levels of trace element than the detection limit of the utilized instrument.¹³ In order to eliminate these drawbacks, it is indispensable to implement a traditional separation and preconcentration method such as solid phase extraction,¹⁴ cloud point extraction,¹⁵ liquid-liquid extraction¹⁶ and coprecipitation⁸ before the analyses step. Among these, coprecipitation is a powerful alternative due to its low cost, simplicity and rapidity, less usage of chemical reagents and obtaining high preconcentration factors in the method.²

The coprecipitation technique is based on the accumulation of metal ions on water-insoluble precipitates of various organic or inorganic characters.¹⁷ In general, in the coprecipitation method two types of reagents are used: *i*) inorganic coprecipitants such as hydroxides and sulphides;^{18–23} *ii*) organic coprecipitants such as some chelates or chelating ligands.^{1,9} However, in both cases, the carrier element, which is added to the medium in excessive amounts for precipitate formation, may have interference effects during the analysis step. In CEFC method, which has been introduced to the literature as a new method in recent years, an organic compound soluble in an organic solvent but insoluble in water

is used as a coprecipitating agent, while a carrier element is not required for precipitate formation.^{8,24,25} Hereby, the pollution risk induced by the carrier element is eliminated. Besides, the method is environmentally friendly as it requires the use of less chemical reagents.

The purpose of the presented research is to develop a new CEFC method by applying an organic coprecipitant, 2-[5,6-dichloro-2-(2-bromobenzyl)-1*H*-benzimidazole-1-yl]acetohydrazide (DIBBA), which was employed for the first time for the selective determination of Cu(II) ions in fruit (sour cherry, mulberry, apple and peach) and water (stream and sea water) samples. Actually, in the first stage of the study, the usability of DIBBA was investigated in the separation and preconcentration of different heavy metals such as Ni(II), Mn(II), Cd(II), Pb(II) and Cr(III) ions from environmental samples by coprecipitation method, apart from Cu(II) ions. However, quantitative recovery values were obtained only for Cu(II) ions. Therefore the experimental conditions affecting the Cu(II) ions recovery efficiency including sample pH, DIBBA amount, waiting time, centrifuge speed and duration and sample volume were evaluated and optimized. The method validation was performed via spike tests and then the applicability of the method was evaluated by the analysis of Cu(II) ions in the fruit and water samples.

EXPERIMENTAL

Chemicals and instruments

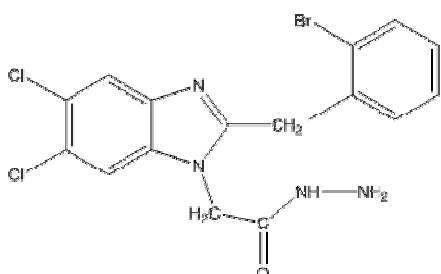
Perkin Elmer AAnalyst 400 model flame atomic absorption spectrophotometer (FAAS) equipped with hollow cathode lamp was employed to determine Cu(II) levels in the solutions. Ground interference was eliminated with deuterium lamp. Analyses were performed at the primary wavelength (324.8 nm) of the copper element. In addition, the following instruments were employed during the experiments; Nuve NF 200 model centrifuge for separating the precipitates from the solution, Hanna pH-211 digital pH meter with glass electrode for adjusting the pH of the solutions, and Milestone Ethos D closed vessel microwave solubilisation system with a maximum pressure and temperature of 10 MPa and 300 °C, respectively for digestion of fruit samples.

All of the reagents including HNO₃, NaOH, ethyl alcohol, dimethyl sulfoxide (DMSO), NaCl, NH₄NO₃, KCl, H(AuCl₄), CaCl₂, Mg(NO₃)₂, Mn(NO₃)₂, NaNO₃, Na₂CO₃, Cu(NO₃)₂, Zn(NO₃)₂ and Cr(NO₃)₃ used at different stages of the experimental studies were of analytical reagent grade and were purchased from Fluka (Buchs, Switzerland) or Merck (Darmstadt, Germany). The stock solution of copper at a concentration of 1000 mg L⁻¹, prepared in 0.5 vol. % HNO₃, was diluted daily for the preparation of standard and working solutions. Milli-Q system was utilized to obtain the distilled/deionized water used throughout the experiments. The synthesis of the coprecipitating agent, DIBBA, was performed by the procedure expressed in the literature.²⁶ The chemical structure of DIBBA was given in Scheme 1. To prepare 100 mL of 0.2 % DIBBA solution, 0.2 g of DIBBA was weighed and dissolved in a mixture of 100 mL of ethyl alcohol and DMSO (1:1) by heating at 80 °C.

General procedure of the developed coprecipitation method

Two mL of DIBBA (0.2 %) were added to 15.0 mL of model solutions containing 5.0 µg of Cu(II) ions in centrifuge tubes. The solutions' pH value was arranged to 8.0 using diluted

HNO_3 or NaOH solutions. For the formation of the precipitate, these solutions were waited for 5 min. At the end of this waiting period, the mixture was centrifuged at 2500 rpm for 3 min and the supernatant was decanted. The precipitate remaining at the bottom of the tube was dissolved by using 1.0 mL of concentrated HNO_3 . The volume was completed to 2.0 mL with distilled water, and then $\text{Cu}(\text{II})$ ions levels were determined in the final solution by FAAS.



Scheme 1. Chemical structure of DIBBA.

Preparation of water and fruit samples

The developed CEFC methodology based on DIBBA was carried out to fruit samples (sour cherry, mulberry, apple, and peach) obtained from a local market in Gümüşhane and water (stream and sea waters) samples collected from Trabzon to determine their $\text{Cu}(\text{II})$ ions levels.

After being collected the sea and stream water samples in prewashed polyethylene bottles, they were acidified with 1 % nitric acid solution. Cellulose nitrate membrane was used for the filtration of the water samples. The pH of the filtrated samples was adjusted to 8.0 before applying the method.

The fruit samples were dried at 90 °C in an oven for 24 h and then homogenized by grinding in an agate mortar. Then the homogenized samples were digested by a closed vessel microwave digestion system. For this purpose, the fruit samples weighing 0.75 g were placed in Teflon vessels, separately. 2.0 mL of H_2O_2 and 6.0 mL of HNO_3 were used as digestion reagents. The microwave digestion program was implemented in four sequential steps at a pressure of 4.56 MPa: 1) 6 min to reach 160 °C (power (P) = 250 W); 2) 6 min to hold 180 °C (P = 400 W); 3) 6 min to reach 220 °C (P = 650 W); 4) 6 min to hold 220 °C (P = 250 W). After microwave digestion the volume of each sample was made up to 50 mL with distilled water and the $\text{Cu}(\text{II})$ ions were preconcentrated performing the suggested procedure.

RESULTS AND DISCUSSION

Optimization of the experimental parameters

The pH of the aqueous media is a critical factor in the quantitative recovery of analyte ions, since it directly affects the competition of metal ions and hydronium or hydroxide ions. In addition, the surface charge of the precipitate formed is enormously dependent on the pH value of the aqueous media. The influences of pH on the recovery of $\text{Cu}(\text{II})$ ions applying the CEFC method based on DIBBA was scrutinized in the pH range of 2.0–8.0. In these experiments, 4.0 mg of DIBBA was added to 15 mL of solutions at different pH values containing 5.0 μg of $\text{Cu}(\text{II})$ ions and the waiting time, centrifuge speed and duration kept as 5 min, 2500 rpm and 3 min, respectively. At pH 2.0, $\text{Cu}(\text{II})$ ions recovery value

was 6.9 % and it increased distinctively as the pH increased, reaching 97.3 % at pH 8.0 (Fig. 1). The surface of the precipitate formed at acidic pH values is positively charged due to the excess hydronium ions in the medium. The electrostatic repulsion between the positively charged precipitate surface and the metal cations prevents the retention of the metal cations on the precipitate surface. Therefore, the recovery values were low at acidic pH. On the contrary, as the pH increases, the surface of the precipitate becomes negatively charged due to the hydroxide ions present in the solution. An electrostatic interaction occurs between the precipitate surface and the metal cations which resulted in the increase of recovery values. Cu(II) ions are collected on the precipitate through surface adsorption, inclusion, and occlusions mechanisms. In precipitation by adsorption mechanism, the electrostatic interaction between the precipitate surface and metal ions becomes important. Consequently, the optimum pH was specified as 8.0 for the analyses of Cu(II) ions quantitatively.

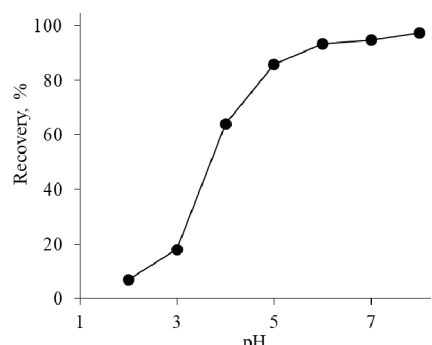


Fig. 1. Effect of pH on the Cu(II) ions recovery.

The impacts of DIBBA quantity on the Cu(II) ions recovery were assessed in the DIBBA amount range of 0.0–6.0 mg (3.0 mL of 0.2 % solution) at the solution pH of 8.0. When the CEFC experiments were carried out without adding any DIBBA to the medium, it is noticed that the recovery value of Cu(II) ions was less than 70 %. The recovery value of Cu(II) ions increased from 82.2 to 97.8 % with the increase of DIBBA amount from 0.5 to 2.0 mg and remained approximately constant with the subsequent increases in DIBBA quantity (Fig. 2). These results demonstrated that DIBBA is indispensable for the determination of Cu(II) ions quantitatively through the proposed CEFC method. The amount of DIBBA was determined as 4.0 mg (2.0 mL of 0.2 % solution) for further studies.

Since the waiting time, centrifuge speed and duration have considerable influence on the quality of the precipitate formed in the aqueous solution, the impacts of these factors on the recovery of Cu(II) ions were evaluated in detail. For this reason, the coprecipitation analyses were carried out at 1–120 min of waiting time, 1000–5000 rpm of centrifuge speed, and 1–10 min of centrifuge duration. For the quantitative recovery of Cu(II) ions with the CEFC method based on

DIBBA, the optimum waiting time, centrifuge speed and duration were determined as 5 min, 2500 rpm and 3 min, respectively.

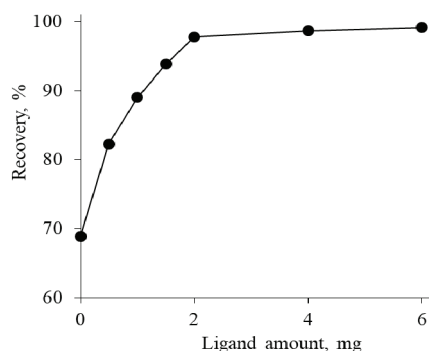


Fig. 2. Influences of DIBBA quantity on the Cu(II) ions recovery.

High preconcentration factors (PF) are required in order to determine the analyte ions present at very low levels in environmental samples with the developed separation and preconcentration methods. The most important factor affecting the PF is the sample volume since the PF is calculated by dividing the optimum sample volume by the final volume. Therefore, the influences of sample volume were assessed at different sample volumes between 100 and 1000 mL. The Cu(II) ions were recovered quantitatively up to 100 mL of sample volume. It is noticed that the recovery values decreased rapidly at volumes higher than 100 mL (Fig. 3). As a result, PF was obtained as 50 when used 100 mL of sample volume and 2 mL of final volume.

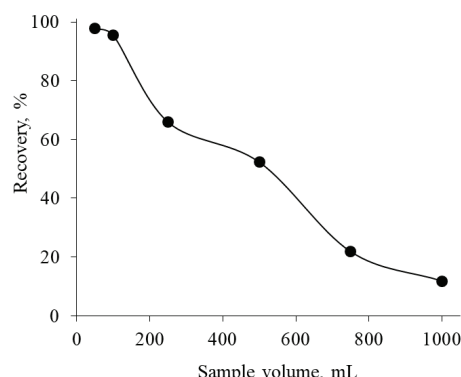


Fig. 3. Sample volume impact on the recovery of Cu(II) ions.

Influences of matrix ions

Since the proposed process was implemented to analyse the Cu(II) ions in fruit and water samples, the possible disruptive effect of the common coexisting ions on the performance of the process should be investigated. The maximum levels of different anions and cations that can be found together with Cu(II) ions

were chosen and their effects on the recovery efficiency of Cu(II) ions were evaluated. In these tests, certain concentration of coexisting ions were added to the 50 mL of model solution containing 5.0 µg of Cu(II) ions and the developed procedure was carried out. Satisfactory recoveries changing between 92.6 and 100.2 % for Cu(II) ions were obtained (Table I).

TABLE I. Influences of matrix ions on the recovery of Cu(II) ions; * – nitrate salts were used

Ion	Added as	$c_{\text{Cu(II)}} / \text{mg L}^{-1}$	Recovery, %
Na ⁺	NaCl	5000	95.3±3.1
K ⁺	KCl	1000	94.7±2.2
Ca ²⁺	CaCl ₂	1000	96.3±0.7
Mg ²⁺	Mg(NO ₃) ₂	1000	95.0±2.1
CO ₃ ²⁻	Na ₂ CO ₃	1000	92.6±1.8
NO ₃ ⁻	NaNO ₃	1000	93.9±2.6
NH ₄ ⁺	NH ₄ NO ₃	1000	94.2±1.5
Au(III), Mn(II), Cr(III), Zn(II)	*	25	97.6±0.7
Mixed ^a	–	–	100.2±1.0

^a687 mg L⁻¹ Na⁺, 1040 mg L⁻¹ Cl⁻, 960 mg L⁻¹ NO₃⁻, 100 mg L⁻¹ K⁺, PO₄³⁻, Ca²⁺, NH₄⁺, CO₃²⁻, Mg²⁺, 10 mg L⁻¹ Au(III), Mn(II), Cr(III), Zn(II)

The effect of Au(III), Mn(II), Cr(III) and Zn(II) concentrations on the recovery of Cu(II) ions was investigated in the concentration range of 5–25 mg L⁻¹ and it was seen that the recovery of Cu(II) ions was quantitative in all foreign heavy metal ions concentrations studied. Since Au(III), Mn(II), Cr(III) and Zn(II) concentrations will not be higher than 25 mg L⁻¹ in the environmental samples to which the method will be applied, only the highest concentration levels of them is given in Table I. These results demonstrated that the foreign ions have a minimal interfering impact on the analyses of Cu(II) ions with the suggested method and it can be concluded that the process can be performed successfully for the coprecipitation of Cu(II) ions in complicated matrices.

Analytical figure of merits

The substantial analytical features of the developed CEFC method based on DIBBA including *RSD*, *LOD* and limit of quantification (*LOQ*) were acquired under the following optimized experimental conditions; pH: 8.0, DIBBA amount: 2.0 mg, waiting time: 5 min, centrifuge speed: 2500 rpm and centrifuge duration: 3 min. The method precision was evaluated with respect to *RSD*, obtained by practicing the method ten times to model solutions containing 5.0 µg of Cu(II) ions under the given experimental conditions above. Accordingly, the *RSD* was calculated as 3.4 %. The *LOD* was calculated by considering three times the standard deviations obtained by the blank analyses ($n = 10$) and for the *LOQ*, ten times the standard deviation achieved from blank analyses ($n = 10$) was taken into account. The *LOD* and *LOQ* were found to be 0.44 and 1.47 µg L⁻¹, respectively. The comparison of the developed method with other Cu(II) coprecipitation

studies in literature from the point of solution pH, *LOD*, *RSD* and *PF* is given in Table II.

TABLE II. Comparison of the present CEFC system with different Cu(II) ions coprecipitation studies in literature

System	<i>PF</i>	LOD / $\mu\text{g L}^{-1}$	<i>RSD</i> / %	pH	Ref.
La-2,2'-bipyridyl-erythrosine	50	10.3	1.85	4.5	¹⁷
APSAL ^a	100	0.5	<5	7.0	²⁴
2,9-dimethyl-4,7-diphenyl-1,10-phenanthroline	25	0.80	8	9.0	²⁷
<i>N</i> -cetyl <i>N,N,N</i> -trimethyl ammonium bromide	10	1.36	<5	10.0	²⁸
ICOTMA ^b	50	0.56	2.8	7.0	²⁹
Zirconium(IV) hydroxide	25	1.55	6.4	8.0	³⁰
Ni ²⁺ /2-Nitroso-1-naphthol-4-sulfonic acid	25	1.3	3.8	8.0	³¹
MEFMAT ^c	50	1.49	2.0	6.8	³²
Ni(II)-salicylaldoxime	20	1.32	2.5	9.0	³³
DIBBA	50	0.44	3.4	8.0	This study

^a4-(2-Hydroxybenzylideneamino)-1,2-dihydro-2,3-dimethyl-1-phenylpyrazol-5-one; ^b2-[4-[2-(1H-indol-3-yl)ethyl]-3-(4-chlorobenzyl)-5-oxo-4,5-dihydro-1*H*-1,2,4-triazol-1-yl]-*N*-aryl-methylidene acetohydrazid; ^c2-[{[4-(4-fluorophenyl)-5-sulphonyl-4*H*-1,2,4-triazol-3-yl]methyl}-4-{{[(4-fluorophenyl)methylene]amino}-5-(4-methylphenyl)-2,4-dihydro-3*H*-1,2,4-triazol-3-one]

The fact that the developed CEFC method based on DIBBA has lower *LOD* and *RSD* values and high *PF* value compared to many methods in the literature indicates the superiority and suitability of the process.^{17,24,27–33}

Analysis of real samples

The spike/recovery test was applied for both fruit and water samples for the validation of the method. The relative recovery (*RR*) values obtained for the water (Table III) and the fruit samples (Table IV) were in the range of 96.3–103.0 % and 94.4–100.6 %, respectively. The good agreement between the added and found values demonstrated the validity of the method and also its applicability with high accuracy without significant matrix effect. Eventually, the suggested methodology was applied smoothly to determine Cu(II) ions levels of several water and fruit samples (Table V).

TABLE III. Recovery of Cu(II) ions from water samples (50 mL of each sample volume and 2.0 mL of final volume); ND – not detected

Quantity of Cu(II) added to the medium, μg	Stream water		Sea water	
	Quantity of Cu(II) found, μg	Recovery %	Quantity of Cu(II) found, μg	Recovery %
0	ND	—	ND	—
20	20.6±0.5	103.0	19.4±0.7	97.0
40	38.5±1.6	96.3	40.1±1.2	100.3

TABLE IV. Cu(II) ions recovery from fruit samples (0.75 g of each fruit sample quantities and 2.0 mL of final volume)

Sample	Quantity of Cu(II), μg		Recovery, %
	Added	Found	
Sour cherry	0	2.53 \pm 0.06	—
	20	21.4 \pm 0.5	94.4
Mulberry	0	2.88 \pm 0.08	—
	20	23.0 \pm 0.6	100.6
Apple	0	2.45 \pm 0.06	—
	20	21.7 \pm 0.4	96.3
Peach	0	3.72 \pm 0.12	—
	20	22.8 \pm 0.5	95.4

TABLE V. Cu(II) levels in water ($\mu\text{g L}^{-1}$) and fruit samples ($\mu\text{g g}^{-1}$, 100 mL of each sample volume, 0.75 g of each fruit sample quantities, and 2.0 mL of final volume)

Liquid samples			Solid samples		
Sea water	Stream water	Sour Cherry	Mulberry	Apple	Peach
3.38 \pm 0.10	15.10 \pm 0.48	3.37 \pm 0.05	3.84 \pm 0.13	3.27 \pm 0.07	4.96 \pm 0.15

CONCLUSION

A new organic coprecipitant, DIBBA, exhibited a great potential for separation and preconcentration of Cu(II) ions by carrier element free coprecipitation (CEFC) method. Until now, DIBBA has not been applied in any other analytical applications. The preconcentration conditions were optimized with respect to pH (8.0), DIBBA amount (4.0 mg), volume of sample (100 mL), waiting time (5 min), centrifuge duration and speed (3 min and 2500 rpm). Short waiting time and centrifuge duration as well as low LOD and RSD values and high preconcentration factor are the notable advantages of the presented method. Since the carrier element was not used for the precipitate formation in the method, the contamination risk originated from the carrier element and the possible interference effect in the determination of the analyte ions were eliminated. In addition, the method allows the use of chemical reagents and harmful solvents at a minimum level and thus it will be beneficial in reducing the environmental pollution. In brief, the obtained results indicated that the proposed sensitive and facile method is a promising alternative for the determination of Cu(II) ions in fruit and water samples.

Acknowledgement. The financial support from the Unit of the Scientific Research Projects of Karadeniz Technical University is gratefully acknowledged.

И З В О Д

ЈЕДНОСТАВНА И ОСЕТЉИВА МЕТОДА КОПРЕЦИПИТАЦИЈЕ У КОМБИНАЦИЈИ СА
ПЛАМЕНОМ АТОМСКОМ АПСОРПЦИОНОМ СПЕКТРОМЕТРИЈОМ ЗА
КВАНТИФИКАЦИЈУ Cu(II) ЈОНА У СЛОЖЕНИМ МАТРИЦАМА

DUYGU OZDES¹, CELAL DURAN², HAKAN BEKTAS³ и EMRE MENTESE⁴

¹Gumushane University, Gumushane Vocational School, Chemistry and Chemical Processing Technologies Department, Gumushane, Turkey, ²Karadeniz Technical University, Faculty of Sciences, Department of Chemistry, Trabzon, Turkey, ³Giresun University, Faculty of Arts and Sciences, Department of Chemistry, Giresun, Turkey and ⁴Recep Tayyip Erdogan University, Faculty of Arts and Sciences, Department of Chemistry, Rize, Turkey

У овом истраживању коришћен је 2-[5,6-дихлоро-2-(2-бромобезил)-1Н-бензими-дазол-1-ил]ацетохидразид (DIBBA), као копреципитациони реагенс, за сепарацију и предконцентрацију Cu(II) јона у узорцима воћа и вода, први пут применом нове методе копреципитације без елемента у носачу. Примењена је пламена атомска апсорпциона спектрометрија за анализу Cu(II) јона. Детаљно су испитивани експериментални услови, који утичу на ефикасност и принос Cu(II) јона, као што су pH, количина DIBBA, време и брзина центрифугирања и запремина узорка. Под оптималним условима предконцентрациони фактор (PF), релативна стандардна девијација (RSD) и границе детекције (LOD) су износили 50, 3,4% и 0,44 μg L⁻¹, редом. Нису детектоване интерференције у присуству страних јона. Постигнут је задовољавајући проценат приноса (94,4–103,0 %) у узорцима из животне средине. После валидације методе, као селективне, економичне, једноставне и брзе, CEFC метода је примењена за детекцију ниског нивоа концентрација Cu(II) јона у узорцима вишана, дудиња, јабука и бресака, као и морске и воде из потока без значајног утицаја матрице.

(Примљено 22. јануара, ревидирано 19. јуна, прихваћено 21. септембра 2022)

REFERENCES

1. M. Soylak, N. D. Erdogan, *J. Hazard. Mater.*, **B 137** (2006) 1035
(<https://doi.org/10.1016/j.jhazmat.2006.03.031>)
2. X. Hu, *Int. J. Environ. Anal. Chem.* **91** (2011) 263
(<https://doi.org/10.1080/03067310903509286>)
3. H. Ahmad, C. Liu, *J. Hazard. Mater.* **415** (2021) 125661
(<https://doi.org/10.1016/j.jhazmat.2021.125661>)
4. S.Z. Mohammadi, T. Shamsipur, Y. M. Baghelani, *Arab. J. Chem.* **12** (2019) 1751
(<https://doi.org/10.1016/j.arabjc.2014.11.054>)
5. Z. Dahaghin, H. Z. Mousavi, S. M. Sajjadi, *J. Mol. Liq.* **231** (2017) 386
(<https://doi.org/10.1016/j.molliq.2017.02.023>)
6. J. Abolhasani, M. Behbahani, *Environ. Monit. Assess.* **187** (2015) 4176
(<https://doi.org/10.1007/s10661-014-4176-9>)
7. M. Behbahani, M. Salarian, M. M. Amini, O. Sadeghi, A. Bagheri, S. Bagheri, *Food Anal. Methods* **6** (2013) 1320 (<https://doi.org/10.1007/s12161-012-9545-9>)
8. C. Duran, D. Ozdes, H.T. Akcay, H. Serencam, M. Tufekci, *Desalin. Water Treat.* **53** (2015) 390 (<https://doi.org/10.1080/19443994.2013.839401>)
9. M. Tuzen, M. Soylak, *J. Hazard. Mater.* **162** (2009) 724
(<https://doi.org/10.1016/j.jhazmat.2008.05.087>)

10. L.M. Tasić, D. S. Ignjatović, L. M. Ignjatović, B. Andelković, M. P. Antić, V. Rajaković, *J. Serb. Chem. Soc.* **81** (2016) 403 (<https://doi.org/10.2298/JSC150429078T>)
11. F. Cheng, C. Yang, C. Zhou, L. Lan, H. Zhu, Y. Li, *Sensors* **20** (2020) 4936 (<https://doi.org/10.3390/s20174936>)
12. K. Pytlakowska, M. Matussek, B. Hachula, M. Pilch, K. Kornaus, M. Zubko, W.A. Pisarski, *Spectrochim. Acta, B* **147** (2018) 79 (<https://doi.org/10.1016/j.sab.2018.05.023>)
13. N. Kobylinska, L. Kostenko, S. Khainakov, S. Garcia-Granda, *Microchim. Acta* **187** (2020) 289 (<https://doi.org/10.1007/s00604-020-04231-9>)
14. E. Çetinkaya, A. Aydin, *Desalin. Water Treat.* **74** (2017) 224 (<https://doi.org/10.5004/dwt.2017.20702>)
15. D. Snigur, A. Chebotarev, V. Dubovyi, D. Barbalat, A. Klochkova, *J. Serb. Chem. Soc.* **85** (2020) 89 (<https://doi.org/10.2298/JSC190212087S>)
16. O. A. Urucu, E. K. Yetimoğlu, Ş. Dönmez, S. Deniz, *J. Serb. Chem. Soc.* **84** (2019) 435 (<https://doi.org/10.2298/JSC180831110U>)
17. B. Feist, B. Mikula, K. Pytlakowska, B. Puzio, F. Buhl, *J. Hazard. Mater.* **152** (2008) 1122 (<https://doi.org/10.1016/j.jhazmat.2007.07.095>)
18. L. S. Moreira, Í. P. Sá, R. C. Machado, A. R. A. Nogueira, E. G. P. da Silva, C. D. B. Amaral, *Spectrochim. Acta, B* **169** (2020) 105899 (<https://doi.org/10.1016/j.sab.2020.105899>)
19. S. Saracoglu, M. Soylak, D. Çabuk, Z. Topalak, Y. Karagozlu, *J. AOAC Int.* **95** (2012) 892 (<https://doi.org/10.5740/jaoacint.11-304>)
20. V. N. Conceição, T.G. Campos, B. M. Dalfior, O. A. Heringer, G. P. Brandão, M. T. W. D. Carneiro, *J. Braz. Chem. Soc.* **32** (2021) 231 (<https://dx.doi.org/10.21577/0103-5053.20200172>)
21. A. Muhammed, A. Hussen, T. Kaneta, *Anal. Sci.* **38** (2022) 123 (<https://doi.org/10.2116/analsci.21P215>)
22. Z. Arslan, T. Oymak, J. White, *Anal. Chim. Acta* **1008** (2018) 18 (<https://doi.org/10.1016/j.aca.2018.01.017>)
23. N. Thubkhun, N. Tangtreamjittmun, *Anal. Sci.* **34** (2018) 849 (<https://doi.org/10.2116/analsci.17P582>)
24. A.A. Gouda, *Talanta* **146** (2016) 435 (<https://doi.org/10.1016/j.talanta.2015.09.005>)
25. V.N. Bulut, D. Ozdes, O. Bekircan, A. Gundogdu, C. Duran, M. Soylak, *Anal. Chim. Acta* **632** (2009) 35 (<https://doi.org/10.1016/j.aca.2008.10.073>)
26. E. Menteşe, H. Bektaş, S. Ülker, O. Bekircan, B. Kahveci, *J. Enzyme Inhib. Med. Chem.* **29** (2014) 64 (<https://doi.org/10.3109/14756366.2012.753880>)
27. D. Mendil, M. Karatas, M. Tuzen, *Food Chem.* **177** (2015) 320 (<https://doi.org/10.1016/j.foodchem.2015.01.008>)
28. S. Saracoglu, M. Soylak, *Food Chem. Toxicol.* **48** (2010) 1328 (<https://doi.org/10.1016/j.fct.2010.02.033>)
29. Z. Bahadir, V.N. Bulut, D. Ozdes, C. Duran, H. Bektas, M. Soylak, *J. Ind. Eng. Chem.* **20** (2014) 1030 (<https://doi.org/10.1016/j.jiec.2013.06.039>)
30. D. Citak, M. Tuzen, M. Soylak, *Food Chem. Toxicol.* **47** (2009) 2302 (<https://doi.org/10.1016/j.fct.2009.06.021>)
31. O.D. Uluozlu, M. Tuzen, D. Mendil, M. Soylak, *J. Hazard. Mater.* **176** (2010) 1032 (<https://doi.org/10.1016/j.jhazmat.2009.11.144>)

32. C. Duran, D. Ozdes, D. Sahin, V.N. Bulut, A. Gundogdu, M. Soylak, *Microchem. J.* **98** (2011) 317 (<https://doi.org/10.1016/j.microc.2011.02.018>)
33. Ş. Tokaloğlu, S. Yıldız, *Microchim. Acta* **165** (2009) 129 (<https://doi.org/10.1007/s00604-008-0110-6>).



Structure and properties of ZnO/ZnMn₂O₄ composite obtained by thermal decomposition of terephthalate precursor

LIDIJA RADOVANOVIC^{1*}, ŽELJKO RADOVANOVIC^{1#}, BOJANA SIMOVIĆ^{2#},
MILICA V. VASIĆ³, BOJANA BALANČ¹, ALEKSANDRA DAPČEVIĆ^{4#},
MIROSLAV DRAMIĆANIN⁵ and JELENA ROGAN^{4#}

¹Innovation Centre of the Faculty of Technology and Metallurgy, University of Belgrade,
Karnegijeva 4, Belgrade, Serbia, ²Institute for Multidisciplinary Research, University of
Belgrade, Kneza Višeslava 1, Belgrade, Serbia, ³Institute for Testing of Materials IMS,
University of Belgrade, Bulevar vojvode Mišića 43, Belgrade, Serbia, ⁴Faculty of
Technology and Metallurgy, University of Belgrade, Karnegijeva 4, Belgrade, Serbia and
⁵Vinča Institute of Nuclear Sciences, University of Belgrade, P.O. Box 522, Belgrade, Serbia

(Received 2 November, revised 17 December, accepted 21 December 2022)

Abstract: A biphasic $[\text{Mn}(\text{dipy})(\text{H}_2\text{O})_4](\text{tpht})/\{[\text{Zn}(\text{dipy})(\text{tpht})]\cdot\text{H}_2\text{O}\}_n$ complex material, **I** ($\text{dipy} = 2,2'$ -dipyridylamine, $\text{tpht}^2- =$ dianion of terephthalic acid) was synthesized by ligand exchange reaction and characterized by XRPD and FTIR spectroscopy. A ZnO/ZnMn₂O₄ composite, **II**, has been prepared via thermal decomposition of **I** in an air atmosphere at 450 °C. XRPD, FTIR and FESEM analyses of **II** revealed the simultaneous presence of spherical nanoparticles of wurtzite ZnO and elongated nanoparticles of spinel ZnMn₂O₄. The specific surface area of **II** was determined by the BET method, whereas the volume and average size of the mesopores were calculated in accordance with the BJH method. The measurements of the mean size, polydispersity index and zeta potential showed colloidal instability of **II**. Two band gap values of 2.4 and 3.3 eV were determined using UV–Vis diffuse reflectance spectroscopy, while the measurements of photoluminescence revealed that **II** is active in the blue region of the visible spectrum. Testing of composite **II** as a pigmentary material showed that it can be used for the colouring of a ceramic glaze.

Keywords: zinc(II)/manganese(II) complex; 1,4-benzenedicarboxylate; thermolysis; zincite; hetaerolite.

INTRODUCTION

Metal oxides and mixed metal oxides belong to the largest and most useful class of solid materials which have been extensively studied from various aspects

* Corresponding author. E-mail: lradovanovic@tmf.bg.ac.rs

Serbian Chemical Society member.

<https://doi.org/10.2298/JSC221102090R>

due to structural, compositional and functional diversities.^{1,2} Zinc oxide (ZnO , zincite) is a multifunctional material with excellent properties, such as high chemical, thermal and mechanical stability, low toxicity, as well as high photostability, which is why it has been used in ceramics, medicine and photocatalysis.³ Zinc manganese oxide ($ZnMn_2O_4$, hetaerolite) with spinel structure has been widely known for its magnetic, electronic or catalytic properties.⁴ During the last decades the search for new materials that can be used as inorganic pigments is in grow, with a special emphasis on environmental suitability.^{5,6} Inorganic pigments are important materials for colouring glazes, ceramics, plastics and glasses, owing to their high opacity, thermal stability and chemical resistance.⁷ ZnO is a non-toxic alternative for lead white,⁸ while $ZnMn_2O_4$, obtained from spent alkaline batteries, is suitable as brown pigment.⁹

Transition metal (TM) complexes with the anion of 1,4-benzenedicarboxylic (terephthalic, H_2tpht) acid are functional materials with numerous applications in chemistry and material science.¹⁰ The usage of the $tpht^{2-}$ anion as a linker between metal centres can result in the formation of fascinating supramolecular topologies because of diversity of coordination modes ranging from monodentate to even dodecadentate.^{11,12} Until now, a vast number of TM– $tpht$ compounds with different nuclearity and dimensionality, have been prepared and characterized, with many of them having $tpht$ as a bridging ligand.¹³ The possibility of using TM complexes as single-source precursors for obtaining functional oxide and mixed metal oxide nanomaterials by the direct thermal decomposition process has been assessed lately.^{14,15} This approach, compared with the conventional synthetic methods, has several advantages such as the possibility of stoichiometry control and homogeneity from both aspects, in terms of metals distribution as well as in the terms of size and morphology of nanoparticles of obtained oxides.¹⁴

As a contribution to our previous research¹⁶ relating the design and synthesis of mono- and heteronuclear TM complexes to prepare new functional materials, here we presented the synthesis, spectral and structural properties of a new biphasic Mn/Zn complex precursor (**I**) composed of coordination compounds $[Mn(dipy)(H_2O)_4](tpht)$ and $\{[Zn(dipy)(tpht)]\cdot H_2O\}_n$ (dipy = 2,2'-dipyridylamine), whose crystal structures have been described previously.^{17,18} Following the preparation of the oxide nanomaterials by solid-state thermal decomposition of TM complexes, the biphasic complex **I** has been used as a single-source precursor for the synthesis of a composite powder **II** containing ZnO and $ZnMn_2O_4$. The structural, spectral, morphological, optical and photoluminescence properties of **II** have been investigated, as well as the possibility of using this material as a pigment.

EXPERIMENTAL

Materials

Except for dipya, which was of purum quality, all reagents were of analytical grade and used without further purification.

*Synthesis of biphasic Mn/Zn complex precursor (**I**)*

A solution of dipya (0.34 g, 2.0 mmol) in 7.5 cm³ of EtOH was added into solution prepared by diluting a mixture of 1.0 M Mn(NO₃)₂ (1.0 cm³, 1.0 mmol) and 1M Zn(NO₃)₂ (1.0 cm³, 1.0 mmol) by 50 cm³ of distilled water. Then, 25 cm³ of an aqueous solution of Na₂tpht (10 cm³, 2.0 mmol) was added dropwise at room temperature under continuous magnetic stirring. The obtained (beige) microcrystalline precipitate was filtered off after standing overnight, washed with small amounts of distilled water, EtOH and Et₂O and dried at room temperature.

*Solid-state synthesis of ZnO/ZnMn₂O₄ composite (**II**)*

The ZnO/ZnMn₂O₄ composite (**II**) has been obtained by the thermal degradation of precursor **I** in the air atmosphere. The mass of 0.45 g of **I** was heated at the constant rate up to 150 °C, isothermally calcined at 150 °C for 30 min, then heated at the constant rate up to 450 °C, and isothermally calcined at 450 °C during 1 h, and finally, spontaneously cooled to the room temperature. Yield: 19 %.

Measurements

The X-ray powder diffraction (XRPD) measurements for **I** and **II** were performed on a Rigaku SmartLab diffractometer using CuK α radiation, at 40 kV and 30 mA, in Bragg–Brentano geometry. Diffraction data were collected in the range 3° < 2θ < 120° (scan speed: 1° min⁻¹, step width: 0.01°) for **I** and in the range 10° < 2θ < 70° (scan speed: 1° min⁻¹, step width: 0.01°) for **II** at room temperature. The crystal structure refinement of **I** and **II** was obtained by the full structure matching mode of the Rietveld refinement technique,¹⁹ using the FULLPROF software.²⁰ The average crystallite size ($<\!D\!>$) for **II** was calculated using the Rigaku PDXL2 software and the whole powder pattern fitting (WPPF) method.

ATR-FTIR spectra of **I** and **II** were recorded in absorbance mode using a Nicolet™ iS™ 10 FTIR spectrometer (Thermo Fisher Scientific) with Smart iTR™ ATR sampling accessories, within the range of 4000–400 cm⁻¹, at a resolution of 4 cm⁻¹ and in 20 scan mode.

Field emission scanning electron microscopy (FESEM) Tescan Mira 3 XMU was used for the morphological characterization of **II**. Using Mira software, the micrographs were analysed and the average diameters of the particles of **II** (more than 100 particles) were determined.

Diffuse reflectance UV–Vis spectrum for **II** was measured over the 200–800 nm spectral region (BaSO₄ was used as a reference standard) by Shimadzu UV-2600 spectrophotometer equipped with an integrating sphere.

The specific surface area (SSA) of **II** was calculated according to the Brunauer, Emmett and Teller (BET) method from the linear part of the nitrogen adsorption isotherm at 77 K on a Micrometrics ASAP 2020 instrument. Before the measurements, the samples were out-gassed at 150 °C for 10 h under a vacuum. The total pore volume (V_{tot}) was given at relative pressure $p/p_0 = 0.998$. The volume of the mesopores was calculated according to the Barrett, Joyner and Halenda (BJH) method from the desorption branch of the isotherm.

The mean size, polydispersity index (PDI) and zeta potential of **II** were measured by photon correlation spectroscopy and by electrophoretic light scattering using Zetasizer Nano

ZS (Malvern Instruments Ltd., Malvern, UK). The measurements were performed at the room temperature, and each sample was measured three times.

Photoluminescence (PL) measurements of **II** were performed at room temperature on Fluorolog-3 model FL3-221 spectrofluorimeter system (Horiba Jobin Yvon), utilizing a 450 W Xenon lamp as the excitation source for the steady-state measurements and xenon–mercury pulsed lamp for the time-resolved measurements. The emission spectrum of **II** was scanned in the range of wavelengths from 380 to 650 nm under 350 nm excitations. The TBX-04-D PMT detector was used for both time-resolved and steady state acquisitions. The line intensities and positions of the measured spectra were calibrated with a standard mercury–argon lamp. PL measurements were performed on pellets prepared from the powders under a pressure of 10 MPa.

To test the synthesized material **II** as a pigment for ceramic tiles glazing, several probes were done. The specimens in the shape of discs were prepared by dry hydraulic pressing of the raw clays ground to the fraction below 0.5 mm. The methodology is explained in more detail in the literature.²² The specimens were dried to a constant mass in laboratory conditions. The blank transparent glaze was composed of ceramic glass frit in a quantity of 50 mass %, and the rest was distilled water. The freshly prepared batch was applied to the samples by immersing them in the mixture solution. The other probe consisted of the same glazing batch with the addition of 5 mass % of dried powder of pigment **II**. Both kinds of discs were dried overnight at 105 °C. The single-firing process was conducted in an oxidizing laboratory kiln using the usual regime for illitic-kaolinitic clays²¹ to obtain a highly vitrified product.²² The final firing temperature was set to 1200 °C based on preliminary probes with blank glazed samples. The chemical composition of the ceramic frit is obtained by energy dispersive X-ray fluorescence (XRF) using the Spectro Xepos instrument that contains 50 W/60 kV X-ray tube. The colour-space $L^*a^*b^*$ coordinates (L^* = lightness, a^* = saturation, b^* = intensity) of the obtained ceramic glazes were determined using a portable spectrophotometer ColorLite (SPH870) by a spectral scan in the steps of 7 recordings in 1 s. The certified white standard CL20602 is used as a reference. The obtained results showed values of L^* , a^* and b^* , providing information on red ($a^* > 0$) or green $a^* < 0$ and yellow ($b^* > 0$) or blue ($b^* < 0$) hues. The lightness of 0 is a standard of black, while 100 presents white colour. Glazed ceramic samples were recorded using a microscope at a magnification in the range of 40–400×. The samples were illuminated by an 1800 lm LED light source during shooting.

RESULTS AND DISCUSSION

Characterization of precursor I

XRPD pattern for biphasic precursor **I** is presented in Fig. 1 and it showed that the system is composed of complexes $[\text{Mn}(\text{dipy})(\text{H}_2\text{O})_4](\text{tpht})$ and $\{[\text{Zn}(\text{dipy})(\text{tpht})]\cdot\text{H}_2\text{O}\}_n$ (Table I and Fig. S-1 of the Supplementary material to this paper). The structural characterization of each phase was performed by the Rietveld method according to the known crystal structures of $[\text{Mn}(\text{dipy})(\text{H}_2\text{O})_4](\text{tpht})$ and $\{[\text{Zn}(\text{dipy})(\text{tpht})]\cdot\text{H}_2\text{O}\}_n$ determined from the single crystal data.^{17,18} The quantitative analysis showed that $[\text{Mn}(\text{dipy})(\text{H}_2\text{O})_4](\text{tpht})$: $\{[\text{Zn}(\text{dipy})(\text{tpht})]\cdot\text{H}_2\text{O}\}_n$ phase-mass ratio was 31:69. The Rietveld refinement results (Tables I and S-I (Supplementary material)) displayed a minor deviation from the final structural parameters measured in the original structures.^{17,18}

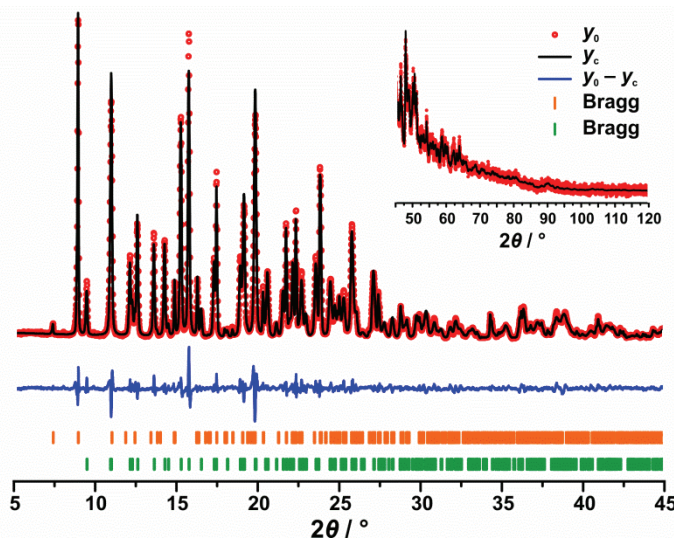


Fig. 1. Two-phased Rietveld refinement pattern of **I**. The Bragg positions of the $[\text{Mn}(\text{dipy})(\text{H}_2\text{O})_4](\text{tpht})$ and $\{[\text{Zn}(\text{dipy})(\text{tpht})]\cdot\text{H}_2\text{O}\}_n$ phases are denoted by orange and green dashes, respectively.

TABLE I. Structural and fitting parameters obtained by Rietveld refinement for **I**

Phase	$[\text{Mn}(\text{dipy})(\text{H}_2\text{O})_4](\text{tpht})$	$\{[\text{Zn}(\text{dipy})(\text{tpht})]\cdot\text{H}_2\text{O}\}_n$
Crystal system	Monoclinic	Monoclinic
Space group	$P2_1/c$	$P2_1/n$
$a / \text{\AA}^*$	7.62706(8)	9.83335(13)
$b / \text{\AA}$	23.8574(2)	14.40389(15)
$c / \text{\AA}$	11.09296(19)	12.27168(15)
$\beta / {}^\circ$	102.2957(10)	95.7916(9)
$V / \text{\AA}^3$	1972.19(4)	1729.27(4)
$R_B / \%$	2.39	3.15
$R_f / \%$	1.99	3.16
Number of parameters refined		314
$R_{wp} / \%$		5.60
$R_p / \%$		4.28
$R_{exp} / \%$		4.42
χ^2		1.60

The existence of water molecules, dipy and tpht ligands in **I** were confirmed from the FTIR spectrum shown in Fig. S-2 of the Supplementary material. A strong $\nu(\text{O}-\text{H})$ stretching vibration at 3418 cm^{-1} corresponds to the lattice water molecules. Characteristic vibrations of the aromatic ring, $\nu(\text{C}=\text{N})$ and $\nu(\text{C}=\text{C})$, as well as $\nu(\text{N}-\text{H})$ bands, are observed at 1659 , 1483 cm^{-1} and in the

* $1 \text{ \AA} = 0.1 \text{ nm}$

3333–3207 cm⁻¹ region, respectively, confirming the coordination of the dipya ligand. The presence of coordinated tpht caused the appearance of asymmetrical (ν_{as}) and symmetrical (ν_s) COO⁻ vibrations at 1599 and 1385 cm⁻¹, respectively, while the vibrations found at 1639 and 1232 cm⁻¹, respectively, confirmed the presence of non-coordinated tpht ligand. In the fingerprint region, a strong peak positioned at 750 cm⁻¹ is due to the presence of overlapped $\nu(N-H)$ and $\nu(C-H)$ vibrations.²³ A band ascribed to the $\nu(M-O)$ stretching vibration at 413 cm⁻¹ verified the coordination of the water molecules as well as tpht ligands to the metal atom.²⁴

Characterization of composite II

The XRPD pattern of **II**, the calculated pattern, as well as the difference profile, are shown in Fig. 2. The Rietveld refinement revealed the coexistence of ZnO, which crystallizes in a hexagonal wurtzite structure and *P6₃mc* space group, and ZnMn₂O₄, which crystallizes in a tetragonal spinel structure and *I4₁/amd* space group. The quantitative phase fraction analysis revealed 62 mass % of ZnO phase and 38 mass % of ZnMn₂O₄ phase. The refined unit cell parameters (Table II) are in good agreement with PDF cards #36-1451 and #24-1123 for ZnO and ZnMn₂O₄ phases, respectively. The reliability factors of less than 5 % (Table II) pointed out that the experimental and calculated data are in good agreement. The calculated values of $\langle D \rangle$ for ZnO phase were similar in all directions meaning that its crystallites were almost spherical (Table II). The corresponding value for ZnMn₂O₄ phase along the *c*-axis was almost two times smaller than along *a*- and *b*-axes implying elongated crystallites of ZnMn₂O₄.

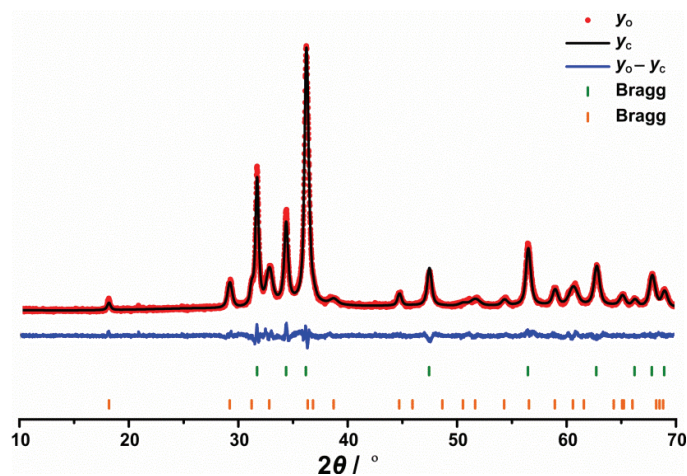


Fig. 2. Two-phase Rietveld refinement pattern of **II**. The Bragg positions of the ZnO and ZnMn₂O₄ phases are denoted by green and orange dashes, respectively.

The FTIR spectrum of **II** is presented in Fig. 3. The broad bands positioned at 611 and 483 cm⁻¹ were ascribed to Mn–O stretching vibrations of MnO₆ octahedron, whereas the weak peaks observed in the region 424–402 cm⁻¹ may be due to the presence of Zn–O bonds in ZnO₄ tetrahedral group.^{25,26}

TABLE II. Structural and fitting parameters obtained by Rietveld refinement for **II**

Phase	ZnO	ZnMn ₂ O ₄
Crystal system	Hexagonal	Tetragonal
Space group	<i>P</i> 6 ₃ <i>mc</i>	<i>I</i> 4 ₁ / <i>amd</i>
<i>a</i> / Å	3.2574(1)	5.7299(3)
<i>c</i> / Å	5.2175(2)	9.3000(8)
<i>V</i> / Å ³	47.945(3)	305.34(3)
< <i>D</i> > / nm	26.5 [0,0,1]; 30.8 [-0.356,-0.935,0] 30.8 [0.935,-0.356,0]	19.5 [0,0,1] 36.9 [-0.356,-0.935,0] 36.9 [0.935,-0.356,0]
Number of parameters refined	39	
<i>R</i> _{wp} / %	4.80	
<i>R</i> _d / %	3.82	
<i>R</i> _{exp} / %	3.80	
<i>S</i>	1.2633	
<i>χ</i> ²	1.5960	

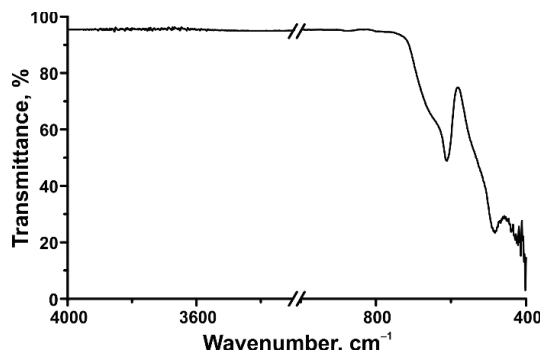


Fig. 3. FTIR spectrum of **II**.

The FESEM micrographs of **II** are presented in Fig. 4. The powder is composed of deformed spherical nanoparticles of ZnO phase and the elliptical particles of ZnMn₂O₄ phase, which is in agreement with the results found by XRPD analysis. The FESEM micrograph made at higher magnification (Fig. 4b) shows that the particles of both phases have smooth surfaces with an average diameter of about 67 nm for ZnO phase and with average width and length of 156 and 290 nm, respectively, for ZnMn₂O₄ phase.

Zeta potential is very important for the stability of colloidal dispersions. In general, dividing line between stable and unstable dispersions is taken at ±30 mV. Particles with absolute zeta potentials higher than 30 mV are mainly considered stable.²⁷ The mean particle size was found to be (445.6±53.1) nm. This

can be explained by the formation of agglomerates which was also observed by FESEM. The value of zeta potential was (-7.80 ± 0.86) mV, indicating that particles of **II** carried the negative surface charge and that colloidal dispersion is unstable. The estimated *PDI* was high with a value of 0.347 ± 0.100 , implying non-uniform dispersion of **II** during dyeing.^{28–30}

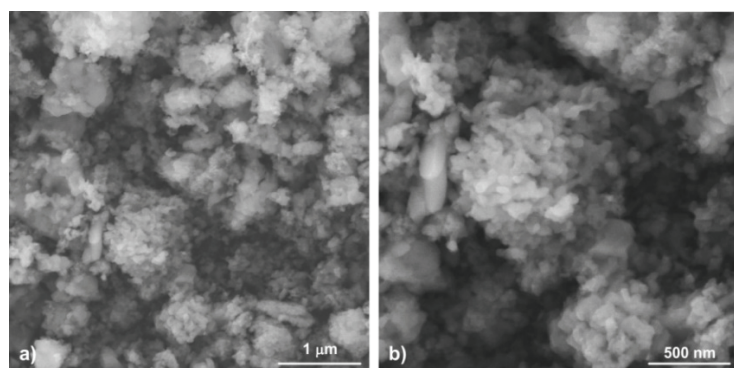


Fig. 4. FESEM images of **II** at different magnifications.

The results of the BET analysis of **II** are presented in Table III and Fig. 5. The value of *SSA* is small, being equal to $16.95 \text{ m}^2 \text{ g}^{-1}$, while the average pore size was estimated to be 23.3 nm (Table III). Up to $p/p_0 = 0.8$, the slope of the N_2 adsorption/desorption isotherms of **II** is small due to the presence of a little number of small size pores (Fig. 5a). A slight separation of the adsorption and desorption isotherms of **II** was observed in the region 0.8–1 at p/p_0 axis, meaning that the quantity of micropores is also small, which further implied that pores were a consequence of the voids between the nanoparticles. The small *SSA* value of **II** denoted that composite could be uneven and weakened in colouring strength.³¹

TABLE III. The results of BET analysis of **II**; V_{tot} – total pore volume; V_{meso} – mesopore volume; V_{micro} – micropore volume; D_{aver} – average pore diameter; D_{max} – the diameter of the pores that occupy the largest part of the volume

$SSA / \text{m}^2 \text{ g}^{-1}$	$V_{\text{tot}} / \text{cm}^3 \text{ g}^{-1}$	$V_{\text{meso}} / \text{cm}^3 \text{ g}^{-1}$	$V_{\text{micro}} / \text{cm}^3 \text{ g}^{-1}$	$D_{\text{aver}} / \text{nm}$	$D_{\text{max}}^{\text{a}} / \text{nm}$
16.95	0.0813	0.0772	0.0048	23.3	23.5 and 34.7

^aTwo maxima exist on the curve

The energy band gap (E_g) values for **II** were calculated from the plot of the modified Kubelka–Munk function ($F(R)h\nu)^2$ vs. the energy of the adsorbed light ($h\nu$) using the linear fits close to the absorption edge as it is shown in Fig. 6a. The absorption spectra exhibited double absorption edges and two different E_g values were determined: one at 2.4 eV and another at 3.3 eV. A lower E_g value could be ascribed to d–d transitions and the dark colour of **II**, as it is already observed for samples with a high concentration of TM in the structure, while a

higher E_g value could be due to an increase in the intensity of TM–O²⁻ charge transfer.³² The steady-state emission spectrum of **II** obtained at room temperature is presented in Fig. 6b. Upon excitation at 350 nm, this analysis revealed a band centred at 422 nm in the blue region of the visible part of the spectrum followed by low or negligible absorption in the red and orange region, which is associated with the brown colour of **II**.³²

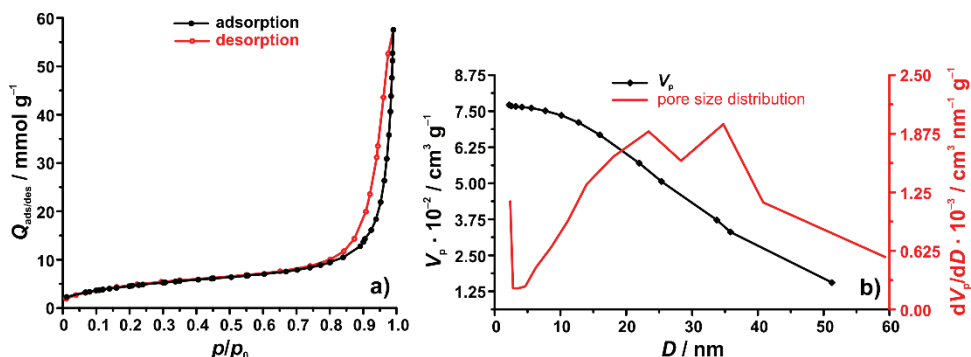


Fig. 5. Adsorption–desorption curves (a) and pore volume and pore size distribution (b) for **II**.

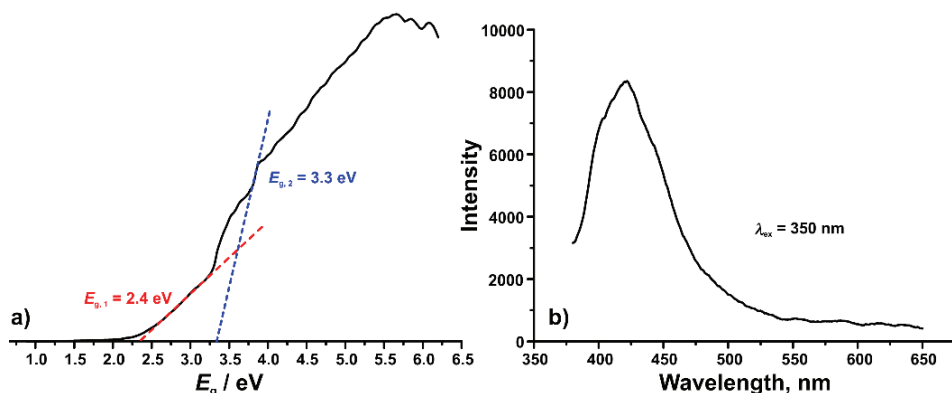


Fig. 6. Direct band gap energies (a) and the emission spectrum (b) of **II**.

The composite **II** is tested for application as a pigment for colouring the ceramic glaze. The transparent glaze is obtained from a glass frit containing a high quantity of SiO₂, and a high SiO₂/Al₂O₃ ratio (Table IV).

The low quantity of lead and absence of cadmium shows that the glaze is not toxic to living organisms.³³ The pigment material **II** was of a brownish–black colour with a value of L^* being 26.85 (Table V, Fig. 7a) and with a^* and b^* coordinates similar to other materials with spinel structure used as pigments.^{6,32} The dark pigment decreased the lightness of the glaze by about 37 %, whereas, at the same time, redness and yellowness increased. In both transparent and pig-

mented glazes, a smooth surface is obtained (Fig. 7b–c and Fig. S-3 of the Supplementary material). The unevenness of the pigment distribution may be caused by an insufficient quantity of the pigment particles that grouped and spread over the transparent glaze during the sintering process. In addition, unevenness of the pigment **II** is in accordance with its small value of *SSA* (Table III), high *PDI* and zeta potential close to zero.

TABLE IV. Chemical composition of the ceramic glass used for glazing; *LOI* – loss on ignition

Component	Share, %	Component	Share, %
<i>LOI</i>	3.47	SO ₃	0.04
SiO ₂	62.16	P ₂ O ₅	0.06
Al ₂ O ₃	15.76	MnO	0.00
Fe ₂ O ₃	0.19	TiO ₂	0.06
CaO	9.84	Pb	0.03
MgO	0.46	Cd	0.00
Na ₂ O	6.00	Ba	0.89
K ₂ O	0.92	Sum	99.87

TABLE V. CIE *L***a***b** colorimetric coordinates of the pigment **II** and glazes

Sample	<i>L*</i>	<i>a*</i>	<i>b*</i>
II	26.85	2.94	4.96
Transparent glaze	64.88	2.60	15.38
Pigmented glaze	40.70	11.26	22.04

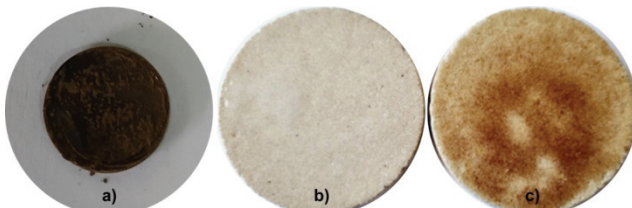


Fig. 7. The appearance of the pigment **II** (a), transparent (b) and pigmented glazed ceramics (c).

The advantages of composite materials considered as not harmful to health may make these glazes promising and widely used on surfaces where glazed ceramics come into contact with food or chemicals.³⁴

CONCLUSION

Direct solid-state decomposition of terephthalate precursor **I**, composed of 31 mass % of [Mn(dipy)(H₂O)₄](tpht) and 69 mass % of {[Zn(dipy)(tpht)]·H₂O}_n, gave as result the nanocrystalline ZnO/ZnMn₂O₄ brown composite material, **II**, with phase mass ratio of 68:32 for ZnO:ZnMn₂O₄. Rietveld structure refinement results revealed the presence of wurtzite ZnO and spinel ZnMn₂O₄. Particle size of ZnO phase was about 67 nm, while width and

length of ZnMn₂O₄ particles were about 156 and 290 nm, respectively. The *PDI* of 0.347, small value of *SSA* of 16.95 m² g⁻¹ and zeta potential value of -7.80 mV resulted in unstable pigmentary dispersion of **II** and uneven distribution of pigment during dyeing of transparent ceramic glaze. Since the composite **II** is composed of nontoxic oxides, it is expected to be the environmentally safe for application as pigmentary material in paints, polymers and ceramics.

SUPPLEMENTARY MATERIAL

Additional data and information are available electronically at the pages of journal website: <https://www.shd-pub.org.rs/index.php/JSCS/article/view/12126>, or from the corresponding author on request.

Acknowledgement. This work was supported by the Ministry of Education, Science and Technological Development of the Republic of Serbia (Contract Nos. 451-03-68/2022-14/200287, 451-03-68/2022-14/200135, 451-03-68/2022-14/200012 and 451-03-68/2022-14/200053).

ИЗВОД
СТРУКТУРА И СВОЈСТВА КОМПОЗИТА ZnO/ZnMn₂O₄ ДОБИЈЕНОГ ТЕРМИЧКОМ
РАЗГРАДЊОМ ТЕРЕФТАЛАТ-ПРЕКУРСОРА

ЛИДИЈА РАДОВАНОВИЋ¹, ЈЕЉКО РАДОВАНОВИЋ¹, БОЈАНА СИМОВИЋ², МИЛИЦА В. ВАСИЋ³,
БОЈАНА БАЛАНЧ¹, АЛЕКСАНДРА ДАПЧЕВИЋ⁴, МИРОСЛАВ ДРАМИЋАНИЋ⁵ И ЈЕЛЕНА РОГАН⁴

¹Иновациони центар Технолошко-мештрушки факултет, Универзитет у Београду, Карнегијева 4,
Београд, ²Институт за мултидисциплинарна истраживања, Универзитет у Београду, Кнеза
Вишеслава 1, Београд, ³Институт за истишавање матерijала ИМС, Универзитет у Београду,
Булевар војводе Мишића 43, Београд, ⁴Технолошко-мештрушки факултет, Универзитет у
Београду, Карнегијева 4, Београд и ⁵Институт за нуклеарне науке „Винча“, Универзитет у
Београду, Поштански претпак 522, Београд

Двофазни [Mn(dipyra)(H₂O)₄](tpht)/{[Zn(dipyra)(tpht)]·H₂O}_n комплексни материјал, **I**, (dipyra = 2,2'-дипиридиламин, tpht²⁻ = дијанјон 1,4-бензендикарбоксилне киселине) синтетисан је реакцијом измене лиганада и окарактерисан XRPD методом и FTIR спектроскопијом. Композит ZnO/ZnMn₂O₄, **II**, добијен је термичком разградњом прекурсора **I** у атмосфери ваздуха на 450 °C. XRPD методом, FTIR спектроскопијом и FESEM микроскопијом композита **II** утврђено је истовремено присуство сферних наночестица ZnO вирцитне структуре и издужених наночестица ZnMn₂O₄ са структуром спинела. Специфична површина композита **II** одређена је BET методом, док су запремина и пропечна величина мезопора израчунати у складу са BJH методом. Средња величина, индекс полидисперзије и цета потенцијал измерени су фотонском корелационом спектроскопијом и електрофоретским расејањем светлости и показали су нестабилност композита **II**. Вредности ширине забрањене зоне од 2,4 и 3,3 eV одређене су UV-Vis дифузно-рефлексионом спектроскопијом, док су мерења фотолуминесценције показала да је композит **II** активан у плавој области видљивог дела спектра. Испитивање композита **II** као пигментног материјала показало је да се може користити за бојење керамичке глазуре.

(Примљено 2. новембра, ревидирано 17 децембра, прихваћено 21. децембра 2022)

REFERENCES

1. C. Yuan, H. B. Wu, Y. Xie, X. W. Lou, *Angew. Chem. Int. Ed.* **53** (2014) 1488 (<https://dx.doi.org/doi: 10.1002/anie.201303971>)
2. C. N. R. Rao, B. Raveau, *Transition Metal Oxides: Structure, Properties, and Synthesis of Ceramic Oxides*, 2nd ed., Wiley-VCH, New York, 1998 ([https://doi.org/10.1002/\(SICI\)1099-0739\(199906\)13:6<476::AID-AOC851>3.0.CO;2-N](https://doi.org/10.1002/(SICI)1099-0739(199906)13:6<476::AID-AOC851>3.0.CO;2-N))
3. A. Kołodziejczak-Radzimska, T. Jesionowski, *Materials* **7** (2014) 2833 (<https://dx.doi.org/10.3390/ma7042833>)
4. G. D. Park, Y. C. Kang, J. S. Cho, *Nanomaterials* **12** (2022) 680 (<https://doi.org/10.3390/nano12040680>)
5. M. Fortuño-Morte, P. Serna-Gallén, H. Beltrán-Mir, E. Cordoncillo, *J. Mat.* **7** (2021) 1061 (<https://doi.org/10.1016/j.jmat.2021.02.002>)
6. T. E. R. Fiuza, D. Göttert, L. J. Pereira, S. R. M. Antunes, A. V. C. de Andrade, A. C. Antunes, É. C. F. de Souza, *Process. Appl. Ceram.* **12** (2018) 319 (<https://doi.org/10.2298/PAC1804319R>)
7. G. Pfaff, *Phys. Sci. Rev.* **7** (2022) 7 (<https://doi.org/10.1515/psr-2020-0183>)
8. G. Osmond, *AICCM Bull.* **33** (2012) 20 (<http://dx.doi.org/10.1179/bac.2012.33.1.004>)
9. L. J. Almeidaa, E. C. Grzebieluckaa, S. R. M. Antunesa, C. P. F. Borgesa, A. V. C. de Andradeb, É. C. F. de Souza, *Mat. Res.* **23** (2020) e20190515 (<https://doi.org/10.1590/1980-5373-MR-2019-0515>)
10. T. R. Cook, Y. R. Zheng, P. J. Stang, *Chem. Rev.* **113** (2013) 734 (<https://doi.org/10.1021/cr3002824>)
11. D. Sun, R. Cao, Y. Liang, Q. Shi, W. Sua, M. Hong, *J. Chem. Soc., Dalton Trans.* (2001) 2335 (<https://doi.org/10.1039/B102888J>)
12. Z. Cheng, H. Shi, H. Ma, L. Bian, Q. Wu, L. Gu, S. Cai, X. Wang, W. Xiong, Z. An, W. Huang, *Angew. Chem. Int. Ed.* **57** (2018) 678 (<https://doi.org/10.1002/anie.201710017>)
13. C. R. Groom, I. J. Bruno, M. P. Lightfoot, S. C. Ward, *Acta Crystallogr., B* **72** (2016) 171 (<https://doi.org/10.1107/S2052520616003954>)
14. H. Lu, D. S. Wright, S. D. Pike, *Chem. Commun.* **56** (2020) 854 (<https://doi.org/10.1039/C9CC06258K>)
15. M. Y. Masoomi, A. Morsali, *Coord. Chem. Rev.* **256** (2012) 2921 (<https://doi.org/10.1016/j.ccr.2012.05.032>)
16. L. Radovanović, J. D. Zdravković, B. Simović, Ž. Radovanović, K. Mihajlovski, M. D. Dramićanin, J. Rogan, *J. Serb. Chem. Soc.* **85** (2020) 1475 (<https://doi.org/10.2298/JSC200629048R>)
17. L. Radovanović, J. Rogan, D. Poleti, M. V. Rodić, N. Begović, *Inorg. Chim. Acta* **445** (2016) 46 (<https://doi.org/10.1016/j.ica.2016.02.026>)
18. L. Radovanović, J. Rogan, D. Poleti, M. Milutinović, M. V. Rodić, *Polyhedron* **112** (2016) 18 (<https://dx.doi.org/10.1016/j.poly.2016.03.054>)
19. H. M. Rietveld, *J. Appl. Cryst.* **2** (1969) 65 (<https://doi.org/10.1107/S0021889869006558>)
20. J. Rodríguez-Carvajal, *Newsletter* **26** (2001) 12 (<http://journals.iucr.org/iucr-top/comm/cpd/Newsletters/>)
21. M. V. Vasić, L. Pezo, M. R. Vasić, N. Mijatović, M. Mitrić, *Bol. Soc. Esp. Ceram. V.* (2020) (<https://doi.org/10.1016/j.bsecv.2020.11.006>)
22. C. Molinari, S. Conte, C. Zanelli, M. Ardit, G. Cruciani, M. Dondi, *Ceram. Int.* **46** (2020) 21839 (<https://doi.org/10.1016/j.ceramint.2020.05.302>)
23. E. Castellucci, L. Angeloni, N. Neto, G. Sbrana, *Chem. Phys.* **43** (1979) 365 ([https://doi.org/10.1016/0301-0104\(79\)85204-0](https://doi.org/10.1016/0301-0104(79)85204-0))

24. K. Nakamoto, *Infrared and Raman Spectra of Inorganic and Organic Coordination Compounds*, Part B, 5th ed., Wiley-Interscience, New York, 1997
25. N. Senthilkumar, V. Venkatachalam, M. Kandiban, P. Vigneshwaran, R. Jayavel, Vetha Potheher, *Physica E* **106** (2019) 121 (<https://doi.org/10.1016/j.physe.2018.10.027>)
26. W. Konicki, D. Siber, U. Narkiewicz, *Separ. Sci. Technol.* **53** (2018) 1295 (<https://doi.org/10.1080/01496395.2018.1444054>)
27. Holmberg, D. O. Shah, M. J. Schwuger, *Handbook of Applied Surface and Colloid Chemistry*, Vol. 2, John Wiley & Sons, Ltd., Chichester, 2002
28. R Greenwood, K Kendall, *J. Eur. Ceram. Soc.* **19** (1999) 479 ([http://dx.doi.org/10.1016/S0955-2219\(98\)00208-8](http://dx.doi.org/10.1016/S0955-2219(98)00208-8))
29. M. Staiger, P. Bowen, J. Ketterer, J. Bohonek, *J. Disper. Sci. Technol.* **23** (2002) 619 (<https://doi.org/10.1081/DIS-120015367>)
30. Nie, G. Chang, R. Li, *Coatings* **20** (2020) 741 (<https://doi.org/10.3390/coatings10080741>)
31. H. Morii, K. Hayashi, K. Iwasaki, (Hiroshima-shi, Hiroshima-ken (JP)), EP 1 686 158 B1 (2006)
32. E. A. Medina, J. Li, M. A. Subramanian, *Prog. Solid State Chem.* **45–46** (2017) 9 (<https://doi.org/10.1016/j.progsolidstchem.2017.02.002>)
33. SRPS EN ISO 10545-15: *Ceramic tiles — Part 15: Determination of lead and cadmium given off by glazed tiles*, 2012
34. J. W. Gallaway, M. Menard, B. Hertzberg, Z. Zhong, M. Croft, L. A. Sviridov, D. E. Turney, S. Banerjee, *J. Electrochem. Soc.* **162** (2015) A162 (<https://doi.org/10.1149/2.0811501jes>).

SUPPLEMENTARY MATERIAL TO

Structure and properties of ZnO/ZnMn₂O₄ composite obtained by thermal decomposition of terephthalate precursor

LIDIJA RADOVANOVIĆ^{1*}, ŽELJKO RADOVANOVIĆ^{1#}, BOJANA SIMOVIĆ^{2#},
MILICA V. VASIĆ³, BOJANA BALANČ¹, ALEKSANDRA DAPČEVIĆ^{4#},
MIROSLAV DRAMIĆANIN⁵ and JELENA ROGAN^{4#}

¹Innovation Centre of the Faculty of Technology and Metallurgy, University of Belgrade,

Karnegijeva 4, Belgrade, Serbia, ²Institute for Multidisciplinary Research, University of Belgrade, Kneza Višeslava 1, Belgrade, Serbia, ³Institute for Testing of Materials IMS,

University of Belgrade, Bulevar vojvode Mišića 43, Belgrade, Serbia, ⁴Faculty of

Technology and Metallurgy, University of Belgrade, Karnegijeva 4, Belgrade, Serbia and

⁵Vinča Institute of Nuclear Sciences, University of Belgrade, I.P.O. Box 522, Belgrade, Serbia

J. Serb. Chem. Soc. 88 (3) (2023) 313–325

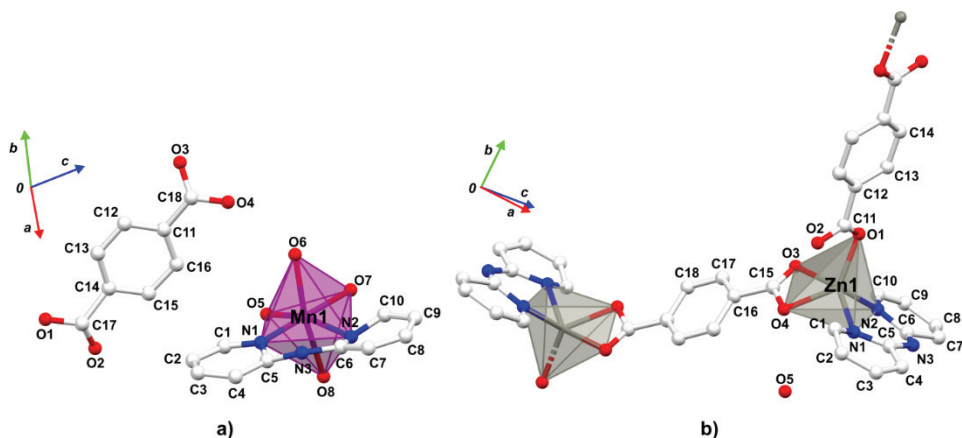


Fig. S-1. The asymmetric unit of $[\text{Mn}(\text{dipyra})(\text{H}_2\text{O})_4](\text{tpht})$ phase (a) and the structural fragment of $\{[\text{Zn}(\text{dipyra})(\text{tpht})]\cdot\text{H}_2\text{O}\}_n$ phase (b) in I.

* Corresponding author. E-mail: lradovanovic@tmf.bg.ac.rs

TABLE S-I. Selected bond lengths (\AA) for $[\text{Mn}(\text{dipy})\text{(H}_2\text{O)}_4]\text{(tpht)}$ and $\{[\text{Zn}(\text{dipy})\text{(tpht)}]\cdot\text{H}_2\text{O}\}_n$ phases in **I**

Phase	Bond	Bond length, \AA^*
$[\text{Mn}(\text{dipy})\text{(H}_2\text{O)}_4]\text{(tpht)}$	Mn1–N1	2.217(14)
	Mn1–N2	2.356(18)
	Mn1–O5	2.23(3)
	Mn1–O6	2.22(4)
	Mn1–O7	2.23(4)
	Mn1–O8	2.44(5)
$\{[\text{Zn}(\text{dipy})\text{(tpht)}]\cdot\text{H}_2\text{O}\}_n$	Zn1–N1	2.153(14)
	Zn1–N2	2.062(8)
	Zn1–O1	2.029(18)
	Zn1–O3	2.408(15)
	Zn1–O4	2.060(16)

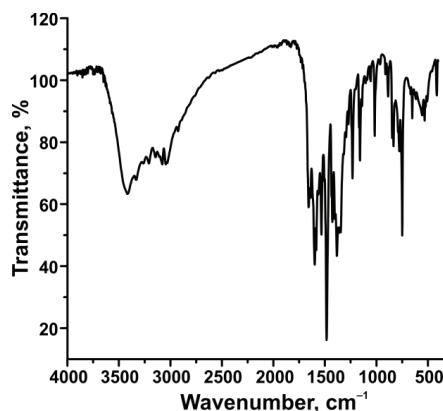


Fig. S-2. FTIR spectrum of **I**.

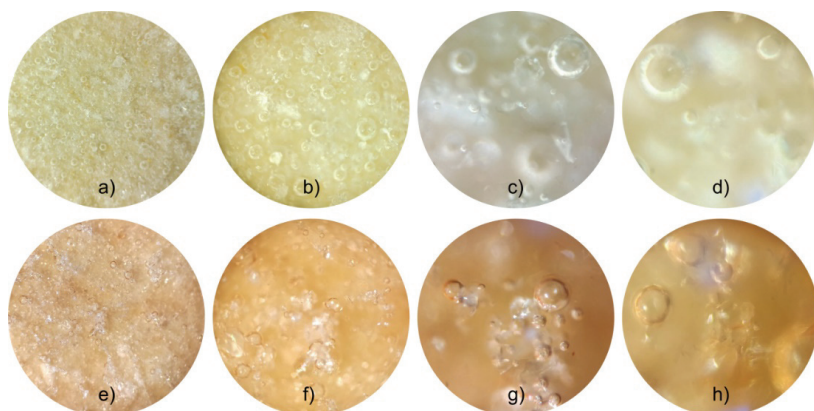


Fig. S-3. Transparent (a–d) and pigmented (e–h) glaze at different magnifications: 40 \times (a, e), 100 \times (b, f), 200 \times (c, g) and 400 \times (d, h).

* 1 \AA = 0.1 nm



Powdered adsorbent obtained from bathurst burr biomass for methylene blue removal from aqueous solutions

GIANNIN MOSOARCA¹, COSMIN VANCEA^{1*}, SIMONA POPA^{1**},
MARIA ELENA RADULESCU-GRAD² AND SORINA BORAN¹

¹Politehnica University Timisoara, Faculty of Industrial Chemistry and Environmental Engineering, Bd. V. Parvan, No. 6, 300223, Timisoara, Romania and ²"Coriolan Dragulescu" Institute of Chemistry, Romanian Academy, Mihai Viteazu Bd. No. 24, 300223 Timisoara, Romania

(Received 16 March, revised 30 April, accepted 4 May 2022)

Abstract: Powdered adsorbent obtained from bathurst burr biomass was tested for methylene blue removal from aqueous solutions. SEM and FTIR analyses were used to characterize the adsorbent before and after adsorption. The influence of contact time, adsorbent dose, pH, initial dye concentration, ionic strength and temperature on the process were investigated. Kinetic, equilibrium and thermodynamic studies were conducted to analyse the process. The Taguchi method was used to establish the most suitable conditions for the dye adsorption. The process is spontaneous, favourable, and exothermic and the Freundlich isotherm and pseudo-second order kinetic model best describe it. The Taguchi method indicate that the ionic strength is the factor with the greatest influence on the adsorption process.

Keywords: low-cost adsorbent; dye adsorption; kinetic; equilibrium; thermodynamic; Taguchi method.

INTRODUCTION

Methylene blue is a thiazine cationic dye used in various fields and activities. It is widely used in the textile industry for dyeing cotton, wood, and silk due to its ease of application, good material resistance and economic benefits. In medicine it is used to treat methemoglobinemia, cyanide poisoning and urinary tract infections. It is also used as a colouring agent in diagnostic examination and surgery. Even if not strongly hazardous, the methylene blue can have negative effects on humans causing eye irritation, breathing difficulty, nausea, heart-beat increase, vomiting, diarrhea and jaundice. To avoid harmful impacts on aquatic

*,** Corresponding authors. E-mail: (*)cosmin.vancea@upt.ro; (**)simona.popa@upt.ro
<https://doi.org/10.2298/JSC220316039M>

life and human health, the dye should be removed from wastewater before their discharging into natural effluents.^{1–5}

Scientific literature mentions many physicochemical and biological methods designed to remove the methylene blue dye from aqueous solutions: adsorption, coagulation, flocculation, ion exchange, precipitation, oxidation, chemical precipitation, electrochemical processes, photocatalytic processes, membrane processes and biodegradation. Very often, adsorption is the chosen process for dye retention due to its many advantages such as: simplicity, high efficiency, flexibility and low costs. An important number of adsorbents are known, among which an important role is played by natural materials that are cheap and available in large quantities.^{1–10}

Bathurst Burr (*Xanthium spinosum*) is a very invasive plant widespread in Europe, North America, Asia, Australia and partly in Africa. It has a very high resistance to drought, pollution and, in general, to any aggressive environmental conditions. It grows up to one meter tall and has a branched stem full of thorns. It can be found in lowland, hilly and low mountain areas, on pastures, abandoned land and roadsides. Due to its anti-inflammatory, disinfectant, diuretic, antidiabetic and antitumor properties, is used in traditional medicine.^{11,12}

The purpose of this study was to use the bathurst burr powder to remove the methylene blue dye from aqueous solutions by adsorption. The effect of contact time, adsorbent dose, pH, initial dye concentration, ionic strength and temperature on the adsorption process were monitored. Kinetic, equilibrium and thermodynamic studies were used to analyse the process. In order to establish the most suitable conditions for the dye adsorption, the process was optimized by the Taguchi method.

EXPERIMENTAL

The adsorbent material was obtained from the aerial part of bathurst burr mature plants, which were purchased from StefMar SRL, a local company that process and pack medicinal and aromatic plants. The adsorbent powder obtaining process was described elsewhere.¹³ The characteristics of adsorbent material, before and after adsorption, were examined by SEM analysis (Quanta FEG 250 scanning electron microscope at 1600 \times magnitude) and FTIR spectroscopy (Shimadzu Prestige-21 FTIR spectrophotometer). The point of zero charge (pH_{PZC}) was determined using the solid addition method.³

In the adsorption studies the influence of pH, adsorbent dose, dye concentration, time, temperature, and ionic strength was studied. Three independent replicates were performed for each test. During the experiments a constant mixing intensity was maintained. The pH was adjusted using NaOH and HCl solutions (0.1 M). NaCl as background electrolyte was used to study the effect of ionic strength. The methylene blue concentration was determined using a UV–Vis spectrophotometer at 664 nm wavelength.

The equilibrium and kinetics studies were assessed using the nonlinear equations of the Langmuir, Freundlich and Temkin isotherms and also, the nonlinear equations of the pseudo first-order, pseudo second-order and Elovich kinetic models.^{14–17} Each of these isotherm and kinetic models were evaluated through the statistical parameters determination coefficient

(R^2), sum of square error (SSE), chi-square (χ^2) and average relative error (ARE).¹⁷ The higher value for R^2 and the lower value for SSE , χ^2 and ARE were used as the criterion for determining the most suitable model.

The Taguchi method was used to optimize the dye removal experimental conditions. The L27 orthogonal array experimental design was employed to establish the influence of six controllable factors on methylene blue removal. Table I shows these factors and their levels. The Taguchi method evaluates the experimental results by signal-to-noise (S/N) ratio, defining the measurement of the response deviation from the desired value.¹⁸⁻²⁰ “The larger the better” option was used to maximize the S/N ratio and implicitly the highest dye removal efficiency. All calculations were performed with the Minitab 19 Software.

TABLE I. Controllable factors and their levels

Factor	Level 1	Level 2	Level 3
Time, min	1	10	30
Adsorbent dose, mg L ⁻¹	0.5	1.5	3.0
pH	2	6	10
Initial dye concentration, mg L ⁻¹	50	150	250
Ionic strength, mol L ⁻¹	0	0.1	0.2
Temperature, K	284	291	315

RESULTS AND DISCUSSION

Adsorbent surface characterization

Fig. 1 shows the SEM images of the adsorbent material surface at 3000 \times magnitude. Before adsorption, the adsorbent surface has a porous aspect, suitable for dye adsorption (Fig. 1A).

After adsorption, the surface morphology has changed (Fig. 1B), indicating that pores, voids, or irregularities might be filled with the dye molecules.

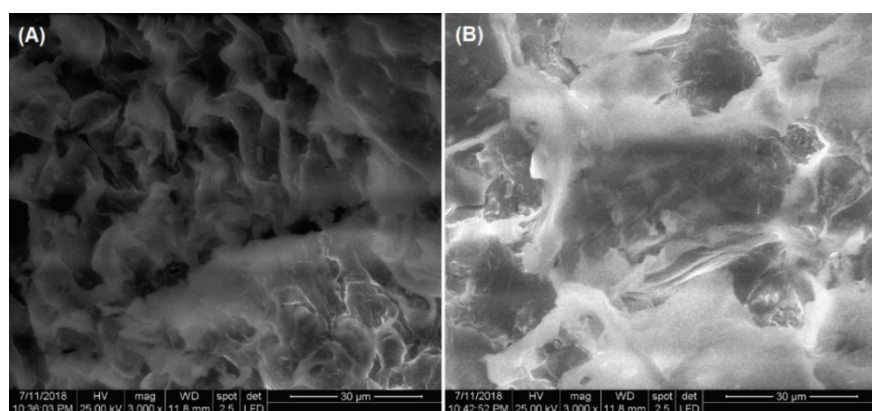


Fig. 1. SEM images of adsorbent surface: A) before and B) after adsorption.

The FTIR spectrum of adsorbent, depicted in Fig. 2, indicates that main components of bathurst burr powder are cellulose, hemicellulose, and lignin. The

identified peaks of the functional groups characteristic of these components are: 3448 cm^{-1} corresponds to O–H stretching of cellulose, Senthamarai Kannan *et al.*²¹ found this peak in the spectra of natural cellulosic fibre from bark of *Albizia amara*; 2340 and 1630 cm^{-1} indicate O–H bending of adsorbed water, Tsuboi²² identifying both peaks in FTIR spectra of cellulose extracted from natural flax, ramie and cotton fibres and Karimi *et al.*²³ found the second peak in cellulose spectrum isolated from kenaf fibres; 2053 cm^{-1} – can be assigned to NCO from isocyanate groups, presence of this functional group being reported Salim *et al.*²⁴ in the lignin spectra extracted from bark of *Leucaena leucocephala*; 1368 cm^{-1} corresponds to C–H bending vibration in cellulose and hemicellulose, Labbe *et al.*²⁵ and Kubovský *et al.*²⁶ found this peak in spectra of aspen tree bark and oak wood respectively; 1000 cm^{-1} indicate C–O stretching, Liang and Marchessault²⁷ identifying this peak in FTIR spectra of native cellulose; 542 cm^{-1} can be attributed to C–H bend, Salim *et al.*²⁴ found this band in the spectra of lignin extracted from native *Leucaena leucocephala* bark.

After absorption, the FTIR spectrum does not show significant differences compared to the one recorded before adsorption, which indicates that physical interactions are implied in the adsorption process.^{8,13}

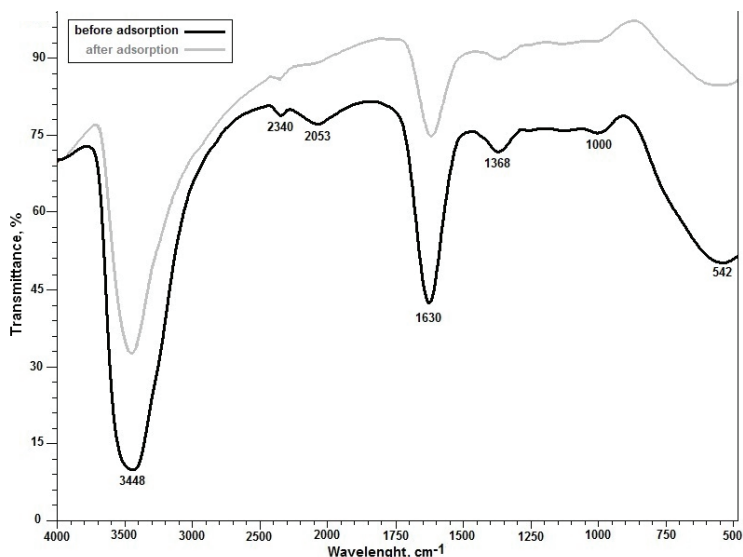


Fig. 2. FTIR spectra of adsorbent before and after dye adsorption.

The point of zero charge provides information on how an adsorbate will be adsorbed by an adsorbent material depending on the surface electrical charge.

If the solution pH is higher than pH_{PZC}, the adsorbent surface is negatively charged while a solution pH lower than pH_{PZC} leads to a positively charged ads-

orbent surface. Therefore, the adsorption of methylene blue will be favoured when the pH of the solution is higher than pH_{PZC} . The value of this parameter, determined using solid addition method, was 6.64 (Fig. 3).

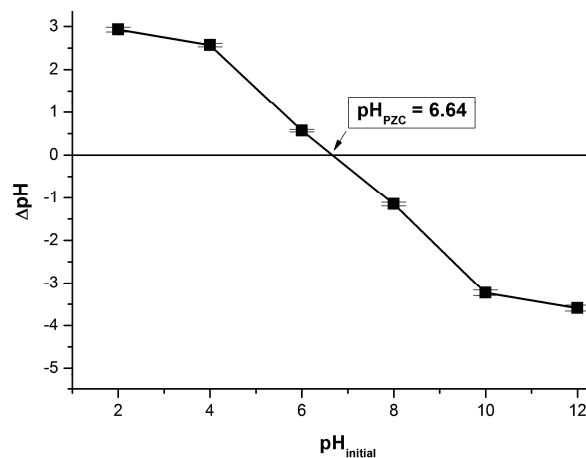


Fig. 3. Determination of point of zero charge (pH_{PZC}) based on the solid addition method.

The influence of contact time on adsorption process

In the first few minutes, the adsorption process is fast (Fig. 4) because many active adsorption sites are available on the surface of the material.^{6,7,10} As time goes on, these sites gradually take over and the adsorption capacity increases more slowly. After 30 min the equilibrium is reached, indicating that all the surface of the adsorbent is covered by dye molecules.^{6,7}

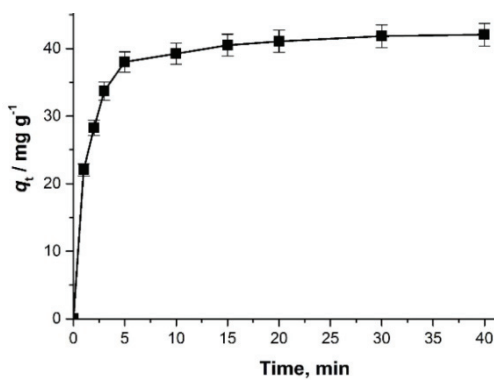


Fig. 4. Influence of contact time on adsorption capacity.

The equilibrium times obtained for similar adsorbents used for methylene blue removal from water were: 30 min for *Arthrosphaera platensis* biomass,²⁸ 50 min for *Haloxylon recurvum* stem biomass,²⁹ 60 min for *Euchema Spinosum* alga biomass³⁰ and 90 min for *Phragmites australis* biomass.³¹

The influence of adsorbent dose on adsorption process

The adsorbent dose influence upon the adsorption capacity together with the methylene blue removal efficiency are presented in Fig. 5. The two parameters behave differently as the adsorbent dose increases: the adsorption capacity decreases while the dye removal efficiency increases. At high adsorbent amounts the aggregation of particles can occur, and a large part of the active sites remains unsaturated. These two phenomena lead to a decrease of the adsorption capacity.^{7,9,10} The positive effect of a larger adsorbent quantity upon the removal efficiency is based on an increase of the surface area and thus of the number of sites available for adsorption.^{3,7,9} Similar observations have been reported in other studies on the methylene blue adsorption on other low-cost plant materials. When *Salix babylonica* leaves were used as adsorbent, an increase in adsorbent material dose from 0.2 to 15 g L⁻¹ led to an increase in dye removal efficiency of 36.88 % and a decrease in adsorption capacity of 98 %.⁷ In the case of citrus limetta peel use, it was observed that for an increase of the adsorbent dose from 0.4 to 2.0 g L⁻¹, removal efficiency increased rapidly by about 3 % while the adsorption capacity decreased by 91 %.¹⁰

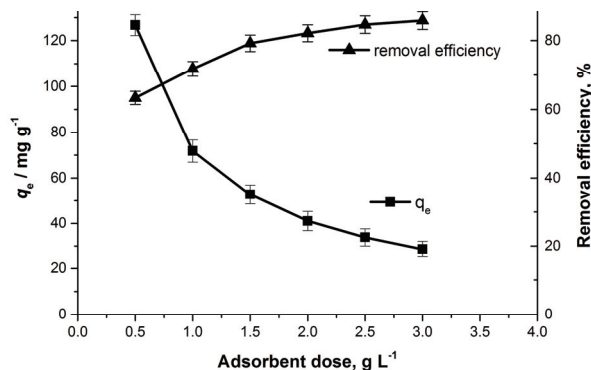


Fig. 5. Influence of adsorbent dose on adsorption capacity and removal efficiency.

The influence of pH on adsorption process

The effect of solution pH on adsorption capacity is depicted in Fig. 6. Increasing the value of this parameter has a positive effect on the adsorption capacity. The best results were obtained at a pH higher than 8. At these pH values, higher than the pH corresponding to the point of zero charge (pHpzc 6.64), the adsorbent material surface is negatively charged, favouring the electrostatic attraction with the dye cations.^{3,10,32} Similar results were reported in other previous articles publish in scientific literature. At pH > 8, increased adsorption capacities were recorded for adsorbent materials such as: *Salix babylonica* leaves,⁷ citrus limetta peel,¹⁰ *Phragmites australis* biomass³¹ and phoenix tree's leaves.³³

The relatively constant value of adsorption capacity at high pH indicates that in addition to the electrostatic attraction, other mechanisms are also involved in the adsorption process.³²

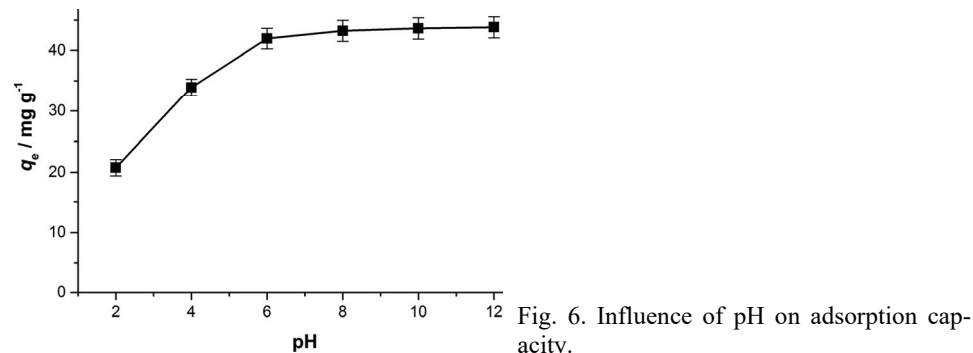


Fig. 6. Influence of pH on adsorption capacity.

The influence of initial dye concentration on adsorption process

The adsorption capacity and the dye removal efficiency values at different initial dye concentrations are shown in Fig. 7. The adsorption capacity increases while the dye removal efficiency decreases as the initial dye concentration increases. The first parameter behaviour is caused by the increase of the driving force resulting from the concentration gradient.^{32,33} The values of the second parameter decrease due to the accumulation of methylene blue molecules on the surface of the adsorbent which leads to saturation of the adsorption sites.^{6,28} Similar behaviours have been mentioned previously in other adsorption studies. Our study shows that an increase of the initial dye concentration from 50 to 200 mg L⁻¹ leads to an increase of the adsorption capacity from 21.7 to 83.5 mg g⁻¹ and a decrease of dye removal efficiency from 87.18 to 83.19 % respectively. For the same initial dye concentration variation range, other researchers reported an

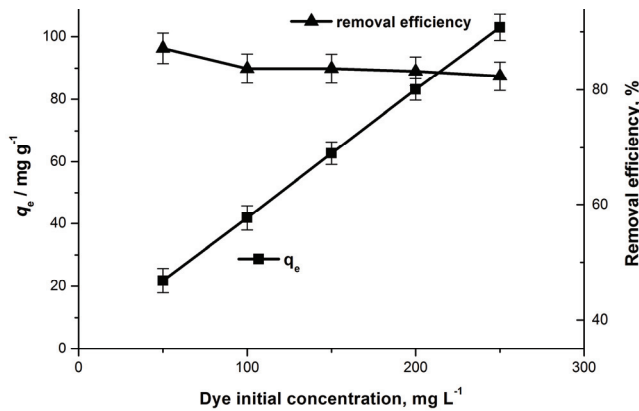


Fig. 7. Influence of dye initial concentration on adsorption capacity and removal efficiency.

increase in adsorption capacity from about 24 to 80 mg g⁻¹ and a decrease dye removal efficiency from 96 to 92 % when using weeping willow leaves⁷ as an adsorbent. Another study using *A. platensis* biomass²⁸ as adsorbent, an increase of the initial dye concentration from 6.25 to 100 mg L⁻¹ generates an increase of the adsorption capacity from 8 to 90 mg g⁻¹ and a dye removal efficiency decrease from 60 to about 45 %.

The influence of ionic strength on adsorption process

Increasing the solution ionic strength generates a decrease of the adsorption capacity, illustrated in Fig. 8, due to competition between methylene blue cations and sodium ions to occupy the available adsorption sites on the surface of the adsorbent.^{32,33} The unfavourable effect of ionic strength on methylene blue adsorption process was also mentioned in other studies. Thus, for *A. platensis* biomass,²⁸ lotus leaves³² and phoenix tree leaves³³ adsorbents an increase in ionic strength from 0 to 0.2 mol L⁻¹ leads to an adsorption capacity decrease of 72, 22 and 7 %, respectively.

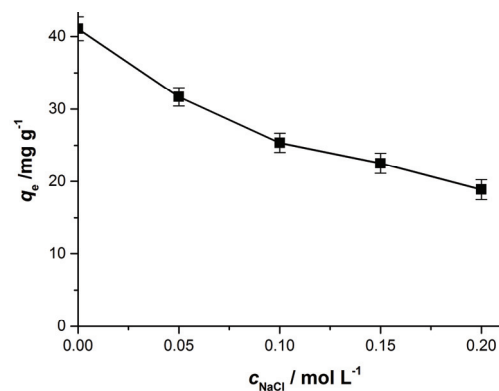


Fig. 8. Influence of ionic strength on adsorption capacity.

The influence of temperature on adsorption process

According to Fig. 9 the adsorption capacity decreases with increasing the temperature indicating that the process is exothermic in nature. The binding forces between the adsorbent surface and the adsorbate molecules become weaker with increasing temperature.^{34,35} Similar observations have been reported by others previous articles. When *Salix babylonica* leaves,⁷ *Haloxylon recurvum* plant stems²⁹ and Natural Muscovite Clay³⁴ were used as adsorbent materials to remove methylene blue from aqueous solutions, a negative effect of temperature rise on the adsorption capacity was observed.

Equilibrium isotherms

In order to study the interactions between the dye molecules and the adsorbent surface three isotherms were tested: Langmuir, Freundlich and Temkin.

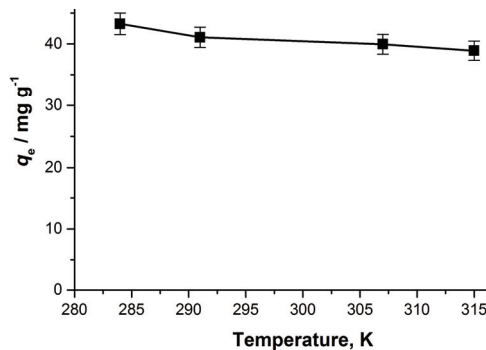


Fig. 9. Influence of temperature on adsorption capacity.

Fig. 10 shows the plots of the tested adsorption isotherms (non-linear forms). The values of adsorption isotherms constants and also, of the corresponding error functions (R^2 , SSE, χ^2 , ARE) are summarized in Table II.

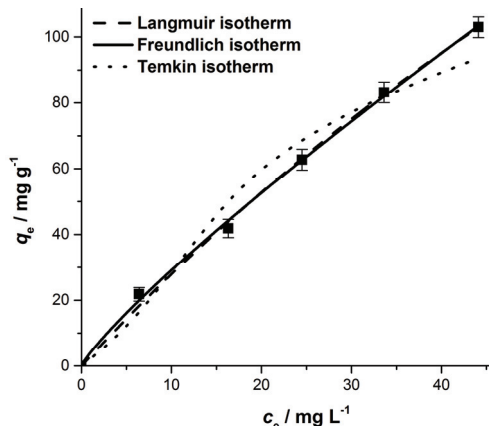


Fig. 10. The tested adsorption isotherms (non-linear forms) for the methylene blue adsorption.

Both the Langmuir isotherm and the Freundlich isotherm characterize very well the adsorption process (Fig. 10). Considering the higher value for determination coefficient (R^2) and the lower values of SSE, χ^2 and ARE it can be concluded that Freundlich isotherm best describes the process. The obtained results agree with those mentioned by other researchers in methylene blue adsorption studies, this isotherm characterizing the dye retention processes on adsorbent materials obtained from *Elaeis guineensis* leaves,⁴ *Haloxylon recurvum* stems²⁹ and *Euchema Spinosum* alga.³⁰

Table III shows a comparison between the maximum adsorption capacities values for methylene blue adsorption using similar low-cost adsorbents.

Adsorption kinetics

The kinetics of the methylene blue adsorption process on the studied adsorbent was investigated by means of kinetic models (non-linear forms): pseudo-

-first order, pseudo-second order and Elovich. The plots of these kinetic models and the value of their specific constants are illustrated in Fig. 11 and Table IV, respectively. The values of the coefficients of determination (R^2) for all models are above 0.96, the highest recorded value was for the pseudo-second order model while the lowest value corresponds to the Elovich model. The calculated values of the error functions (χ^2 , SSE and ARE) are the lowest for the pseudo-second order model.

TABLE II. Adsorption isotherms models constants and the corresponding error functions

Isotherm model	Parameter	Value
Langmuir non-linear	$K_L / L \text{ mg}^{-1}$	0.006±0.001
	$q_{\max} / \text{mg g}^{-1}$	485.1±9.23
	R^2	0.9978
	χ^2	0.78
	SSE	17.37
	ARE / %	5.08
	$K_f / \text{mg g}^{-1}$	4.07±0.74
	$1/n$	0.85±0.07
	R^2	0.9985
	χ^2	0.32
Freundlich non-linear	SSE	10.90
	ARE / %	3.39
	$K_T / L \text{ mg}^{-1}$	0.220±0.043
	$B / \text{kJ g}^{-1}$	58.77±6.94
	R^2	0.9584
Temkin non-linear	χ^2	7.81
	SSE	307.29
	ARE / %	18.81

TABLE III. The maximum adsorption capacities (mg g⁻¹) for methylene blue on different low-cost adsorbents

Adsorbent	Value
<i>Citrullus colocynthis</i> seeds ⁶	18.8
<i>Phragmites australis</i> biomass ³¹	22.7
<i>Haloxylon recurvum</i> stems ²⁹	22.9
<i>Salix babylonica</i> leaves ⁷	60.9
<i>Daucus carota</i> leaves ³	66.5
Phoenix tree leaves ³³	80.9
<i>Elaeis guineensis</i> leaves ⁴	103.0
Dry bean pods husks ⁸	121.1
Fava bean peel ¹	140.0
lotus leaf ³²	221.7
Citrus limetta peel ¹⁰	227.3
<i>Arthrospira platensis</i> biomass ²⁸	312.5
Bathurst burr biomass (this study)	485.1
<i>Euchema Spinosum</i> algae ³⁰	833.3

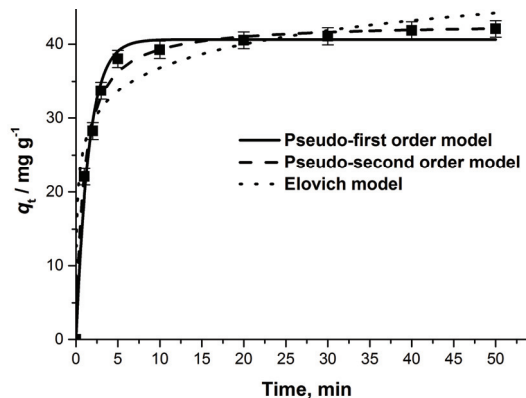


Fig. 11. The tested kinetic models (non-linear forms) for the methylene blue adsorption.

TABLE IV. Kinetic models constants and the corresponding error functions

Kinetic model	Parameter	Value
Pseudo-first order non-linear	k_1 / min^{-1}	0.648 ± 0.051
	$q_{e,\text{calc}} / \text{mg g}^{-1}$	40.63 ± 0.4
	R^2	0.9899
	χ^2	0.61
	SSE	16.37
	ARE / %	13.48
Pseudo-second order non-linear	k_2 / min^{-1}	0.025 ± 0.004
	$q_{e,\text{calc}} / \text{g mg}^{-1} \text{ min}^{-1}$	42.86 ± 0.38
	R^2	0.9962
	χ^2	0.17
	SSE	5.84
	ARE / %	11.59
Elovich non-linear	$a / \text{g mg}^{-1}$	0.218 ± 0.048
	$b / \text{mg g}^{-1} \text{ min}^{-1}$	1434 ± 124
	R^2	0.9635
	χ^2	1.95
	SSE	57.41
	ARE / %	15.84

These results indicate that the adsorption process is best described by this kinetic model. The conclusion is also supported by the calculated value of equilibrium adsorption capacity 42.86 mg g^{-1} which is very close to experimental value 42.05 mg g^{-1} . The pseudo-second order kinetic model also characterized other similar methylene blue adsorption processes on other adsorbents based on *Salix babylonica* leaves,⁷ corn cobs,⁹ *Euchema Spinosum* macro-alga,³⁰ *Phragmites australis* biomass³¹ and lotus leaves.³²

Thermodynamic parameters

The thermodynamic parameters of dye adsorption process, calculated bases on experimental results obtained at 284, 291, 307 and 315 K, are presented in

Table V. The negative values of standard Gibbs energy change (ΔG^0) and standard enthalpy change (ΔH^0) indicate a spontaneous, favourable and exothermic process. The positive value of standard entropy change (ΔS^0) shows an increase randomness at solid–liquid interface. The value of ΔG^0 is in the range –20 to 0 kJ mol^{–1} and the ΔH^0 value is lower than 40 kJ mol^{–1}, therefore the main mechanism involved in absorption is physisorption.^{7,29,31,34,35}

TABLE V. Thermodynamic parameters for the methylene blue adsorption onto bathurst burr powder

$\Delta G^0 / \text{kJ mol}^{-1}$				$\Delta H^0 / \text{kJ mol}^{-1}$	$\Delta S^0 / \text{J mol}^{-1} \text{K}^{-1}$
284 K	291 K	307 K	315 K		
–19.04	–19.18	–19.78	–19.91	–1.26	3.60

Optimization adsorption parameters by Taguchi method

The L27 orthogonal array and the obtained results after each run, for dye removal efficiency and the *S/N* ratios, are summarized in Table VI. The order of the controllable factors' significance (Table VII) was established using the rank of *S/N* ratio and delta values (difference between the highest and lowest average response values for each factor).¹⁸

TABLE VI. Experimental layout of L27 orthogonal array

τ / min	Adsorbent dose, mg L ^{–1}	pH	Initial dye concentration, mg L ^{–1}	Ionic strength mol L ^{–1}	T / K	Removal efficiency, %	S/N
1	0.5	2	50	0.0	284	18.73	25.45
1	0.5	2	50	0.1	291	10.97	20.80
1	0.5	2	50	0.2	315	7.74	17.78
1	1.5	6	250	0.1	284	40.27	32.09
1	1.5	6	250	0.2	291	23.59	27.45
1	1.5	6	250	0.0	315	16.64	24.42
1	3.0	10	150	0.2	284	44.93	33.05
1	3.0	10	150	0.0	291	26.32	28.40
1	3.0	10	150	0.1	315	18.57	25.37
10	0.5	10	250	0.2	284	27.61	28.82
10	0.5	10	250	0.0	291	19.52	25.81
10	0.5	10	250	0.1	315	40.25	32.09
10	1.5	2	150	0.0	284	56.74	35.07
10	1.5	2	150	0.1	291	40.12	32.06
10	1.5	2	150	0.2	315	82.71	38.35
10	3.0	6	50	0.1	284	42.06	32.47
10	3.0	6	50	0.2	291	29.74	29.46
10	3.0	6	50	0.0	315	61.31	35.75
30	0.5	6	150	0.1	284	23.53	27.43
30	0.5	6	150	0.2	291	48.60	33.73
30	0.5	6	150	0.0	315	28.42	29.07
30	1.5	10	50	0.2	284	30.66	29.73

TABLE VI. Continued

τ / min	Adsorbent dose, mg L ⁻¹	pH	Initial dye concentration, mg L ⁻¹	Ionic strength mol L ⁻¹	T / K	Removal efficiency, %	S/N
30	1.5	10	50	0.0	291	63.32	36.03
30	1.5	10	50	0.1	315	37.02	31.37
30	3.0	2	250	0.0	284	42.43	32.55
30	3.0	2	250	0.1	291	87.64	38.85
30	3.0	2	250	0.2	315	51.25	34.19

TABLE VII. Response table for signal-to-noise ratios

Level	Time	Adsorbent dose	pH	Initial dye concentration	Ionic strength	Temperature
1	26.78	28.76	26.10	30.57	33.94	30.74
2	31.85	30.70	32.21	30.21	29.74	30.29
3	32.24	31.40	32.55	30.08	27.18	29.83
Delta	5.46	2.63	6.46	0.49	6.75	0.92
Rank	3	4	2	6	1	5

The factor having the highest influence on the adsorption process was the ionic strength while the factor with the least influence was initial dye concentration. Correlating the data from Table I and Table VI, the optimum adsorption conditions were: time 30 min, adsorbent dose 3 mg L⁻¹, pH 10, initial dye concentration 50 mg L⁻¹, no ions and temperature 284 K.

CONCLUSION

Powdered material obtained from bathurst burr biomass is an efficient low-cost and easily available adsorbent for methylene blue removal from aqueous solutions. The adsorption is influenced by contact time, adsorbent dose, pH, initial dye concentration, ionic strength and temperature and is best described by Freundlich isotherm and pseudo-second order kinetic model. The process is spontaneous, favourable and exothermic and the main mechanism involved is physisorption. The ionic strength is the factor with the highest influence on the process and initial dye concentration least influences the adsorption.

ИЗВОД

ПРАШКАСТИ АДСОРБЕНТ ДОБИЈЕН ИЗ БИОМАСЕ *Xanthium spinosum* ЗА УКЛАЊАЊЕ МЕТИЛЕНСКОГ ПЛАВОГ ИЗ ВОДЕНИХ РАСТВОРА

GIANNIN MOSOARCA¹, COSMIN VANCEA¹, SIMONA POPA¹, MARIA ELENA RADULESCU-GRAD²
и SORINA BORAN¹

¹Politehnica University Timisoara, Faculty of Industrial Chemistry and Environmental Engineering, Bd. V. Parvan, No. 6, 300223, Timisoara, Romania и ²"Coriolan Dragulescu" Institute of Chemistry, Romanian Academy, Mihai Viteazu Bd. No. 24, 300223 Timisoara, Romania

Адсорбент у праху добијен из *Xanthium spinosum* биомасе је испитиван за уклањање метиленског плавог из водених растворова. SEM и FTIR анализе су коришћене за карактеризацију адсорбента пре и након адсорпције. Испитан је утицај времена контакта, дозе

адсорбента, pH, почетне концентрације боје, јонске јачине и температуре на процес адсорпције. Кинетичка, равнотежна и термодинамичка испитивања су вршена ради анализа процеса адсорпције. Тагучи метод је коришћен да би се одредили најбољи услови за адсорпцију боје. Процес је спонтан, фаворизован, егзотерман, описује га Фројндлихова изотерма и кинетички модел псеудо-другог реда. Тагучи метод указује да је јонска јачина фактор који има највећи утицај на процес адсорпције.

(Примљено 16. марта, ревидирано 30. априла, прихваћено 4. маја 2022)

REFERENCES

1. O. S. Bayomie, H. Kandeel, T. Shoeib, H. Yang, N. Youssef, M. M. H. El-Sayed, *Sci. Rep.* **10** (2020) 7824 (<https://doi.org/10.1038/s41598-020-64727-5>)
2. N. Choudhary, V. K. Yadav, K. K. Yadav, A. I. Almohana, S. F. Almojil, G. Gnanamoorthy, D. H. Kim, S. Islam, P. Kumar, B. H. Jeon, *Water* **13** (2021) 3206 (<https://doi.org/10.3390/w13223206>)
3. A. K. Kushwaha, N. Gupta, M. C. Chattopadhyaya, *J. Saudi. Chem. Soc.* **18** (2014) 200 (<https://doi.org/10.1016/j.jscs.2011.06.011>)
4. H. D. Setiabudi, R. Jusoh, S. F. R. M. Suhaimi, S. F. Masrur, *J. Taiwan Inst. Chem. Eng.* **63** (2016) 363 (<https://doi.org/10.1016/j.jtice.2016.03.035>)
5. K. Sharma, S. Sharma, V. Sharma, P. K. Mishra, A. Ekielski, V. Sharma, V. Kumar, *Nanomaterials* **11** (2021) 1403 (<https://doi.org/10.3390/nano11061403>)
6. W. M. Alghamdi, I. El Mannoubi, *Processes* **9** (2021) 1279 (<https://doi.org/10.3390/pr9081279>)
7. A. Khodabandehloo, A. Rahbar-Kelishami, H. Shayesteh, *J. Mol. Liq.* **244** (2017) 540 (<https://doi.org/10.1016/j.molliq.2017.08.108>)
8. G. Mosoarca, S. Popa, C. Vancea, S. Boran, *Materials* **14** (2021) 5673 (<https://doi.org/10.3390/ma14195673>)
9. P. M. K. Reddy, P. Verma, C. Subrahmanyam, *J. Taiwan Inst. Chem. Eng.* **58** (2016) 500 (<https://doi.org/10.1016/j.jtice.2015.07.006>)
10. S. Shakoor, A. J. Nasar, *Taiwan. Inst. Chem. Eng.* **66** (2016) 154 (<https://doi.org/10.1016/j.jtice.2016.06.009>)
11. L. R. G. Holm, D. L. Plucknett, J. V. Pancho, J. P. Herberger, *The world's worst weeds. Distribution and biology*, University Press of Hawaii, Honolulu, HI, 1977 (ISBN 0824802950)
12. G. Raman, K. T. Park, J. H. Kim, S. J. Park, *BMC Genomics* **21** (2020) 855 (<https://doi.org/10.1186/s12864-020-07219-0>)
13. G. Mosoarca, C. Vancea, S. Popa, S. Boran, *Materials* **14** (2021) 5861 (<https://doi.org/10.3390/ma14195861>)
14. G. L. Dotto, N. P. G. Salau, J. S. Piccin, T. R. S. Cadaval, L. A. A. de Pinto, in *Adsorption Processes for Water Treatment and Purification*, A. Bonilla-Petriciolet, D. Mendoza-Castillo, H. Reynel-Ávila, Eds., Springer, Cham, 2017, p. 53 (https://doi.org/10.1007/978-3-319-58136-1_3)
15. V. M. Esquerdo, T. M. Quintana, G. L. Dotto, L. A. A. Pinto, *Reac. Kinet. Mech. Cat.* **116** (2015) 105 (<http://doi.org/10.1007/s11144-015-0893-5>)
16. M. S. Netto, J. Georgin, D. S. P. Franco, E. S. Mallmann, E. L. Foletto, M. Godinho, D. Pinto, G. L. Dotto, *Environ. Sci. Pollut. Res.* **29** (2022) 3672 (<https://doi.org.libproxy.viko.lt/10.1007/s11356-021-15366-4>)

17. J. S. Piccin, T. R. S. Cadaval, L. A. A. de Pinto, G. L. Dotto, in *Adsorption Processes for Water Treatment and Purification*, A. Bonilla-Petriciolet, D. Mendoza-Castillo, H. Reynel-Ávila, Eds., Springer, Cham, 2017, p. 19 (https://doi.org/10.1007/978-3-319-58136-1_2)
18. J. A. Fernandez-Lopez, J. M. Angosto, M. J. Roca, M. Doval Minarro, *Sci. Total Environ.* **653** (2019) 55 (<https://doi.org/10.1016/j.scitotenv.2018.10.343>)
19. S. R. Korake, P. D. Jadhao, *Heliyon* **6** (2020) e05755 (<https://doi.org/10.1016/j.heliyon.2020.e05755>)
20. S. S. Madan, K. L. Wasewar, *J. Appl. Res. Technol.* **15** (2017) 332 (<https://doi.org/10.1016/j.jart.2017.02.007>)
21. P. Senthamaraiakannan, M. R. Sanjay, K. S. Bhat, N. H. Padmaraj, M. Jawaid, *J. Nat. Fibers* **16** (2019) 1124 (<http://doi.org/10.1080/15440478.2018.1453432>)
22. Tsuboi L. M. F. Pardo, A. G. Córdoba, J. E. L. Galán, *DYNA* **86** (2019) 98 (<http://doi.org/10.15446/dyna.v86n210.75757>)
23. S. Karimi, P. M. Tahir, A. Karimi, A. Dufresne, A. Abdulkhani, *Carbohydr. Polym.* **101** (2013) 878 (<http://doi.org/10.1016/j.carbpol.2013.09.106>)
24. R. Md Salim, J. Asik, M. S. Sarjadi, *Wood Sci. Technol.* **55** (2021) 295 (<https://doi.org/10.1007/s00226-020-01258-2>)
25. N. Labbe, T. G. Rials, S. S. Kelley, Z. M. Cheng, J. Y. Kim, Y. Li, *Wood Sci. Technol.* **39** (2005) 61 (<https://doi.org/10.1007/s00226-004-0274-0>)
26. I. Kubovský, D. Kačíková, F. Kačík, *Polymers* **12** (2020) 485 (<https://doi.org/10.3390/polym12020485>)
27. C. Y. Liang, R. H. Marchessault, *J. Polym. Sci.* **39** (1959) 269 (<http://doi.org/10.1002/pol.1959.1203913521>)
28. D. Mitrogiannis, G. Markou, A. Çelekli, H. J. Bozkurt, *Environ. Chem. Eng.* **3** (2015) 670 (<http://doi.org/10.1016/j.jece.2015.02.008>)
29. W. Hassan, U. Farooq, M. Ahmad, M. Athar, M. A. Khan, *Arab. J. Chem.* **10** (2017) S1512 (<https://doi.org/10.1016/j.arabjc.2013.05.002>)
30. N. Mokhtar, E. A. Aziz, A. Aris, W. F. W. Ishak, N. S. M. Ali, *J. Environ. Chem. Eng.* **5** (2017) 5721–5731 (<https://doi.org/10.1016/j.jece.2017.10.043>)
31. G. B. Kankılıç, A. U. Metin, I. Tüzün, *Ecol. Eng.* **86** (2016) 85 (<https://doi.org/10.1016/j.ecoleng.2015.10.024>)
32. X. Han, W. Wang, X. Ma, *Chem. Eng. J.* **171** (2011) 1 (<http://doi.org/10.1016/j.cej.2011.02.067>)
33. R. Han, W. Zou, W. Yu, S. Cheng, Y. Wang, J. Shi, *J. Hazard. Mater.* **141** (2007) 156 (<https://doi.org/10.1016/j.jhazmat.2006.06.107>)
34. O. Amrhar, A. Berisha, L. El Gana, H. Nassali, M. S. Elyoubi, *Int. J. Environ. Anal. Chem.* (2021) (<https://doi.org/10.1080/03067319.2021.1897119>)
35. C. Saucier, M. A. Adebayo, E. C. Lima, L. D. T. Prola, P. S. Thue, C. S. Umpierres, M. J. Puchana-Rosero, F. M. Machado, *Clean (Weinh)* **43** (2015) 1389 (<https://doi.org/10.1002/clen.201400669>).



Do Serbian high school students possess knowledge of basic chemical facts related to real life as a prerequisite for chemical literacy?

FILIP STAŠEVIĆ¹, NASTA MILETIĆ², JELENA ĐURĐEVIĆ NIKOLIĆ^{1*}#
and IVAN GUTMAN^{1#}

¹University of Kragujevac, Faculty of Science, Radoja Domanovića 12, 34000 Kragujevac,
Serbia and ²Gymnasium Kosovska Mitrovica, Lole Ribara 29, 38220
Kosovska Mitrovica, Serbia

(Received 26 November 2021, revised 21 November, accepted 22 November 2022)

Abstract: For a long time, literacy has had a deeper meaning than just the ability of reading and writing. Chemical literacy, as a part of science literacy, represents the use of chemical knowledge and skills in solving real life problems. With the increasing influence that chemistry has on society, chemical literacy becomes one of the main goals of science education. In order to examine the knowledge of chemical facts related to real life (as a prerequisite for chemical literacy) of high school students ($N = 379$), we designed a knowledge test and constructed a scoring scale for evaluating achievements. The obtained results are contrary to expectations, *i.e.*, a large number of students did not achieve a satisfactory level of knowing selected chemical facts chosen by the authors. The small number of correct answers per question indicates that the examined sample of students does not show a desirable level of chemical knowledge, implying that there is a need for new, improved strategies in chemistry teaching.

Keywords: chemistry teaching; students' achievements; basic chemical knowledge.

INTRODUCTION

Literacy, in its most common usage, is defined as the ability to read and write.¹ In the 21st century, we can say that this definition is not appropriate and that the concept of literacy is much broader. Literacy is a characteristic needed not just for highly educated people, but due to a different organization of society, it is everyone's necessity.² Contemporary time shapes literacy and determines

* Corresponding author. E-mail: jelena.djurdjevic@pmf.kg.ac.rs

Serbian Chemical Society member.

<https://doi.org/10.2298/JSC211126083S>

required abilities and skills. The digital age, the accelerated flow of information that quickly becomes outdated, the development of civilisation and technology demands constant learning. Therefore, the definition of literacy is complex and dynamic. There are several forms of literacy: nominal, functional, conceptual, scientific, media, digital, political.^{3–7} Many authors worldwide maintain that scientific literacy should be one of the main goals of science education. The reason for this is the increasing impact of science and technology on everyday life and social, political, educational, technological, and economic advancement.^{8–10}

Chemical literacy, as a part of scientific literacy, should be available to the broader public, not just to chemists, which would imply the use of chemistry knowledge and skills in various situations.¹¹ Individuals who are chemical literate are:

1. able to apply knowledge and skills from the chemistry domain in daily life;
2. aware of the significance of chemistry;
3. understand the relationship between chemistry, technology and society.^{12–16}

As one of the scientific disciplines, chemistry has an important role to help students to understand and use basic chemical facts and concepts which is one of the prerequisites for chemical literacy. Chemical literacy is needed to understand many processes and science-related issues that occur in everyday life.^{17,18} Chemistry topics involve studying matter and properties of matter that are important in many disciplines such as health sciences, geography, physics, environmental science.^{19,20} It is well known that chemicals can play a vital role in our daily lives. Therefore, it is necessary to enhance human conscience about chemistry, prepare the population for the proper use of chemistry knowledge and provide them with the ability for long-life learning. Also, learning chemistry should not just lean on learning the content available in textbooks. Learning must be effective, by making links between chemical knowledge and real life, involving activities based on solving life problems related to chemical issues. Accordingly, the published standards and benchmarks regarding content enable achieving the main goal of chemistry education, and that is chemistry literacy for all students.^{21,22} The role of the teacher is to adapt the given curriculum, keeping in mind the type of class composition and student characteristics, also considering textbooks and other teaching materials, as well as the technical conditions, teaching tools and media available to the school. The chemistry curriculum in high school education describes the teaching process, goals, outcomes, contents, and educational activities. Standards of achievements define the result of that process, namely, required knowledge, skills and attitudes for solving different societal challenges. These standards specify the results expected from all students (basic level), the results that are the basis for continuing education at the university level in areas not

directly related to chemistry (intermediate level), and the results in chemistry required for further education in chemistry area (advanced level). Hence, there are three levels of standards of achievement, which are cumulative, built into each other, so that students at the advanced level satisfy the requirements from all three levels. The standards of achievements describe the qualitative and quantitative results of the teaching process and thus give the description of what students know and can do based on their overall general education in chemistry. As one of the goals of chemistry education is the functionality and applicability of knowledge, achieving a certain level of standards of achievement means accomplishing a certain level of functional chemical knowledge.

The program for International Student Assessment (PISA) and Trends in Mathematics and Science Studies (TIMSS) are two programs used for monitoring the progress of the skills that are essential for every child to progress through school and life. TIMSS assessments provide an insight into students' achievement in mathematics and science, using the scale that measures the students' knowledge, knowledge application and reasoning ability.^{23–25} According to testing under the TIMSS and obtained results (2011, 2015 and 2019), the average accomplishment of the Serbian students (>500) was statistically higher than the previously determined average value, which placed them at 25th (2011) 24th (2015) and 21st (2019) position on the list.^{26–29} It should be noted that in these studies, participants were fourth-grade students from elementary school. PISA tends to focus on practical knowledge in action, namely recognizing questions as scientific, identifying relevant evidence, critically evaluating conclusions, and communicating scientific ideas.^{30–33} The last results of scientific literacy for 15-years-old students assessed evaluated by PISA 2018 showed that a mean score (440) of students from Serbia in scientific literacy was statistically significantly below the Organization for Economic Cooperation and Development (OECD) average (489), so that the students from Serbia ranked 45th from 79 countries.³⁴

Although the TIMSS results show solid achievements of younger primary school students, PISA assessment results are warning signs that we should be concerned about the scientific literacy of the country's population. Therefore, the present researchers were aimed at examining the level of basic chemical knowledge of the high school students from different school profiles using the test based on knowing different chemical terms and facts related to daily life.

EXPERIMENTAL

Research aims and research questions

The purpose of the present study was to provide an insight into the manifestation of various aspects of chemical literacy, such as knowing basic chemical facts related to everyday life, among high school students, without any hidden intentions, as discrediting students, and teachers. Since chemistry knowledge is important for society, research questions that guide researchers were:

1. What is the situation in high schools with students' knowledge of basic chemical facts and terms related to real life?
2. Which level of chemical knowledge possess students based on the researchers' scoring scale and the standards of achievements?
3. Is there a difference in the knowledge between Gymnasium students and Vocational school students?

Sample/participants

Simple random sampling was used to select the participants for testing. A heterogeneous sample ($N = 379$) included the high school students from two different types of schools in Serbia, gymnasium ($N = 270$) and vocational school ($N = 109$). The participants from gymnasium were all 4th grade high school students with an orientation to natural sciences and mathematics, whereas participants from three vocational schools were 1st grade (economic school, $N = 28$) 2nd grade (medical school, $N = 52$) and 4th grade (technical school, $N = 29$) high school students. Chemistry course as a general-educational subject lasts a different number of years depending on a vocational school. The medical school has chemistry for two years (pharmacy technician), the economic school has chemistry one year (economic technician) and the technical school (industrial-pharmaceutical technician) has chemistry for four years. The curriculum for all schools emphasizes knowing basic chemical concepts and facts regardless of the different duration of the chemistry education, the number of different chemistry courses, and the different number of classes per year. Looking into the curriculum of these different school profiles reveals the same main topics that provide students the required knowledge. The number of classes for the entire chemistry education determined by the curriculum for each school and profile is provided in Table I.

TABLE I. Number of the chemistry classes per school

Type of school and selected profile	Number of the theoretical classes	Number of the practical classes
Gymnasium	288	74
Technical school	484	516
Medical school	134	0
Economic school	74	0

The total number of classes (theoretical and practical) determined by the curriculum for selected modules are 362 (Gymnasium), 1000 (Technical school), 134 (Medical school) and 74 (Economic school). A large number of the classes in Technical school is due to the fact that students in this school gain chemistry knowledge throughout several separate courses (General and Inorganic Chemistry, Organic Chemistry, Analytical Chemistry, Physical Chemistry and Biochemistry). Other selected schools have one course through the years that covers all chemistry disciplines listed above.

Instrument/design

The data were collected with the knowledge test administered to students in a paper form. The knowledge test contained 8 open-ended questions with a short answer. All the questions were based on the corresponding standards of achievements. The committee of experts (high school chemistry teachers and university chemistry teachers) who were not involved in its design confirmed the instrument's validity. Based on the evaluations, the revised items

were held in the instrument. Questions from the knowledge test defined with the corresponding standards of achievements are given in Table II.²²

TABLE II. Questions from the test with the respective standards of achievements

Question No.	Question	Standard of achievement
1.	In which human organ is the lowest pH value?	2.HE.1.1.5.
2.	At what temperature, ice melts, and inversely, water freezes to ice?	2.HE.1.1.2; 2.HE.1.2.3.
3.	Why is not good to squeeze the lemon into hot tea?	2.HE.1.3.2; 2.HE.1.4.1. 2.HE.1.4.2.
4.	Do sugar, milk, fruits, vegetables, bread contain the same carbohydrate?	2.HE.1.4.1; 2.HE.1.4.2.
5.	The test for drivers that measures the level of alcohol in the blood is based on which chemical reaction?	2.HE.1.3.3; 2.HE.1.3.4.
6.	Which compound provokes tingling after an ant's sting?	2.HE.1.3.1; 2.HE.1.3.4.
7.	Which gas is more commonly known as laughing gas?	2.HE.1.2.3.
8.	We often hear that limescale does damage to various household appliances and that it comes from hard water. Which salts contribute most to water hardness?	2.HE.1.2.3.

A set of questions covered by the instrument was chosen randomly from the curriculum with the intention to examine whether students know basic chemical concepts related with real life after they accomplish general chemistry education. The instrument was designed as a pilot version for providing the insight into the current situation with students' chemical knowledge. The obtained results could serve as a motive for more extensive research.

The instrument covered almost all the chemistry disciplines: general chemistry (first two questions), inorganic chemistry (second and last two questions), organic chemistry (fifth, sixth and third questions) and biochemistry (fourth and third questions). Students should get the necessary knowledge and competencies to solve the test throughout their chemistry education at primary and secondary school. It is worth mentioning, that all high school students included in this research were in the final year of their chemistry education. All participants went through all the topics set in the instrument during the chemistry courses through their schooling. It was expected, based on the standards of achievement, that the majority would access a basic level of chemical knowledge, *i.e.*, to recognize and connect chemical facts with daily life. Since chemical literacy is a multi-dimensional and complex term, it is difficult to assess all its aspects and components. The instrument was designed to measure acquired chemical knowledge for the end of general secondary chemical education, as well as knowing terms and facts from the chemistry domain, related to daily life. Without knowing basic chemical facts there is no functional chemical knowledge, as knowledge of these facts is a prerequisite for the existence of chemical literacy. The collected data were analysed both quantitatively and qualitatively with an emphasis on quantitative analysis, whereas the data analysis was carried out with several statistical tests (mean, standard deviation, Mann–Whitney test also called U-test).^{35,36} Answers were summed up and scored as correct, wrong and no answer. Descriptive statistics were reported in the percentages and the mean and standard deviation for the percentages were also given. The scoring scale, used to evaluate the level of students' chemical

knowledge, was constructed by the researchers and the responses to each question from the knowledge test were transcribed and scored. The scale was constructed and used to score and evaluate the students' chemical knowledge based on general standards of achievements for the end of secondary education.²² Values of correct answers on the questions were scored from low (1), moderate (2) to high level (3) of chemical knowledge as indicated in Table III. The new scoring scale is designed for better insight into the students' accomplishment of achievements on the knowledge test and better interpretation of the results. For primary school, it is specified that 80 % of students should achieve chemical knowledge at the basic level of standards of achievements.³⁷ As the standards of achievement for secondary school represent expanded knowledge, skills, and attitudes relative to those which are determined for primary school, it is expected that all high school students should achieve a basic level of standards of achievement.³⁸ All questions from the knowledge test were designed to be at a basic level by standards of achievements. The scale is determined by the number of correct answers, low level is less than 50 % correct answers, the moderate level implied 50–80 % of correct responses, whereas the high level is achieved with over 80 % of correct answers per question. Reaching a high level on the scale can be interpreted as satisfactory chemical knowledge on the basic level. The moderate level can be explicated as worrying, while the low level represents an alarming situation related to chemical knowledge. Expectations were that more than 80 % of students would reach a high level on the scoring scale.

TABLE III. Scoring scale for categorizing responses to questions

Level	Description of each category in interpretation responses
Low (1)	Students' chemical knowledge is low. Less than 50 % of correct answers per question. The situation is alarmingly worrying.
Moderate (2)	Students' chemical knowledge is moderate. Students' correct answers are between 50–80 % per question. The situation is worrying.
High (3)	Students' chemical knowledge is high. More than 80 % of correct answers per question. The situation is satisfactory.

RESULTS AND DISCUSSION

The data collected with the knowledge test are presented in the Table IV. Results (number of wrong, correct and no answers) are given in percentages and the number of respondents is given in parentheses.

TABLE IV. Distribution of answers (%) on the knowledge test; number of respondents are given in the parentheses

Question No. (Table II)	Answer		
	Correct	Wrong	Without answer
1	70.71 (268)	15.83 (60)	13.46 (51)
2	31.66 (120)	62.80 (238)	5.54 (21)
3	65.70 (249)	15.30 (58)	19.00 (72)
4	78.90 (299)	14.51 (55)	6.60 (25)
5	27.70 (105)	16.62 (63)	55.67 (211)
6	58.05 (220)	11.61 (44)	30.34 (115)
7	46.96 (178)	40.37 (153)	12.66 (48)
8	46.17 (175)	19.26 (73)	34.56 (131)

Transcribed to a researchers' scale, the respondents are on the transition of two levels, low and moderate. Students showed a moderate level of chemical knowledge (50–80 % correct answers) on four questions (Question No. 1, 3, 4 and 6) and low level (<50 % correct answers) on the same number of questions (Question No. 2, 5, 7 and 8) toward scale score, but no one achieved a high level of knowledge. Based on these results, the students do not reach the expected level of basic chemical knowledge and the situation in schools can be interpreted as not satisfactory.

The question with the most correct answers is the fourth question (78 %), while the question with the lowest number of correct answers is the fifth question (27.7 %). It is important to pay attention to a low level of chemical knowledge of the students related to the second question where the number of correct answers was only 31.66 %. Based on these results, the students did not achieve a sufficient level of basic chemical knowledge, as expected by standards of achievement.^{37,38}

According to the scoring scale and students' accomplishments on the individual questions (1, 3, 4 and 6), students know on a moderate level: acid–base properties of some body fluids and substances from real life (2.HE.1.1.5.); the role and presence of biologically important compounds as well as their physical properties and structure (2.HE.1.3.2.; 2.HE.1.4.1. and 2.HE.1.4.2.); structure, physical properties of carbohydrates (2.HE.1.4.1. and 2.HE.1.4.2.); trivial names of organic compounds and corresponding names according to IUPAC nomenclature (2.HE.1.3.1.), physical and chemical properties of organic compounds, and also their importance in everyday life (2.HE.1.3.4.). More precisely, students know on the moderate level which organ in the human organism is with the lowest pH value (stomach); the physical properties of vitamin C, *i.e.*, they know what happens with vitamin C at high temperatures (decomposition); formic acid provokes tingling after an ant's sting and that sugar, milk, fruits, vegetables, and bread do not contain the same carbohydrate.

Students' responses on the 2nd, 5th, 7th and 8th question disclose a low level of knowledge on the researchers' scale for the selected chemical facts: the physical and chemical properties of substances that they encounter in daily life (2.HE.1.1.2.; 2.HE.1.2.3.); chemical properties and some of the most significant reactions of organic compounds (2.HE.1.3.3. and 2.HE.1.3.4.) and the most important inorganic compounds as well their applicability (2.HE.1.2.3.). Students were expected to know at what temperature ice melts and water freezes; oxidation reaction of alcohol and reduction reaction of dichromate is that one on which is based test that measures the level of alcohol in the blood of drivers; nitrous oxide is laughing gas and that the salts of divalent metal cations contribute the most to the water hardness (Ca^{2+} ; Mg^{2+} , *etc.*).

The assessment of students' chemical knowledge revealed that only a small percentage of them know basic chemical facts related to real life. The problem may be that the newly acquired knowledge is not well assimilated, and thus, does not contribute to the students' ability to meaningfully comprehend the basic chemical concepts. The results also indicate many misinterpretations and misconceptions caused by mechanical learning. For example, helium was mentioned as the laughing gas instead of dinitrogen oxide or histamine, not formic acid, as a substance that causes tingling. Also, the frequent wrong answer was that ice melts at 4 °C and inversely, water becomes ice, probably because students know that this temperature is characteristic for water (on 4 °C water has maximum density).

Fig. 1 presents the students' correct answers to questions from the knowledge per school.

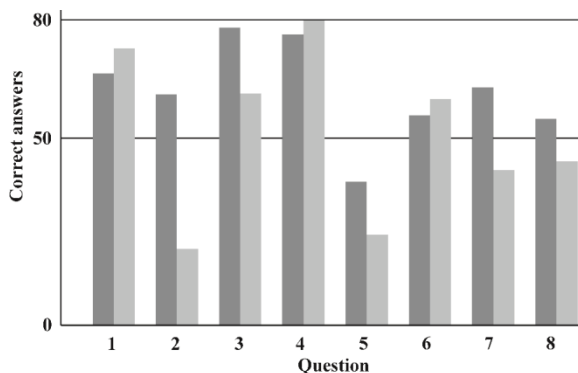


Fig. 1. Distribution of respondents' correct answers on questions per school; light grey – gymnasium, dark grey – vocational school.

The present researchers expected a non-significant difference in responses between students from two types of schools, firstly, because the questions were constructed on the basic level of chemical knowledge, and secondly, because the content and curriculum from both schools have the same goal, chemical literacy, and knowledge retention.

The mean value of the correct answers of gymnasium students is 50.00 with a standard deviation of 20.43, whereas this value for students from vocational school is 61.24 with a standard deviation of 12.12. Based on these values, it may be concluded that students from the vocational school give more correct answers per question with smaller deviation from the mean, and barely cross the moderate level of chemical knowledge towards researchers' scale score. On the other hand, students from gymnasium show oscillations in the number of correct answers per question, and do not cross the moderate level. U-test, that was carried out shows a significant difference with a p -value of 0.44 ($p > 0.05$; $z = \pm 0.77$). It cannot be known what happened in the individual classes through students' education, so,

the difference may be caused by the individual characteristics of both teachers and students and the quality of the teaching process.

The obtained results clearly show disagreement with the goals defined in curriculum which is based on applicable knowledge. A large number of wrong answers suggest that the learning process in Serbia's high schools is still grounded only on the reproduction of the content. Without the opportunity to understand and link content with real life, students will develop misinterpretations and misconceptions, so it can be expected that students would not be able to apply their knowledge.³⁹

Regarding this finding, developing new teaching forms could impact the functionality of students' knowledge, and it is also a call for chemistry teachers to provide an appropriate and conducive learning environment during the learning process. The context of chemistry in daily life situations should provide students the possibility to improve their literacy skills.^{40,41} The context-based learning with engaging all students during the learning process makes chemistry more relevant and relative to the students.⁴² Such approach leads students to relate real life to chemistry, with context that can be an environmental issue, an everyday life problem, or an industrial process.⁴³ Also, it is required to enhance the students' intrinsic motivation. Without this, students will continue to form knowledge with limited understanding based only on memorized facts.

CONCLUSION

For a long time, literacy does not mean just being able to read and write. No matter whether your work is connected directly or indirectly with chemistry, or you compete in a quiz, read some newspaper article, or buy a cosmetic product, you should have a basic level of chemical knowledge or, in other words, be chemically literate. Chemical literacy is a target in major reforms in science education today and it is conceptualized as a main goal. With that goal achieved, the school will provide people with sufficient and functional knowledge and the ability to solve real life problems.

The results obtained in this paper have highlighted that knowing basic chemical facts (as a prerequisite for chemistry literacy) among students remains low. It is worrying that the students do not know at what temperature ice melts, *i.e.*, water freezes to ice, and also, other similar chemical concepts tested with the instrument. The ignorance of the basic chemical concepts brought students to an unsatisfactory level of basic chemical knowledge. The achieved level of basic chemical knowledge is not sufficient to link the acquired knowledge to real life situations, and thus for the application of chemical concepts in daily life. Therefore, students mostly do not have the prerequisite for chemical literacy. Based on the standards of achievements, expectations were that more than 80 % of students would reach a high level on our scoring scale. The results reveal that the situation

about students' chemical knowledge is not satisfactory, none of the question reached a high level of the scoring scale. The authors had believed that there will be no significant difference in responses between students from different school profiles. Based on the results, students from the vocational school gave more correct answers per question than students from gymnasium. This result can trigger new research with an aim to confirm this difference and to analyse the reasons. The findings reflect that there still exists a need for developing learning activities throughout chemistry education in order to provide a chance for students to use their knowledge in real life situations.

Our results were collected before the SARS-CoV-2 pandemic, in 2018. The obtained results could serve as a motive for broader research on students' chemical literacy. A similar study is planned, after the pandemic is put under control, to examine the impact of simultaneously, non-simultaneously, and blended E-learning on students' knowledge required for reaching even a basic level of chemical literacy.

Acknowledgement. This work was supported by the Serbian Ministry of Education, Science and Technological Development (Agreement Nos. 451-03-68/2022-14/200122 and 451-03-01330/2020-14/2787).

ИЗВОД

ДА ЛИ УЧЕНИЦИ СРЕДЊИХ ШКОЛА У СРБИЈИ ИМАЈУ ФУНКЦИОНАЛНО ЗНАЊЕ ИЗ ХЕМИЈЕ?

ФИЛИП СТАШЕВИЋ¹, НАСТА МИЛЕТИЋ², ЈЕЛЕНА ЂУРЂЕВИЋ НИКОЛИЋ¹ и ИВАН ГУТМАН¹

¹Универзитет у Краљеву, Природно-математички факултет, Радоја Домановића 12, 34000 Краљевац и ²Гимназија Косовска Митровица, Лоле Рибара 29, 38220 Косовска Митровица

Већ дужи временски период бити писмен не подразумева само способност писања и читања. Хемијска писменост, као део научне писмености, представља употребу знања, вештина и ставова у решавању различитих друштвених изазова. Свест друштва о значају хемије, хемијску писменост уводи на листу главних циљева образовања и васпитања. Да би испитали ниво хемијског знања и ниво познавања основних хемијских чињеница, што је предуслов за хемијску писменост, средњошколаца ($N = 379$) осмишљен је упитник и скала за евалуацију постигнућа. Приказани резултати су у супротности очекивањима, тј. нису остварени захтеви дефинисани стандардима постигнућа на основном нивоу. Мали број тачних одговора указује да испитивани узорак ученика не поседује задовољавајући ниво знања из хемије, што наводи на потребу за развијањем нових, напреднијих метода у настави хемије.

(Примљено 26. новембра 2021, ревидирано 21 новембра, прихваћено 22. новембра 2022)

REFERENCES

1. B. V. Street, *Literacy in Theory and Practice*, Cambridge University Press, New York, 1984
2. P. Turiman, J. Omar, A. Mohd Daud, K. Osman, *Proc. Soc. Behav. Sci.* **59** (2012) 110
(<https://doi.org/10.1016/j.sbspro.2012.09.253>)

3. L. Verhoeven, in: *Encyclopedia of Language and Education. Encyclopedia of Language and Education Vol. 2*, V. Edwards, D. Corson, Eds., Springer, Dordrecht, 1997 (https://doi.org/10.1007/978-94-011-4540-4_14)
4. N. Feinstein, *Sci. Ed.* **95** (2011) 168 (<https://doi.org/10.1002/sce.20414>)
5. S. Livingstone, *Commun. Rev.* **7** (2010) 3 (<https://doi.org/10.1080/10714420490280152>)
6. D. Bawden, in: *Digital Literacies: Concepts, Policies and Practices*, C. Lankshear, M. Knobel, Eds., Peter Lang, New York, 2008 (ISBN: 1433101696)
7. C. A. Cassel, C. C. Lo, *Polit. Behav.* **19** (1997) 317 (<https://doi.org/10.1023/A:1024895721905>)
8. R. C. Laugksch, *Sci. Ed.* **84** (2000) 71 ([https://doi.org/10.1002/\(SICI\)1098-237X\(200001\)84:1<71::AID-SCE6>3.0.CO;2-C](https://doi.org/10.1002/(SICI)1098-237X(200001)84:1<71::AID-SCE6>3.0.CO;2-C))
9. W. Graber, P. Nentwig, H. Becker, E. Sumfleth, A. Pitton, K. Wollweber, D. Jorde, in: *Research in Science Education – Past, Present, and Future*, H. Behrendt, Ed., Springer, Dordrecht, 2001 (https://doi.org/10.1007/0-306-47639-8_6)
10. S. Avargil, O. Herscovitz, Y. J. Dori, *Think. Skills Creat.* **10** (2013) 189 (<https://doi.org/10.1016/j.tsc.2013.07.008>)
11. Y. Shwartz, R. Ben-Zvi, A. Hofstein, *J. Chem. Educ.* **83** (2006) 1557 (<https://doi.org/10.1021/ed083p1557>)
12. R. M. Hazen, J. S. Trefil, *J. Chem. Educ.* **68** (1991) 392 (<https://doi.org/10.1021/ed068p392>)
13. R. W. Missen, W. R. Smith, *J. Chem. Educ.* **66** (1989) 217 (<https://doi.org/10.1021/ed066p217>)
14. Y. Shwartz, R. Ben-Zvi, A. Hofstein, *Chem. Educ. Res. Pract.* **7** (2006) 203 (<https://doi.org/10.1039/B6RP90011A>)
15. M. K. Serry, C. McDonnell, *Chem. Educ. Res. Pract.* **14** (2013) 227 (<https://doi.org/10.1039/C3RP90006A>)
16. Z. Kohen, O. Herscovitz, Y. J. Dori, *Chem. Educ. Res. Pract.* **21** (2020) 250 (<https://doi.org/10.1039/c9rp00134d>)
17. P. E. Childs, S. M. Hayes, A. O'Dwyer, in: *Relevant Chemistry Education*, I. Eilks, A. Hofstein, Eds., SensePublishers, Rotterdam, 2015 (https://doi.org/10.1007/978-94-6300-175-5_3)
18. J. C. Besley, A. Dudo, M. Storksdieck, *J. Res. Sci. Teach.* **52** (2015) 199 (<https://doi.org/10.1002/tea.21186>)
19. T. Brown, H. E. LeMay, B. E. Bursten, *Chemistry the Central Science*, 8th ed., Prentice Hall, Hoboken, NJ, 2015 (ISBN: 0130103101)
20. P. Karvankova, D. Popjakova, *Int. J. Sci. Educ.* **40** (2018) 702 (<https://doi.org/10.1080/09500693.2018.1442598>)
21. *Curriculum for high schools, vocational schools and adult education*, Official Gazette, Belgrade, Serbia, <https://zuov.gov.rs/zakoni-i-pravilnici>, accessed 9.3.2022 (in Serbian)
22. *General standards of achievement for the end of general secondary education and upbringing and secondary vocational education and education in the field of general education subjects for the subject - Chemistry*, Institute for the Evaluation of the Quality of Education, Belgrade, 2013 (<https://ceo.edu.rs/стандарди-у-образовању>), (accessed 8.3.2022) (in Serbian)
23. D. Trivić, *Hemijski Pregled* **51** (2010) 148 (in Serbian)

24. K. Eriksson, O. Helenius, A. Ryve, *Instr. Sci.* **47** (2019) 1 (<https://doi.org/10.1007/s11251-018-9473-1>)
25. National Center for Education Statistics (NCES), *Trends in International Mathematics and Science Study* (TIMSS), <http://nces.ed.gov/TIMSS/> (accessed 13.9.2021)
26. M. O. Martin, I. V. S. Mullis, P. Foy, G. M. Stancu, *TIMSS 2011 International Results in Science*, TIMSS & PIRLS International Study Center, Boston College, Chestnut Hill, MA, 2012
27. M. O. Martin, I. V. S. Mullis, P. Foy, M. Hooper, *TIMSS 2015 International Results in Science*, TIMSS & PIRLS International Study Center, Boston College, Chestnut Hill, MA, 2016
28. I. Derić, N. Gutvajn, S. Jošić, N. Ševa, *National report TIMSS 2019 in Serbia*, Institute for pedagogical investigations, Belgrade, 2020 (ISBN 978-86-7447-153-1) (in Serbian)
29. V. F. Savec, B. Urankar, M. Aksela, I. Devetak, *J. Serb. Chem. Soc.* **82** (2017) 1193 (<https://doi.org/10.2298/JSC161221083S>)
30. P. J. Fensham, W. Harlen, *Int. J. Sci. Educ.* **21** (1999) 755 (<https://doi.org/10.1080/095006999290417>)
31. W. Harlen, *Stud. Sci. Educ.* **36** (2011) 79 (<https://doi.org/10.1080/03057260108560168>)
32. Organization for Economic Co-operation and Development (OECD-PISA), *Assessment of scientific literacy in the OECD / Pisa project*, <http://www.pisa.oecd.org/> (accessed 13.9.2021)
33. J. Korolija, S. Rajić, M. Tošić, Lj. Mandić, *J. Serb. Chem. Soc.* **80** (2015) 1567 (<https://doi.org/10.2298/JSC150522072K>)
34. M. Videnović, G. Čaprić, *PISA 2018 Report for the Republic Serbia*, Ministry of Education, Science and Technological Development of the Republic of Serbia, Belgrade, 2020 (in Serbian)
35. E. McCrum-Gardner, *Br. J. Oral Maxillofac. Surg.* **46** (2008) 38 (<https://doi.org/10.1016/j.bjoms.2007.09.002>)
36. H. W. Kruskal, A. W. Wallis, *J. Am. Stat. Assoc.* **47** (1952) 583 (<https://doi.org/10.2307/2280779>)
37. D. Trivić, R. Jankov, M. Randelović, V. Vukotić, M. Marković, R. Kovačević, M. Nikolić, *Educational standards for the end of compulsory education for the subject - chemistry*, Ministry of Education, Science and Technological Development of the Republic of Serbia, Belgrade, 2010 (ISBN 978-86-86715-22-7) (in Serbian)
38. *General standards of achievements for the end of general secondary and secondary vocational education and upbringing in the part of general education subjects for the subject – Chemistry, Handbook for teachers*, Institute for the Evaluation of the Quality of Education and Upbringing, Belgrade, 2015 (ISBN 978-86-86715-55-5) (in Serbian)
39. T. Hrin, D. Milenković, M. Segedinac, *Chem. Educ. Res. Pract.* **19** (2018) 305 (<https://doi.org/10.1039/c7rp00162b>)
40. J. Bennett, J. Holman, in *Chemical Education: Towards Research-based Practice. Science & Technology Education Library Vol. 17*, J. K. Gilbert, O. De Jong, R. Justi, D. F. Treagust, J. H. Van Driel, Eds., Springer, Dordrecht, 2002 (https://doi.org/10.1007/0-306-47977-X_8)
41. Y. J. Dori, S. Avargil, Z. Kohen, L. Saar, *Int. J. Sci. Educ.* **40** (2018) 1198 (<https://doi.org/10.1080/09500693.2018.1470351>)
42. J. K. Gilbert, *Int. J. Sci. Educ.* **28** (2006) 957 (<https://doi.org/10.1080/09500690600702470>)
43. J. P. Gutwill-Wise, *J. Chem. Educ.* **78** (2001) 684 (<https://doi.org/10.1021/ed078p684>).